International Journal of Physical Sciences

Academic Journals

ABOUT IJPS

The **International Journal of Physical Sciences (IJPS)** is published weekly (one volume per year) by Academic Journals.

International Journal of Physical Sciences (IJPS) is an open access journal that publishes high-quality solicited and unsolicited articles, in English, in all Physics and chemistry including artificial intelligence, neural processing, nuclear and particle physics, geophysics, physics in medicine and biology, plasma physics, semiconductor science and technology, wireless and optical communications, materials science, energy and fuels, environmental science and technology, combinatorial chemistry, natural products, molecular therapeutics, geochemistry, cement and concrete research, metallurgy, crystallography and computer-aided materials design. All articles published in IJPS are peer-reviewed.

Submission of Manuscript

Submit manuscripts as e-mail attachment to the Editorial Office at: ijps@academicjournals.org. A manuscript number will be mailed to the corresponding author shortly after submission.

For all other correspondence that cannot be sent by e-mail, please contact the editorial office (at ijps@academicjournals.org).

The International Journal of Physical Sciences will only accept manuscripts submitted as e-mail attachments.

Please read the **Instructions for Authors** before submitting your manuscript. The manuscript files should be given the last name of the first author.

Instructions for Author

Electronic submission of manuscripts is strongly encouraged, provided that the text, tables, and figures are included in a single Microsoft Word file (preferably in Arial font).

The **cover letter** should include the corresponding author's full address and telephone/fax numbers and should be in an e-mail message sent to the Editor, with the file, whose name should begin with the first author's surname, as an attachment.

Article Types
Three types of manuscripts may be submitted:

Regular articles: These should describe new and carefully confirmed findings, and experimental procedures should be given in sufficient detail for others to verify the work. The length of a full paper should be the minimum required to describe and interpret the work clearly.

Short Communications: A Short Communication is suitable for recording the results of complete small investigations or giving details of new models or hypotheses, innovative methods, techniques or apparatus. The style of main sections need not conform to that of full-length papers. Short communications are 2 to 4 printed pages (about 6 to 12 manuscript pages) in length.

Reviews: Submissions of reviews and perspectives covering topics of current interest are welcome and encouraged. Reviews should be concise and no longer than 4-6 printed pages (about 12 to 18 manuscript pages). Reviews are also peer-reviewed.

Review Process

All manuscripts are reviewed by an editor and members of the Editorial Board or qualified outside reviewers. Authors cannot nominate reviewers. Only reviewers randomly selected from our database with specialization in the subject area will be contacted to evaluate the manuscripts. The process will be blind review.
Decisions will be made as rapidly as possible, and the journal strives to return reviewers' comments to authors as fast as possible. The editorial board will re-review manuscripts that are accepted pending revision. It is the goal of the IJPS to publish manuscripts within weeks after submission.

Regular articles

All portions of the manuscript must be typed double-spaced and all pages numbered starting from the title page.

The Title should be a brief phrase describing the contents of the paper. The Title Page should include the authors' full names and affiliations, the name of the corresponding author along with phone, fax and E-mail information. Present addresses of authors should appear as a footnote.

The Abstract should be informative and completely self-explanatory, briefly present the topic, state the scope of the experiments, indicate significant data, and point out major findings and conclusions. The Abstract should be 100 to 200 words in length.. Complete sentences, active verbs, and the third person should be used, and the abstract should be written in the past tense. Standard nomenclature should be used and abbreviations should be avoided. No literature should be cited.
Following the abstract, about 3 to 10 key words that will provide indexing references should be listed.

A list of non-standard **Abbreviations** should be added. In general, non-standard abbreviations should be used only when the full term is very long and used often. Each abbreviation should be spelled out and introduced in parentheses the first time it is used in the text. Only recommended SI units should be used. Authors should use the solidus presentation (mg/ml). Standard abbreviations (such as ATP and DNA) need not be defined.

The Introduction should provide a clear statement of the problem, the relevant literature on the subject, and the proposed approach or solution. It should be understandable to colleagues from a broad range of scientific disciplines.

Materials and methods should be complete enough to allow experiments to be reproduced. However, only truly new procedures should be described in detail; previously published procedures should be cited, and important modifications of published procedures should be mentioned briefly. Capitalize trade names and include the manufacturer's name and address. Subheadings should be used. Methods in general use need not be described in detail.

Results should be presented with clarity and precision. The results should be written in the past tense when describing findings in the authors' experiments. Previously published findings should be written in the present tense. Results should be explained, but largely without referring to the literature. Discussion, speculation and detailed interpretation of data should not be included in the Results but should be put into the Discussion section.

The Discussion should interpret the findings in view of the results obtained in this and in past studies on this topic. State the conclusions in a few sentences at the end of the paper. The Results and Discussion sections can include subheadings, and when appropriate, both sections can be combined.

The Acknowledgments of people, grants, funds, etc should be brief.

Tables should be kept to a minimum and be designed to be as simple as possible. Tables are to be typed double-spaced throughout, including headings and footnotes. Each table should be on a separate page, numbered consecutively in Arabic numerals and supplied with a heading and a legend. Tables should be self-explanatory without reference to the text. The details of the methods used in the experiments should preferably be described in the legend instead of in the text. The same data should not be presented in both table and graph form or repeated in the text.

Figure legends should be typed in numerical order on a separate sheet. Graphics should be prepared using applications capable of generating high resolution GIF, TIFF, JPEG or Powerpoint before pasting in the Microsoft Word manuscript file. Tables should be prepared in Microsoft Word. Use Arabic numerals to designate figures and upper case letters for their parts (Figure 1). Begin each legend with a title and include sufficient description so that the figure is understandable without reading the text of the manuscript. Information given in legends should not be repeated in the text.

References: In the text, a reference identified by means of an author's name should be followed by the date of the reference in parentheses. When there are more than two authors, only the first author's name should be mentioned, followed by 'et al'. In the event that an author cited has had two or more works published during the same year, the reference, both in the text and in the reference list, should be identified by a lower case letter like 'a' and 'b' after the date to distinguish the works.

Examples:

Abayomi (2000), Agindotan et al. (2003), (Kelebeni, 1983), (Usman and Smith, 1992), (Chege, 1998;

1987a,b; Tijani, 1993,1995), (Kumasi et al., 2001)
References should be listed at the end of the paper in alphabetical order. Articles in preparation or articles submitted for publication, unpublished observations, personal communications, etc. should not be included in the reference list but should only be mentioned in the article text (e.g., A. Kingori, University of Nairobi, Kenya, personal communication). Journal names are abbreviated according to Chemical Abstracts. Authors are fully responsible for the accuracy of the references.

Examples:

Ogunseitan OA (1998). Protein method for investigating mercuric reductase gene expression in aquatic environments. Appl. Environ. Microbiol. 64:695-702.
Gueye M, Ndoye I, Dianda M, Danso SKA, Dreyfus B (1997). Active N2 fixation in several Faidherbia albida provenances. Ar. Soil Res. Rehabil. 11:63-70.

Charnley AK (1992). Mechanisms of fungal pathogenesis in insects with particular reference to locusts. In: Lomer CJ, Prior C (eds) Biological Controls of Locusts and Grasshoppers: Proceedings of an international workshop held at Cotonou, Benin. Oxford: CAB International, pp 181-190.

Mundree SG, Farrant JM (2000). Some physiological and molecular insights into the mechanisms of desiccation tolerance in the resurrection plant Xerophyta viscasa Baker. In Cherry et al. (eds) Plant tolerance to abiotic stresses in Agriculture: Role of Genetic Engineering, Kluwer Academic Publishers, Netherlands, pp 201-222.

Short Communications

Short Communications are limited to a maximum of two figures and one table. They should present a complete study that is more limited in scope than is found in full-length papers. The items of manuscript preparation listed above apply to Short Communications with the following differences: (1) Abstracts are limited to 100 words; (2) instead of a separate Materials and Methods section, experimental procedures may be incorporated into Figure Legends and Table footnotes; (3) Results and Discussion should be combined into a single section.
Proofs and Reprints: Electronic proofs will be sent (e-mail attachment) to the corresponding author as a PDF file. Page proofs are considered to be the final version of the manuscript. With the exception of typographical or minor clerical errors, no changes will be made in the manuscript at the proof stage.

ARTICLES

Full Length Research Paper

Synthesis and use of hydrotalcites as heat stabilisers in thermally processed powdered polyvinylchloride (PVC)

A. Bissessur[1]* and M. Naicker[2]

[1]School of Chemistry and Physics, University of KwaZulu-Natal, Private Bag X54001, Durban, 4000 South Africa.
[2]Department of Chemistry, University of South Africa, P. O. Box 392, Muckleneuk Ridge, City of Tshwane, 0003, South Africa.

Lead-based stabilisers, such as lead sulphate and lead stearate, currently used in the processing of polyvinylchloride (PVC) products are being substituted with more environmentally safe, economically viable and higher quality materials. This study aimed to use hydrotalcites (HTs), which are environmentally non-hazardous and simple to synthesise, to effectively quench the HCl gas evolved during the degradation of PVC. From the results obtained in this study, the effects of varying the metal ion ratios in Mg/Zn/Al-HTs showed many similarities with some variations. The synthesised Mg/Al-HTs, viz. $Mg_4Al_2(OH)_{12}CO_3.3H_2O$ and $Mg_6Al_2(OH)_{16}CO_3.4H_2O$, displayed the most superior stability properties, with the latter being the best PVC stabiliser, over the other HTs synthesised. The most important test conducted in this study, demonstrated the synthesised HTs ability to quench the HCl gas evolved as a result of dehydrochlorination, which occurs during the processing of PVC to useful polymeric products. Results from this study also confirmed that approximately 0.2 g of synthesised Mg/Al-HTs adsorbed 0.2 μmol of the HCl gas evolved, thus most effectively delayed the onset of degradation of powdered PVC (~10 g) than other HTs synthesised, including the non-stabilised PVC. It is thus evident that Mg/Al-HTs can function as effective heat stabilisers during the processing of PVC, with the potential of inhibiting the degradation of PVC, especially during the evolution of HCl gas.

Key words: Hydrotalcites, polyvinylchloride, thermal gravimetric analysis (TGA), dehydrochlorination, Brunauer–Emmett–Teller (BET) surface area, crystalline, amorphous.

INTRODUCTION

Lead compounds continue to assume an important role among stabilisers, especially in PVC derived products. Heat stabilisers are applied to polyvinylchloride (PVC) processing in order to prevent or minimise thermal instability, which is autocatalytic and leads to polymers adhering to the equipment (Gupta et al., 2008), discolouration, brittleness and insolubility. Common heat stabilisers used include metal salts, metal soaps and organometallic compounds. The toxicity and affinity for environmental pollution, renders these types of stabilisers harmful, therefore alternatives are required.

During the processing of PVC, stabilisers and additives are mixed and heated to form a solid, which can be subsequently moulded into a range of useful household and industrial products, examples: raincoats, toys, food packaging and conduits. When PVC is heated, chlorine and hydrogen atoms in the molecules are eliminated, and the release of HCl gas (dehydrochlorination) becomes apparent. This is an undesirable by-product that can negatively affect the properties and quality of the end products. Therefore it is vital that the evolution of hydrogen chloride be prevented, by using metal

*Corresponding author. E-mail: bissessura@ukzn.ac.za
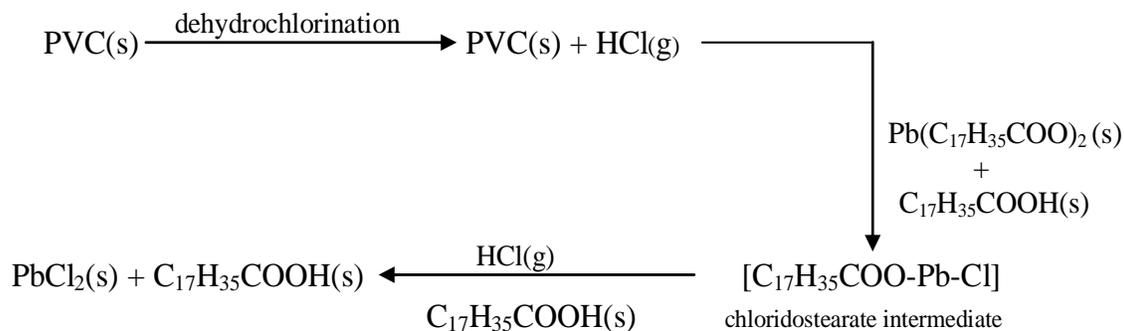
Scheme 1. Behaviour of lead stearate during the degradation of PVC.
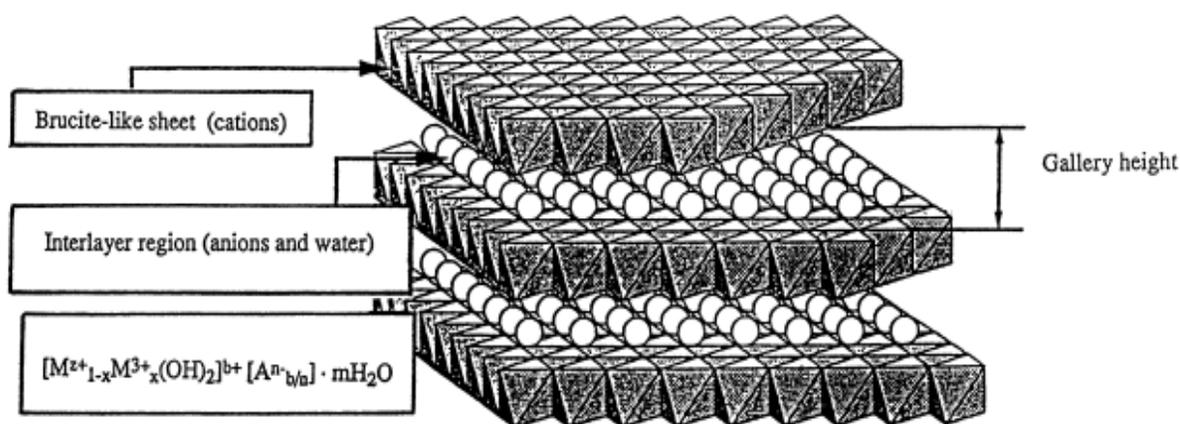
Figure 1. Layered structure of hydrotalcites with rhombohedral symmetry.

compound stabilisers.

A current additive, such as lead stearate $[Pb(C_{17}H_{35}COO)_2]$, is used to quench the evolved HCl gas, which results in the formation of lead (II) chloride, as illustrated in Scheme 1, where lead chloridostearate was formed as an intermediate product and stearic acid served as a catalyst (Kalouskova et al., 2004). Lead stearate readily reacts with the evolved HCl gas and favourably affects the stability of PVC. However, the main concern is that the $PbCl_2$ formed as a product can leach into the environment as the polymer degrades. This is extremely harmful to the environment and the public because exposure to $PbCl_2$ is a common source of lead poisoning. This is another reason why alternatives need to be investigated. In this study, the use of hydrotalcites (HTs) as a lead replacement stabiliser in PVC processing was investigated. The general formula for HTs is represented by Equation 1, where M^{2+} and M^{3+} represent divalent and trivalent cations respectively (Morioka et al., 1995; Borja and Dutta, 1992; Lin et al., 2006; Yong and Rodrigues, 2002; Tong et al., 2011).

$$[M^{2+}_{1-x}M^{3+}_x(OH)_2](A^{n-})_{x/n} \cdot mH_2O \qquad (1)$$
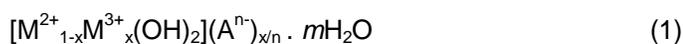
The synthesis of HTs involves the formation of positively charged (cations) layers and filling the interlayer region with anions. During this process, the initial solution contains carbonate and hydroxide ions. The metal ions are later added to this solution and bonds to the hydroxide ions to form the metal-hydroxide layers (indicated as 'brucite-like sheet' in Figure 1).

According to Gupta et al. (2008, 2009), the reaction between an Mg/Al-based HT and HCl gas is shown in Scheme 2. In comparison to lead stearate in Scheme 1, no harmful products are formed when an Mg/Al-HT reacts with the evolved HCl gas. This shows that HTs are more favourable (in terms of environmental health and safety) to use as stabilisers in the manufacturing of PVC polymeric products. In order to determine how HTs enhance the stability of PVC during degradation, synthesised HTs were used to quench HCl gas evolved as a result of thermal processing of PVC. Under conditions of elevated temperatures and UV radiation, PVC undergoes dehydrochlorination, where the evolved HCl gas is a polar covalently bonded gas. Signs of degradation during dehydrochlorination are apparent as severe discolouration of the PVC sample occurs. In this

$$PVC\ (s) \xrightarrow{\text{dehydrochlorination}} PVC(s) +\ HCl\ (g) \xrightarrow{\quad Mg\text{-}A\ell\text{-}CO_3.mH_2O \quad}$$

$$Mg\text{-}A\ell_2Cl_2CO_3.mH_2O(s) + H_2O(\ell) + CO_2(g)$$
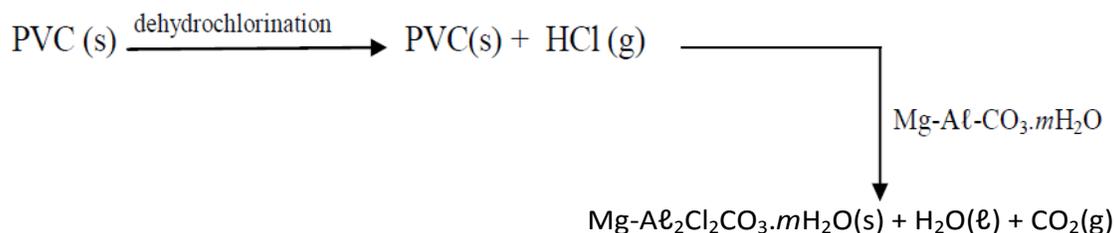
Scheme 2. Behaviour of a Mg/Al-Hydrotalcite during the degradation of PVC.

study, results from the dehydrochlorination and thermogravimetric analysis performed on the PVC and HTs, will show that the synthesised HTs (as heat stabilisers) can inhibit the degradation of PVC by quenching the evolved HCl gas.

Lin et al. (2005) in Gupta et al. (2008), van der Ven et al. (2000) and Kalouskova et al. (2004) have also used HTs as heat stabilisers in PVC processing and suggested that a possible reason for its stabilising properties is due to ion exchange, where CO_3^{2-} ions are replaced by the absorbed Cl^- ions. Contrary to Lin et al. (2005) and Kalouskova et al. (2004) findings, Gupta et al. (2008, 2009) reported that besides ion exchange, adsorption of the evolved HCl gas by HTs is a major factor in the stabilisation of PVC.

The phenomena of adsorption can only be explained, according to Gupta et al. (2009), if the chloride ions on the surface of the HT are adsorbed, instead of exchanged with the carbonate ions. A possible mechanism for scavenging the evolved HCl gas using HTs was suggested by Gupta et al. (2008, 2009). Ion exchange is likely to occur if the chlorine atoms from the HCl are converted into Cl^- ions, however in the gaseous state this is least likely to occur. As a result, it is the surface adsorption of HCl gas onto the HTs that plays a significant role in heat stabilisation.

The research undertaken aims to explore the stabilising effect on PVC products during thermal processing using synthetic hydrotalcites.

MATERIALS AND METHODS

Synthesis of hydrotalcites

The metal solution, containing 0.75 M magnesium nitrate, zinc nitrate and/or aluminium nitrate, was transferred to the carbonate solution, containing 0.5 M sodium carbonate, using a burette at room temperature. This was conducted at a flow rate of ~1.0 mL/min under constant stirring. The pH was maintained between 11 and 12, by adding 2 M NaOH. Once the transfer was complete, the resulting mixture was stirred for 1.5 h at room temperature. The resulting metal/carbonate mixture was refluxed at 80°C, in an oil bath for 18 h, cooled to room temperature and filtered under a vacuum. The precipitate obtained was rinsed several times with deionised water and dried overnight at 110°C.

Characterisation

FT-IR spectroscopy

All FT-IR spectra were recorded on a Perkin Elmer Spectrum 100 FT-IR Spectrometer with a universal ATR sampling accessory. The spectrum was recorded in the range of 4000-400 cm^{-1}.

Chemical analysis

To analyse the metal ions using ICP-OES, into a 50 mL centrifuge tube, 200 mg of each HT was accurately weighed and to it, 10 mL of aqua regia (3 parts HCl, 1 part HNO_3) was added. These tubes were sealed and placed on an orbital shaker for 2 h, centrifuged for 5 min then decanted into 100 ml volumetric flasks. The samples were filtered (by gravity) as it passed into the flasks and dilute to 100 mL with deionised water. These samples were prepared in triplicate and were analysed by a Perkin Elmer Optical Emission Spectrometer. The percentage of carbon, hydrogen and nitrogen present in the HTs was determined by accurately weighing approximately 2 mg of HT into a pre-shaped casing, closed and pressed into a pellet then analysed by a LECO CHNS-932 elemental analyser.

Physical analysis: PXRD, Surface area and pore volume

Powder X-Ray Diffraction (PXRD) studies was conducted on a Bruker AXS Diffraktometer D8, at room temperature, where a PXRD pattern with d-values was obtained using a scan range between 10 and 90° 2θ (theta) and a step width of 0.014°. The unit cell values were determined by the following equation:

$$\sin^2\theta = (\lambda^2/4a^2) \times N \quad [12] \tag{2}$$

Determination of surface area and pore volume of the HTs was obtained using a Perkin Elmer instrument with Gemini 2375 V5.00 software.

Thermogravitmetric analysis

This analysis was performed by a SDT Q600 Thermogravimetric analyser, under nitrogen (100 mL/min) from 50 to 700°C at a heating rate of 10°C/min, where approximately 20 mg of sample was required. The HT and PVC powder were analysed individually, followed by the PVC-HT samples prepared by mixing 10 g of PVC powder and 200 mg of the synthesised HTs. From this analysis, a thermogram was obtained illustrating the sample's weight loss, derivative weight and heat flow as a function of temperature.

Dehydrochlorination

This is a thermal stabilising efficiency test, where the efficiency of the HT's ability to quench the evolved HCl was determined. Samples were placed in a round bottom flask and heated at 180°C in an oil bath, under a steady flow of nitrogen (60 mL/min). The HCl gas evolved was collected in a 100 mL Erlenmeyer flask, which was placed at the end of the condenser containing 50 ml of 4 μM NaOH solution with phenolphthalein indictor. The time taken for 0.2 μmol of HCl gas to evolve was recorded.

RESULTS AND DISCUSSION

The method for synthesising HTs is a well-established technique, and in this study the co-precipitation method was employed, which yielded a white precipitate in all cases. Our laboratory yields for all HTs ranging from 17 to 24% are considered low in comparison to yields recorded by others ranging from 80 to 90% (Mohan et al., 2005). According to Kloprogge et al. (2004a), HTs synthesised at pH 12 are more highly crystalline than the HTs synthesised at pH values other than 12. Thus, pH 12 was used as a standard bench mark for the synthesis of HTs in this study. However, according Vaccari et al. (1998), a pH range of 8-10 is also considered suitable for the synthesis of HTs. It is therefore possible that should a pH range of 8-10 be used, a higher yield of HTs would result, consequently, with a possible variation in the degree of crystallinity.

The use of FT-IR spectroscopy (generally used to identify the functional groups present in a HT structure composed of two or three metals) showed a broad band at ~3400 cm^{-1}, which is assigned to the stretching of the O-H bonds in the brucite-like sheets (Figure 1) in all six samples. However, a shift of this OH band to a higher wavenumber with increasing M^{2+}/M^{3+} ratios (HT 2 > HT 1 and HT 4 > HT 3) was observed. This is possibly due to a decrease in ionic radius across a period (from left to right) and an increase down a group (Zn^{2+} = 0.74 Å, Mg^{2+} = 0.65 Å, Al^{3+} = 0.50 Å). As a result, the electrostatic forces between Al^{3+} and OH^- (1:3) are stronger than that between Mg^{2+} or Zn^{2+} and OH^- (1:2). As the metal/hydroxide ion ratios decrease, less electrostatic forces are present, thus resulting in the hydroxide ions vibrating at higher wavenumbers.

As the number of metal ions in synthesised HTs were increased, the IR bands were observed at higher wavenumbers (Mg/Zn/Al-HT > Mg/Al-HT > Zn/Al-HT). Although Zn has a greater ionic radius than Mg, it is a transition metal with a completely filled d-orbital. Thus the electrostatic forces between Zn^{2+} and OH^- would be stronger than Mg^{2+} and OH^-, resulting in the O-H stretch of Zn-containing HTs vibrating at a slightly lower wavenumber than the initially observed 3400 cm^{-1}. The band observed at 3459.19 cm^{-1} was due to HT 5, which contained more Mg ions than Zn. All synthesised HTs showed two weak bands occurring as shoulders at ~2900-3000 cm^{-1} and ~1620 cm^{-1} respectively (as a result

Table 1. Ratios of metals ions present in HTs synthesised determined by ICP-OES.

HT	Calculated ratios (Mg^{2+}:Zn^{2+}:Al^{3+})	Experimental ratios (Mg^{2+}:Zn^{2+}:Al^{3+})
1	4 : 0 : 2	4 : 0 : 2
2	6 : 0 : 2	6 : 0 : 2
3	0 : 4 : 2	0 : 5 : 1
4	0 : 6 : 2	0 : 7 : 1
5	4 : 2 : 2	4 : 3 : 1
6	2 : 4 : 2	2 : 5 : 1

of the low percentage yields). The first according to Kloprogge and co-workers et al. (2004b) is due to the CO_3-H_2O bridging vibrations, and the second is assigned to the bending modes of H_2O caused by the hydrogen bonding between the molecules.

The carbonate ions found in the interlayer region of the HT structure shown in Figure 1 is indicative of a sharp intense band at ~1360 cm^{-1} due the antisymmetric stretching. For all synthesised HTs, three FT-IR bands were observed in the fingerprint region at ca. 550 cm^{-1}, ca. 630 cm^{-1} and ca. 770 m^{-1}. These bands are typically found in HTs and are due mainly to the lattice and translational vibrations of the metal ions, or the flexural vibrations of CO_3^{2-} (that is, 'rocking' of the molecule) (Seftel et al., 2005). A sharp band observed at approximately 440 cm^{-1}, is due to the lattice vibration of Al^{3+} which was observed in HT 1 and 6 only. Hence, it can be deduced that all relevant functional groups for example, CO_3^{2-} and OH^- are present in HTs synthesised. Also the addition of Zn to the Mg/Al-HT did not result in any major variation in the IR bands observed.

The concentration of metal ions in HTs was determined from the relative intensities of metal ions using ICP-OES. The calculated and experimental values for the metal ion ratios in Mg/Al-HTs shown in Table 1 were found to be the same. However, laboratory synthesised Zn-containing HTs are found to contain one more Zn atom than the calculated amount. This results in one less Al atom being present in the Zn-containing HTs. It was suggested by Rajamathi et al. (2001) that Zn^{2+} ions occupy the tetrahedral as well octahedral sites in the layered structure. This can lead to competition between the Al^{3+} and Zn^{2+} ions for the tetrahedral sites in the structure.

From the C, H, N instrumental analysis, nitrogen, as expected, was absent in all HTs synthesised. This indicates that all nitrates were successfully removed from the precipitate during the washing stages using deionised water. Applying the general formula for HTs (Equation 1) theoretically and calculating it experimentally from C, H, N analysis, all synthesised HTs were found to contain one carbon atom. The variation of the number of hydrogen atoms in each HT, based on predicted and calculated results indicate that the amount of water

Table 2. Chemical formulae of synthesised HTs determined theoretically and experimentally.

HT	Calculated chemical formula	Actual chemical formula
1	$Mg_4Al_2(OH)_{12}CO_3.3H_2O$	$Mg_4Al_2(OH)_{12}CO_3.4H_2O$
2	$Mg_6Al_2(OH)_{16}CO_3.4H_2O$	$Mg_6Al_2(OH)_{16}CO_3.4.5H_2O$
3	$Zn_4Al_2(OH)_{12}CO_3.3H_2O$	$Zn_5Al(OH)_{12}CO_3.3H_2O$
4	$Zn_6Al_2(OH)_{16}CO_3.4H_2O$	$Zn_7Al(OH)_{16}CO_3.3.5H_2O$
5	$Mg_4Zn_2Al_2(OH)_{12}CO_3.3H_2O$	$Mg_4Zn_3Al(OH)_{12}CO_3.8H_2O$
6	$Mg_2Zn_4Al_2(OH)_{12}CO_3.3H_2O$	$Mg_2Zn_5Al(OH_{12}CO_3.6.5H_2O$

molecules in the interlayer region does not correlate to the expected values. Therefore from chemical analyses, the synthesised HTs were found to have an experimentally determined chemical formula (Table 2) that varied from the theoretically calculated formula.

In order to establish which HT that has the potential to function as an effective heat stabiliser for PVC, its physical properties needs to be investigated and considered. The crystalline or amorphous structural identification of HTs were investigated by PXRD (Figure 2a-f). In addition, the surface area and pore volume, from BET surface area analysis, is a direct indication of the synthesised HTs ability to quench the HCl gas.

According to Bastiani et al. (2004), broad and narrow symmetrical peaks observed in PXRD for HTs is a characteristic feature of a layered crystal structure HT. The PXRD patterns (Figure 2) obtained for all synthesised HTs in this study showed a similar trend thus confirming the formation of a layered crystal structure. The unit cell values calculated (Equation 2) for HTs synthesised in this study correlated to the literature value of 3.054 Å (Cavani et al., 1991). This confirms the rhombohedral symmetry in the layered structures of Mg/Al-HTs, with some variations in the Zn-containing HTs. The variations in the Zn-containing HTs may be attributed to a large cationic distance between Zn^{2+} ions. Consequently, the Zn-containing HTs were found to have a smaller pore volume than the Mg/Al-HTs, which was confirmed by BET surface area analysis (Table 3). Kloprogge et al. (2004) suggested that the higher the degree of crystallinity of the HT structure, the higher its thermal stability. However, the degree of crystallinity of the synthesised HTs using data obtained from PXRD patterns was uncertain.

The Mg/Al-HTs were found to have a larger surface area and pore volume, in comparison to the other HTs synthesised. From the BET surface area results, it is observed that the surface area and pore volume of the Mg/Al-HTs are much larger than the Zn-containing HTs. This suggests that the Mg/Al-HTs can act as an effective adsorbent, which is consistent with its industrial applications, and would be an ideal heat stabiliser for PVC. Therefore from the physical properties investigated,

the Mg/Al-HTs are most favourable to show an inhibition of the degradation of PVC during thermal gravimetric analysis (TGA) and dehydrochlorination.

From the TGA analysis, thermograms showed three distinct (temperature ranges 25-230°C, 230-450°C and 450-700°C) of weight loss. Since all synthesised HTs are highly crystalline (according to the PXRD results) and comprised of the same anions, any variation in the temperature range was therefore due to the different metal ion ratios. This was suggested by Rao et al. (2005) who indicated that HTs generally undergo two weight losses around 270 and 450°C, which depend qualitatively and quantitatively on many factors such as crystallinity, type of anions (Borja and Dutta, 1992), as well as nature and relative amounts of cations (Vaccari, 1998). Two sample weight losses are evidently present in the thermograms (Figure 3) for Mg/Al-HTs, verifying the formation of the layered structure illustrated in Figure 1. The thermograms for the Zn-containing HTs showed only one major loss in weight between 25-230°C, while PVC decomposed completely with two major weight losses between 230-500°C (Figure 4).

According to TGA-MS studies on HTs, the temperature at which the weight losses occur, suggest that the first weight loss corresponds to the loss of water molecules (Gupta et al., 2009; Lin et al., 2005; Mohan et al., 2005; Kloprogge et al., 2004a) present in the interlayer region. Upon further heating the second weight loss (subsequent to the first weight loss) involve dehydroxylation of the brucite-like sheets (Figure 1), as well as the removal of the carbonate anions as confirmed by Kloprogge et al. (2004a). The derivative weight loss curves for HTs 3, 4, 5 and 6, show only one major mass change, which resulted in a low total weight loss (reported in Table 4), as suggested by Cavani et al. (1991), who found that the carbonate ions can be removed from the interlayer without destroying the structure of the HTs.

Further results from TGA showed that HTs 1 and 2 were most stable compared to the rest of them. It was found that HTs 1 and 2 decomposed at 250 and 225°C respectively, while HTs 4 and 5 decomposed at lower temperature of 205°C. A higher thermal stability of HTs 1 and 2 is inherent arising out of their composition made up mainly of $Mg(OH)_2$ and $Al(OH)_3$ (which decompose at 350 and 300°C, respectively). As a result, the Mg/Al-HTs are mostly likely to be better heat stabilisers than Zn-containing HTs (comprising mainly of $Zn(OH)_2$ which decomposes at 125°C) (Cavani et al., 1991), as indicated by BET surface area analysis. Thermograms generated for HTs 1 and 2 were the only compounds which corresponded to data reported by Rao et al. (2005), Gupta et al. (2009), Lin et al. (2006) and Kloprogge et al. (2004) thus confirming high thermal stability over other HT's synthesised. Therefore based on derivative weight loss, HTs in order of increasing thermal stabilities are:

HT 4 ≈ HT 5 < HT 3 < HT 6 < HT 2 < HT 1

(a)

(b)

(c)
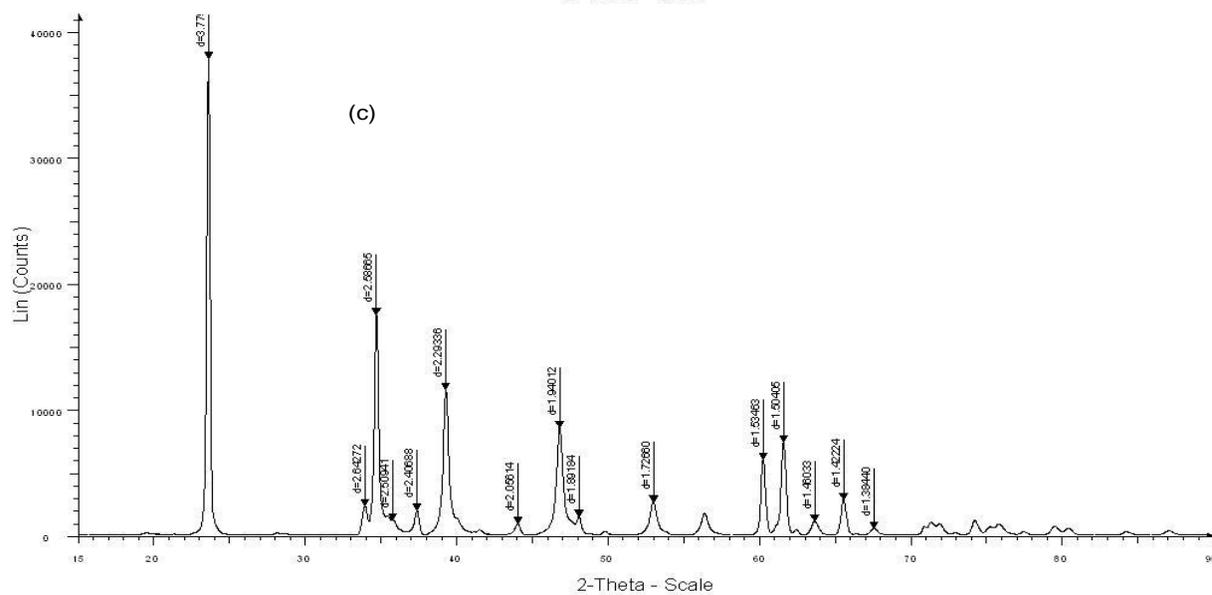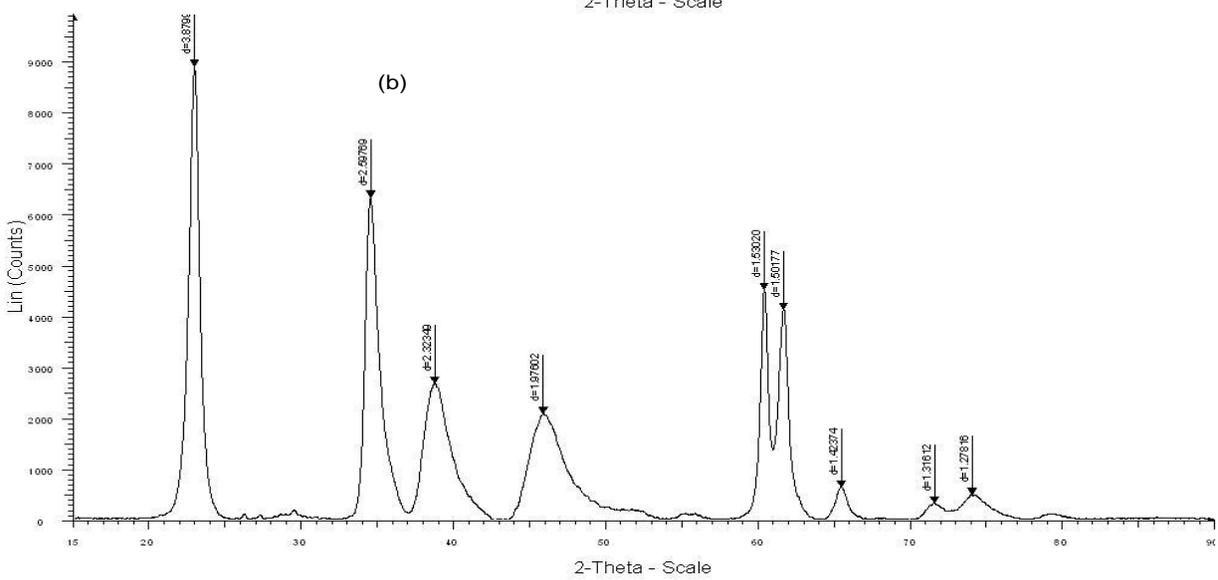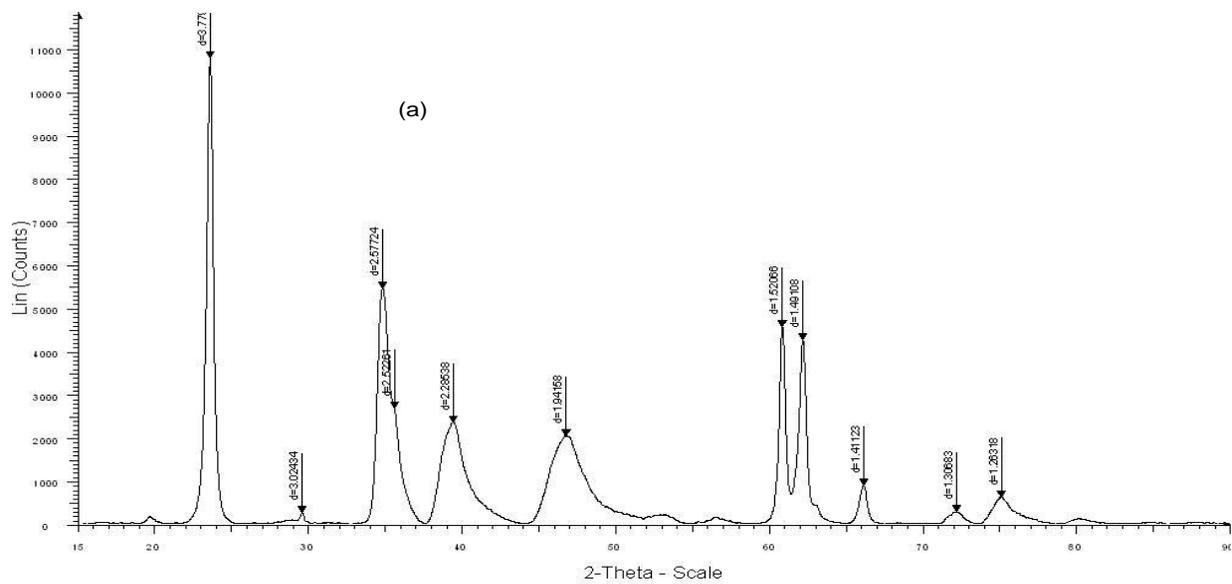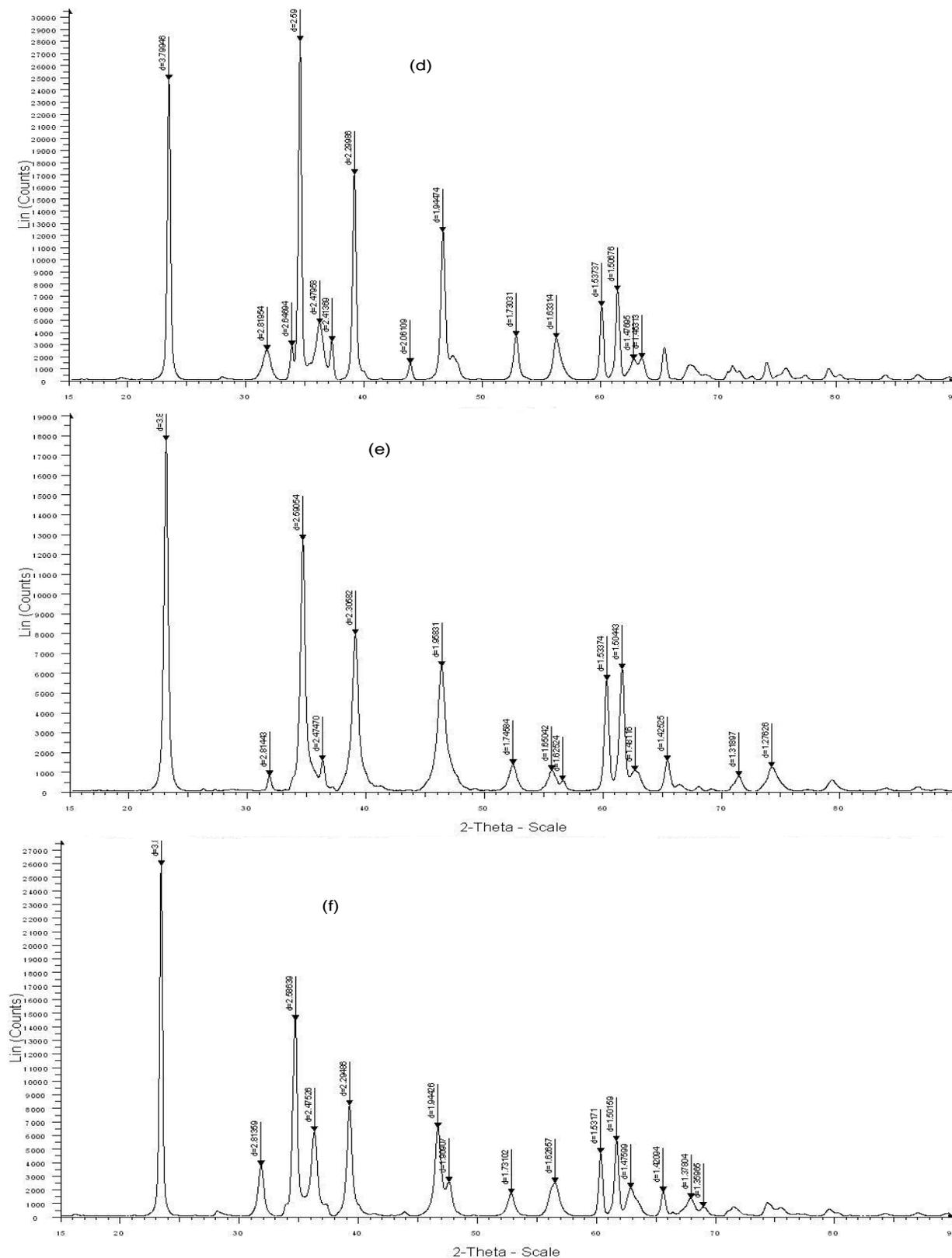
Figure 2. PXRD patterns obtained for HT's. (a) PXRD pattern obtained for $Mg_4Al_2(OH)_{12}CO_3.3H_2O$, (b) PXRD pattern obtained for $Mg_6Al_2(OH)_{16}CO_3.4H_2O$, (c) PXRD pattern obtained for $Zn_4Al_2(OH)_{12}CO_3.3H_2O$, (d) PXRD pattern obtained for $Zn_6Al_2(OH)_{16}CO_3.4H_2O$, (e) PXRD pattern obtained for $Mg_4Zn_2Al_2(OH)_{12}CO_3.3H_2O$, (f) PXRD pattern obtained for $Mg_2Zn_4Al_2(OH)_{12}CO_3.3H_2O$.

Table 3. Surface area and pore volume obtained for HTs synthesised.

HT	Sample mass / mg	Surface area / $m^2 g^{-1}$	/ m^2	Pore volume / $cm^3 g^{-1}$	/ dm^3
1	15.5	88.7000	1.375	0.5476	8.49
2	19.6	103.7092	2.033	0.5205	10.2
3	15.2	69.1270	1.051	0.0639	0.97
4	17.5	42.4833	0.743	0.1058	1.85
5	18.7	48.6898	0.910	0.2112	3.95
6	19.8	24.4649	0.484	0.0593	1.17
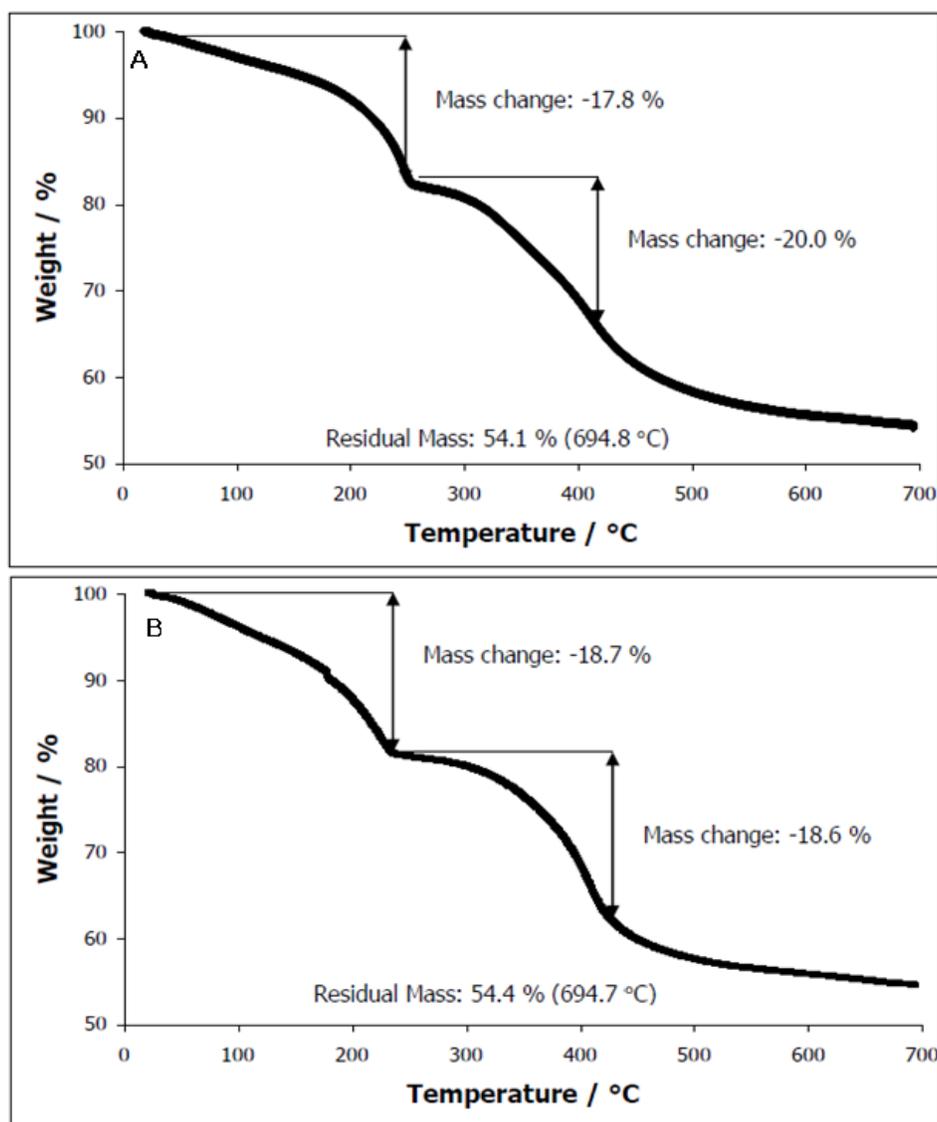
Figure 3. Thermograms for (A) Mg_4Al_2-HT and (B) Mg_6Al_2-HT.

Heating of the PVC powder, resulted in the evolution of HCl gas at temperatures greater than 180°C. From the thermogram for PVC (Figure 4), it was evident that the structure of PVC becomes unstable due to its facile
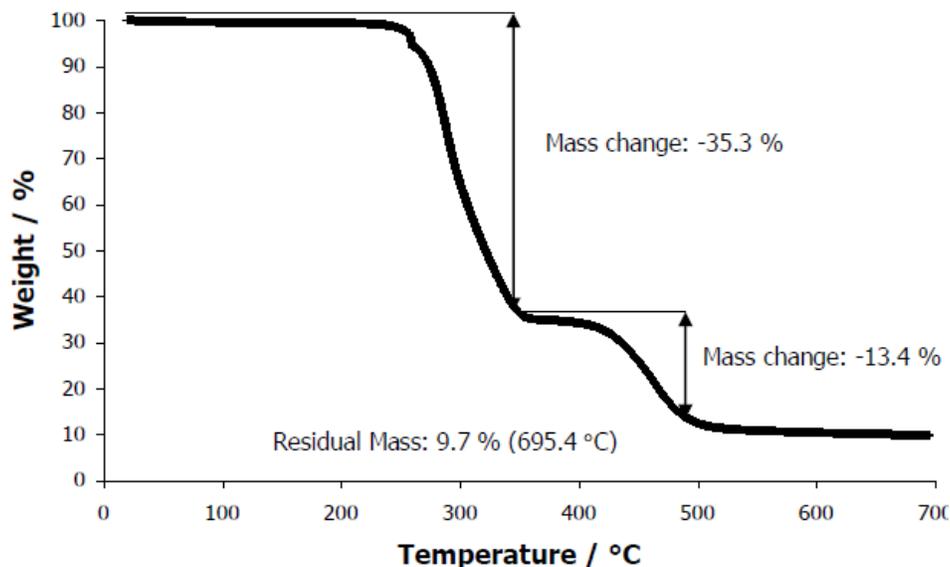
Figure 4. Thermogram for PVC.

Table 4. TGA data obtained for HTs and PVC.

Samples	Temperature / °C	Weight loss / %	Total weight loss / %
HT 1	250; 415	17.8; 20.0	45.9
HT 2	225; 415	18.7; 18.6	45.6
HT 3	215	18.0	33.0
HT 4	205	15.1	27.3
HT 5	205	15.0	37.6
HT 6	220	13.5	29.8
PVC	300; 460	35.3; 13.4	90.3

decomposition observed between 250-350°C. The process of dehydrochlorination (release of HCl gas from PVC) accelerates the degradation of PVC as observed from the continuous weight loss up to approximately 500°C. For this reason, heat stabilisers are an essential part of the PVC industry to prevent subsequent decomposition of the polymer upon heating. Potential inhibition of degradation of PVC by synthesised HTs is clearly evident from their characterisation using TGA, PXRD and BET surface area analysis. This can also be confirmed by the fact that at 700°C, all HTs maintained at least 50% of residual mass, indicating favourable thermal stability properties of the structure.

Since thermal stability is temperature dependant, the most stable synthesised HTs appear to be HT 4 and 6 showing lowest total weight loss (Table 4). However, the BET surface area results suggest that HTs 4 and 5 are most unlikely to quench the evolved HCl gas, due to its small pore volumes and surface areas. Although HT 4

and 6 show high thermal stability from the TGA results, it is the HTs ability to quench the HCl gas that is of importance to this study. Therefore from this analysis, it was observed that the HT thermal stability in increasing order is as follows:

HT 1 ≈ HT 2 < HT 5 < HT 3 < HT 6 < HT 4

The results of dehydrochlorination are reported in Table 4, where all samples were analysed under the same conditions. A blank analysis, containing PVC only, showed signs of degradation (decolourised to light brown) after 5 min. The Mg/Al-HTs (0.2 g) showed the highest thermal stabilisation by delaying the degradation of 10 g of PVC powder by 14 to 15 min in comparison to the blank analysis, where the PVC completely degraded after 12 min. Such results are consistent with the BET surface area results, where the Mg/Al-HTs had the largest surface areas and pore volumes. Therefore, the Mg/Al-HTs would be able to quench the most HCl gas in comparison to the other HTs synthesised.

PVC samples containing HTs 3 and 4 were the only samples to turn black after a short time, while all the other samples decolourised to light brown. This shows that Zn did not offer any stability towards the PVC, as the PVC-HT 6 sample degraded the fastest at 6.45 min. Therefore, the PVC samples containing HTs 3, 4 or 6 instability is consistent with the small surface area and pore volume observed. The time taken for the PVC samples containing HTs 3, 4 or 6 to degrade was less than the PVC containing no HTs. It can be suggested that the reason for the PVC samples containing HTs 3, 4 or 6 not being stable for at least 12 min was due to the extra Zn atom present in the HT, reported in Table 1.

Table 5. Adsorption rate of 0.2 μmol evolved HCl gas (dehydrochlorination) by HTs at 180°C.

Samples	Degradation Time/ mins	Observations
PVC (Blank)	12.00	Sample decolourised to light brown after 5 minutes.
PVC-HT 1	26.45	Sample decolourised partially from white to light brown.
PVC-HT 2	28.20	
PVC-HT 3	12.51	Sample turned black after 11 minutes.
PVC-HT 4	8.30	Sample turned black with fumes of HCl rapidly being given off after 8 minutes.
PVC-HT 5	12.42	Sample decolourised partially from white to light brown.
PVC-HT 6	6.45	
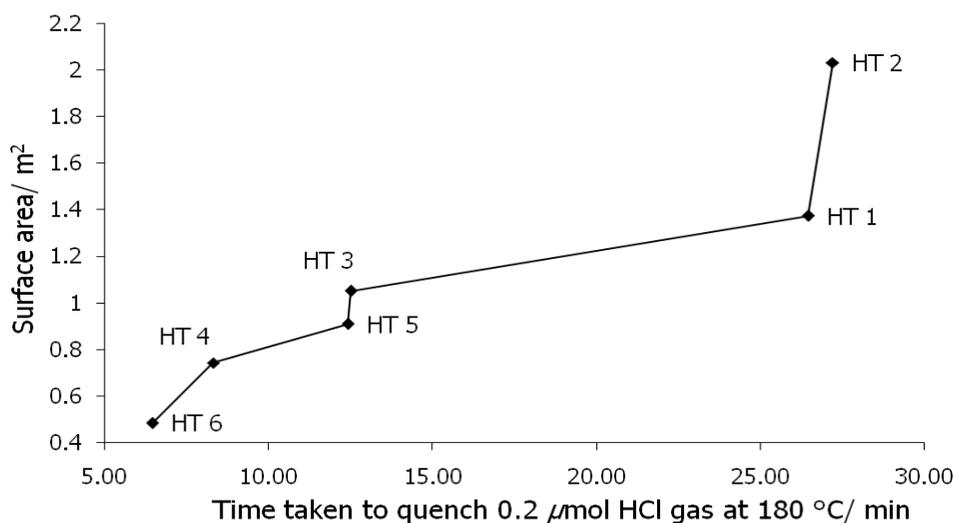
Figure 5. Correlation between the BET surface area and dehydrochlorination results obtained.

From the BET surface area and TGA results obtained, it is possible to assume that HT 3, 4, 5 and 6 did not form the expected layered structure and therefore a second weight loss was not observed on each thermogram recorded. Further investigation is deemed necessary to elucidate the structure of HTs 3, 4, 5 and 6. Although PVC-HT 5 has a small surface area and pore volume relative HTs 1 and 2, but larger than HTs 3, 4 or 6, showed signs of stabilising the PVC for approximately 42 seconds due to the presence of Mg in the HT. The observed thermal stability of synthesised HT from this analysis in order of increasing ability to stabilise the PVC is: HT 6 < HT 4 < HT 5 < HT 3 < HT 1 < HT 2.

It is also envisaged from the results obtained that the type of metal ions present in a synthesised HT has a significant effect on the thermal stability of PVC during dehydrochlorination as observed from the adsorption rate of evolved HCl gas shown in Table 5. This is confirmed by the relatively linear relationship between the HTs surface area and its ability to inhibit the degradation of PVC (Figure 5). Surface adsorption and not absorption,

according to Figure 5, is the mechanism in which Mg/Al-HTs quench evolved HCl gas. Stabilisation of PVC by HT 3 was more effective than HT 4 due to its surface area rather than to its pore volume. HT 2 was found to have the largest surface area over all synthesised HTs and consequently was the most effective in stabilising the PVC powder. HT 6 was found to have the smallest surface area and as a result, did not stabilise the PVC at all. Hence from the HTs synthesised in this study, HT 2 ($Mg_6Al_2(OH)_{16}CO_3.4H_2O$) has proven to be the most effective heat stabiliser in processing of PVC to useful polymeric products.

Conclusion

The results from this study show that Mg/Al-HTs have proven to potentially function as ideal heat stabilisers in processed PVC products. From the PXRD studies, it can be confirmed that the Mg/Al-HTs synthesised in this study were the only HTs which formed layered structures with

rhombohedral symmetry. A combination of favourable properties, such as a large surface area confirmed by the BET surface area analysis, thermal stability and quenching ability of a PVC-HT blend determines the inhibition potential of dehydrochlorination. The addition of Zn to the Mg/Al-HT did not benefit the HT and in fact accelerated the degradation of PVC during dehydrochlorination. Mg/Al-HTs were able to adsorb 0.2 μmol of HCl gas evolved during the degradation of PVC and significantly delayed the onset of degradation of PVC relative to the other HTs synthesised, including the non-stabilised PVC sample. Therefore scavenging of HCl gas by synthesised Mg/Al-HTs in this study has shown an increase toward the inhibition of degradation and thermal stability of PVC during its processing.

REFERENCES

Bastiani R, Zonno IV, Santos IAV, Henriques CA, Monteiro JLF (2004). Influence of thermal treatments on the basic and catalytic properties of Mg, Al-mixed oxides derived from hydrotalcites. Brazilian J. Chem. Eng. 21(2):193-202.

Borja M, Dutta PK (1992). Fatty acids in layered metal hydroxides; membrane-like structure and dynamics. J. Phys. Chem. 96(13): 5434-5444.

Cavani F, Trifiro F, Vaccari A (1991). Hydrotalcite-type anionic clays: preparation, properties and applications. Catalysis today. 11(2):176-190.

Gupta S, Agarwal DD, Banerjee S (2008). Synthesis and characterization of hydrotalcites: Potential thermal stabilizers for PVC. Indian J. Chem. 47A:1004-1008.

Gupta S, Agarwal DD, Banerjee S (2009). Thermal stabilization of poly (vinyl chloride) in presence of hydrotalcites, Zeolites and conventional stabilizer system. J. Vinyl Additive Technol. 15:164-170.

Haynes D (2007). Materials Practical Manual - APCH 312. 2007, P. 19.

Kalouskova R, Novotna M, Vymazal Z (2004). Investigation of thermal stabilization of poly(vinyl chloride) by lead stearate and its combination with synthetic hydrotalcite, Polymer Degradation and Stability. Polymer Degradation and Stability, 85:903-909.

Kloprogge JT, Hickey L, Frost RL (2004a). The effects of synthesis pH and hydrothermal treatment on the formation of zinc aluminum hydrotalcites. J. Solid State Chem. 177:4047-4057.

Kloprogge JT, Hickey L, Frost RL, Raman J (2004b). FT-Raman and FT-IR spectroscopic study of the local structure of synthetic Mg/Zn/Al-hydrotalcites. Spectroscopy, 35:967-974.

Lin Y, Wang J, Evans DG, Li D (2006). Layered and intercalated hydrotalcite-like materials as thermal stabilizers in PVC resin. J. Phys. Chem. Solids, 67:998-1001.

Lin YJ, Li DQ, Evans DG, Duan X (2005). Modulating effect of Mg–Al–CO_3 layered double hydroxides on the thermal stability of PVC resin. Polymer Degradation and Stability, 88:286-293.

Mohan RM, Ramachandra RB, Jayalakshmi M, Swarna JV, Sridhar B (2005). Hydrothermal synthesis of Mg–Al hydrotalcites by urea hydrolysis. Mater. Res. Bulletin, 40:347-359.

Morioka H, Tagaya H, Karasu M, Kadokawa J, Chiba K (1995). Preparation of new useful materials by surface modification of inorganic layered compound. J. Solid State Chem.117:337-342.

Rajamathi M, Thomas GS, Kamath PV (2001). The many ways of making anionic clays. Proceedings of the Indian national Academy of Sciences (Chemistry Sciences). 113(5-6):671-680.

Seftel EM, Dvininov E, Lutic D, Popovici E, Ciocoiu C (2005). Synthesis of hydrotalcite-type anionic clays containing biomolecules. Optoelectronics Adv. Mater. 7(6):2869-2874.

Tong M, Chen H, Yang Z, Wen R (2011). The Effect of Zn-Al-Hydrotalcites Composited with Calcium Stearate and β-Diketone on the Thermal Stability of PVC. Int. J. Molecular Sci. 12:1756-1766.

Vaccari A (1998). Preparation and Catalytic properties of cationic and anionic clays. Catalysis Today. 41:53-71.

van der Ven L, van Germert MLM, Batenburg LF, Keern JJ, Gielgens LH, Koster TPM, Fischer HR (2000). On the action of hydrotalcite-like clay materials as stabilizers in poly(vinyl chloride. Appl. Clay Sci. 17:25-34.

Yong Z, Rodrigues AE (2002). Hydrotalcite-like compounds as adsorbents for carbon dioxide. Energy Conver. Manage. 43:1865.

Full Length Research Paper

Excessive correlated shifts in pH within distal solutions sharing phase-uncoupled angular accelerating magnetic fields: Macro-entanglement and information transfer

Blake T. Dotta, Nirosha J. Murugan, Lukasz M. Karbowski and Michael A. Persinger

Biophysics Section, Biomolecular Sciences Program, Laurentian University Sudbury, Ontario, Canada.

Entanglement or "excess correlation" between physical chemical reactions separated by significant distances has both theoretical and practical implications. In 24 experiments, the inverse shifts in pH were noted in two quantities of spring water separated by 10 m that shared rotating magnetic fields (0.5 μT) with changing angular velocities when one solution was injected with proton donors (weak acetic acid). The values of increased pH in the "entangled" (non-injected) beakers were 0.01, 0.03, and 0.07 for water volumes of 100, 50, and 25 cc, respectively. The associated fixed amount of energy of ~10^{-21} J per molecule from the coordinated fields in the two loci was related to the change in numbers of H^+ within these volumes and predicted the time required to produce the maximum shift in pH. These results suggest that macroentanglement as a potentially inexpensive method of transfer of information over long distances may have practical application.

Key words: Convergent loci, entanglement, weak magnetic fields, pH, communications.

INTRODUCTION

Demonstration of macroentanglement for discrete reactions over non-traditional distances that do require conventional electromagnetic transmission has significant practical importance for future, inexpensive and private modes of communication. Although there have been elegant demonstrations of entanglement involving electron spins and gases (Ahn et al., 2000; Fickler et al., 2012; Hoffman et al., 2012; Julsgaard et al., 2001), the equipment is expensive and limited in availability. Dotta and Persinger (2012) reported that two photochemical reactions separated by 10 m but that shared identical circular rotating magnetic fields whose phase and group velocities were uncoupled, to satisfy the conditions calculated by Tu et al. (2005), responded as if the two separate spaces were the same locus. Simultaneous injection of single reactants in the solutions in the separate spaces produced a doubling of photon emissions as measured by photomultiplier tubes. The effect, which was visually conspicuous, was equivalent to injecting twice the amount into one reaction. It involved energies in the order of 10^{-11} to 10^{-12} J and was evident at distances of 3 km. Separate studies suggested that similar effects are demonstrable with pairs of cell cultures or human brains (Dotta et al., 2011). Recent source localization from quantitative electroencephalography revealed remarkable excess correlation between brain activities for pairs of individuals separated by about 300 km but who shared the same changing angular velocity circular magnetic fields (Burke et al., 2013).

In the pursuit of understanding the mechanism, we

*Corresponding author. E-mail: mpersinger@laurentian.Ca Fax: 01-705-671-3844.
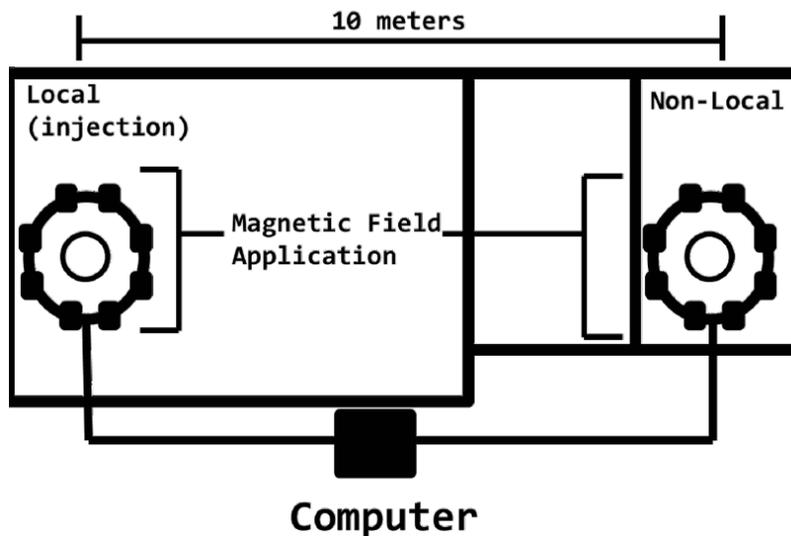
Figure 1. Diagram of the experimental design.

explored less expensive procedures to demonstrate this potent effect. Both theory and calculations indicate that when two spaces share the same configuration of dissociation of phase and group velocity of circularly accelerating or decelerating magnetic fields, a discrete amount of energy is shared. Several of our experiments involving photon transmission through tissue indicated that the hydrogen ion (DeCoursey, 2003), particularly the hydronium atom (H_3O^+), is a primary candidate. In the present experiment, the pH of two solutions separated by 10 m but sharing the same configuration of magnetic fields that was associated with the photon doubling effect were monitored over 20 min after a small amount of proton donor (a weak acid) was injected into one solution. Here we present clear evidence that the injection of a proton donor into one solution produced the predictable decrease in pH that was accompanied by a reliable minute quantitative increase in pH in the distal solution when both shared the same field configuration. This conspicuous effect meets the criteria of excess correlation for macroentanglement and the transfer of a discrete amount of energy over non-traditional distances.

MATERIALS AND METHODS

There were a total of 24 different experiments completed on separate days (one per week). Beakers containing the same volume of spring water, either 25, 50, or 100 cc were placed in the center of each of two circular arrays of 8 coupled solenoids as described by Dotta and Persinger (2012). The equipment is also described in U.S. Patent 6,312,376: b1: November 6, 2001; Canadian Patent No. 2214296. Each pair of solenoids that were reed switches or relays (250Ω) were arranged within small plastic (film) canisters and connected such that they were pairs of north and south poles. The circumference of the equally spaced solenoids that were separated by 45° from each other was ~60 cm.

The flasks containing the water were placed in the middle of the circular arrays (Figure 1) where a power meter indicated the average field strength of the applied fields was 0.5 to 1 µT as measured by a power meter.

This experiment involved exposing the samples of spring water (4 mM of HCO_3; 1.77 mM Ca; 76 µM of Cl; 1.3 mM; of Mg, 41.9; µM of NO_3; 61 µM SO_4 ; 17.9 µM K; 43.5 µM Na) in 125 cc flasks for 18 min to a counterclockwise rotating computer generated magnetic field whose wave pattern (phase) was decelerating while the group velocity (rotation of the wave around the array) was accelerating at 20+2 ms. This means that the duration of the field presentation at each solenoid decreased by 2 ms such that the duration for the first solenoid was 20 ms and 4 ms for the 8th solenoid. After the optimal time of 6 min of this exposure (part 1), the field pattern was changed to an accelerating phase pattern and a decelerating group velocity of 20-2 ms (part 2). This means that 2 ms was added to the duration of the field after the 20 ms at the first solenoid. The second field was applied an additional 12 min. The pH values for both beakers in each experiment were recorded separately once per second by Dr. Daq systems (Pico Technology, United Kingdom) which are sensitive to the .01 pH unit.

There were two separate circular arrangements of 8 solenoids within which the flasks of spring water (circles) were placed. A computer generated the changing angular velocity and phase modulated fields within the two arrays. The proton donor (acetic acid) was injected into the local flask. pH levels were measured every second from the local and the non-local flasks. The latter never received any injections.

After 4 min of exposure to the first field, 50 µl of 0.83 M acetic acid (proton source) was injected into the active beaker. Immediately after the onset of the second field configuration (8 min from the beginning of the experiment), 50 µL was injected into the active beaker once every min until 16th minute of the experiment (9 injections). Nothing was ever injected into the "entangled" beaker. To ensure the specificity of the effect, triplicates of experiments were completed where pH values were monitored in the same manner while the same sequences of injections of protons were injected into the active beaker but no experimental magnetic fields were present. Another triplicate of experiments involved measuring the pH values in both beakers over the same duration when no protons were injected and no fields were present to control for any
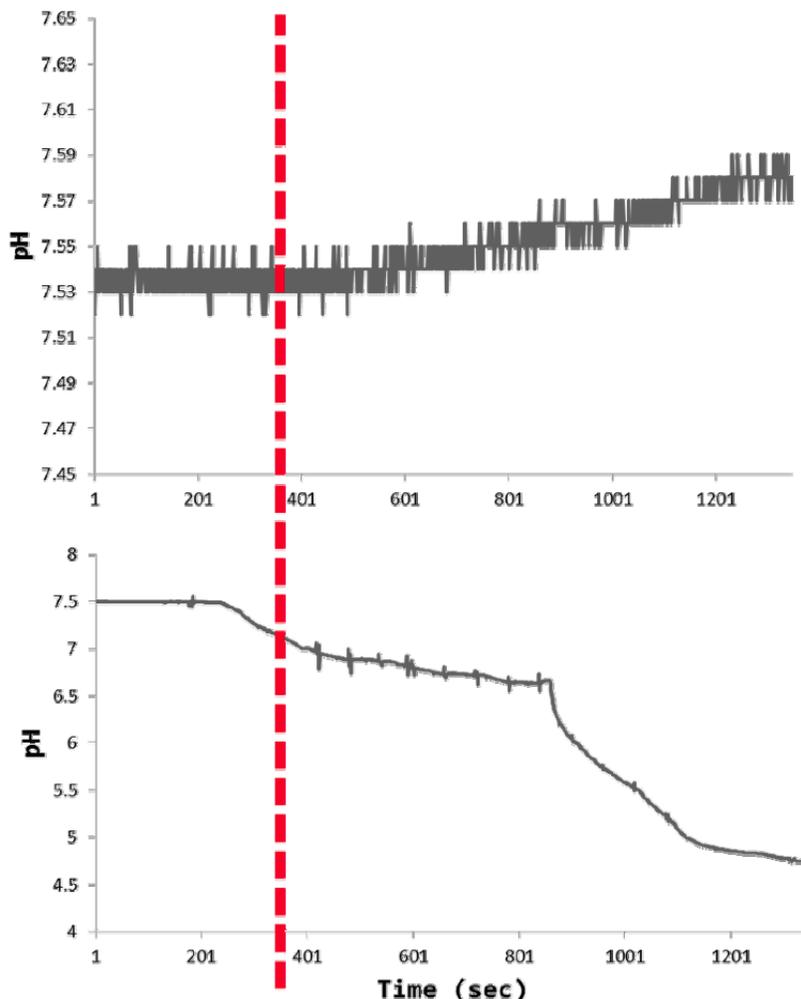
Figure 2. Upper panel: Example of the shift towards basic pH over time (in seconds) in the non-local flask after the initiation of the second component of the magnetic field configuration that was generated at both local and non local spaces. Lower panel: the response to sequential addition of 50 µL of acetic acid (indicated by small spikes) to the local flask during the same time period. Vertical line indicates activation of the "entanglement" field.

serial drift. There was no change in the pH values (flat line) from baseline for any of the pairs of beakers over the 18 min period for these conditions. The net shifts in pH for volume (25, 50, 100 cc of spring water, plus, control) were analyzed by SPSS 16 PC software.

RESULTS

An example of the shifts in pH over time in the non-injected beaker containing 50 cc of spring water that shared the same configuration of circularly rotating magnetic fields as well as the active beaker of spring water that was serially injected with 50 µL of acetic acid 10 m away in a second room is shown in Figure 2. The progressive increases in acidity in the injected beaker is obvious as well as the opposite drift towards basic pH in

the non-injected beaker. The vertical line indicates the activation of the second field whose onset was also associated with the entanglement effect reported by Dotta and Persinger (2012) for photon emissions.

Figure 3 shows the average net change in the pH over time within the non-injected beakers within the different volumes of spring water. Within the 50 cc volumes, the mean total shift (increase) in pH was 0.03 (SEM=0.006). The mean total shift for the 25 cc volumes was pH=0.07 (SEM=0.009). The mean total shift for 100 cc of water (M=0.01, SEM=0.008) did not differ from the control condition (M=0.01, SEM=0.003) when no fields were applied. The difference between the four experimental conditions was statistically significant [$F(3,20)$=23.94, p <.001]; the amount of variance explained, the effect size (eta^2 estimate), was 82%.
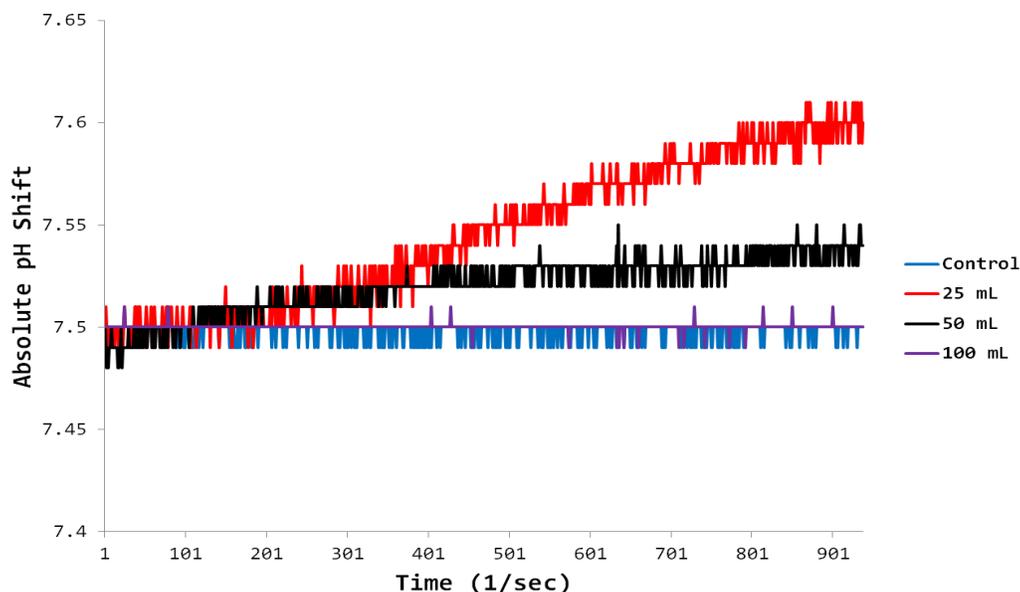
Figure 3. The absolute shift in pH within the 25 (red), 50 (black) and 100 (purple) cc volumes of spring water within the non-local flasks as a function of time from the onset of the entanglement phase. The blue line refers to control conditions (no shared field but acetic acid injected into the local flasks).

DISCUSSION

The results of this study indicate that strong excess correlation or entanglement between two separate spaces can occur when they are both exposed to circular (rotating) magnetic fields with appropriate changes in angular velocity. The effect was robust and consistent with the two separate spaces behaving as if they were the same locus. The acidification of the injected water (local flasks) was associated with the shift towards base in the "non-local" flasks. According to the traditional formula $[H^+]=10^{-pH}$, a shift of 0.01, 0.03, and 0.07 pH towards basic from a starting pH of 7.50 would be associated with a decrease of 1, 2, and $4 \cdot 10^{-9}$ M of H^+. When each of these concentrations is multiplied by the moles of water in each volume of 100, 50, and 25 cc, or 5.55 M, 2.78 M, and 1.39 M (1 mole of water=18 cc), the conserved molarity would be $5.55 \cdot 10^{-9}$ M. With $6.023 \cdot 10^{23}$ units per mole, there would be $3.35 \cdot 10^{15}$ H^+ involved with the phenomenon.

In comparison if we assume the functional median of the increased acidity in the local (injected) flasks was to about pH=5.6, the equivalent is $2.5 \cdot 10^{-6}$ M. The acetic acid was applied in 0.05 cc quantities to 25, 50, and 100 cc of water. The ratio of these volumes multiplied by the molarity of water in each volume is a constant of $2.77 \cdot 10^{-3}$ which results in a net concentration of $6.9 \cdot 10^{-9}$ M which is well within range of measurement error for the shift towards basic in the non local flasks.

If this is a physical process, the energy available from this special configuration of magnetic fields should converge with the shift in quantities of H^+ involved with the "superimposition" of the two spaces. From our perspective, the energy available from both magnetic fields (1 μT) is the product of the strength of the field ($kg \cdot A^{-1} \cdot s^{-2}$), unit charge ($A \cdot s$) and a measure of diffusivity ($m^2 \cdot s^{-1}$). Assuming $9 \cdot 10^{16}$ $m^2 \cdot s^{-1}$ (diffusion of light) and a unit charge ($1.6 \ 10^{-19}$ $A \cdot s$), the energy available for entanglement would be $\sim 1.4 \cdot 10^{-8}$ J and if applied over the time for the pH shift to occur (~ 1000 s), would be $14.4 \cdot 10^{-6}$ J for the cumulative energy. When divided by the number of H^+ involved with the shifts in pH ($3.35 \cdot 10^{15}$), the energy per proton is $4.3 \cdot 10^{-21}$ J per H^+. For comparison, the kT (where k is the Boltzmann constant and T is temperature in Kelvin) threshold that defines the thermal "noise" component for 25°C (298 K) is $\sim 4.1 \cdot 10^{-21}$ J. This is also within an order of magnitude of the $\sim 10^{-20}$ J quantum unit (Persinger, 2010) that may be involved as a universal quantity (Persinger et al., 2008).

REFERENCES

Ahn J, Weinacht TC, Bucksbaum PH (2000). Information storage and retrieval through quantum phase. Science 287:462-466.
Burke RC, Gauthier MY, Rouleau N, Persinger MA (2013). Experimental demonstration of potential entanglement of brain

activity over 300 km for pairs of subjects sharing the same circular rotating, angularly accelerating magnetic fields: verification by s_LORETA, QEEG measurements. J. Consc. Explor. Res. 4: 35-44.

Decoursey TE (2003). Voltage-gated proton channels and other proton transfer pathways. Physiol. Rev. 83:476-579.

Dotta BT, Buckner CA, Lafrenie RM, Persinger MA (2011). Photon emissions from human brain and cell culture exposed to distally rotating magnetic fields shared by separate light-stimulated brains and cells. Brain Res. 388:77-88.

Dotta BT, Persinger MA (2012). A "doubling" of local photon emissions when two simultaneous, spatially separated, chemiluminescent reactions share the same magnetic field configurations. J. Biophys. Chem. 3:72-80.

Fickler R, Lapkiewicz R, Plick WN, Krenn M, Schaeff C, Ramelow S, Zeilinger A (2012). Quantum entanglement of high angular momenta. Science. 338:640-644.

Hoffman J, Krug M, Ortegel N, Gerard L, Weber M, Rosenfield W, Weinfurter H (2012). Heralded entanglement between widely separated atoms. Science. 337:72-75.

Julsgaard B, Kozhekin A, Polzik ES (2001). Experimental long-lived entanglement of two macroscopic objects. Nature. 413: 400-403.

Persinger MA (2010). 10^{-20} Joules as a neuromolecular quantum in medicinal chemistry: an alternative approach to myriad molecular pathways. Cur. Med. Chem. 17:3094-3098.

Persinger MA, Koren SA, Lafreniere GF (2008). A neuroquantological approach to how human thought might affect the universe. Neuroquantol. 6:262-271.

Tu LC, Luo J, Gilles GT (2005). The mass of the photon. Rept. Prog. Phys. 68:77-130.

Full Length Research Paper

Magneto hydrodynamic (MHD) squeezing flow of a Casson fluid between parallel disks

Naveed Ahmed[1], Umar Khan[1], Sheikh Irfanullah Khan[1,2], Yang Xiao-Jun[3], Zulfiqar Ali Zaidi[1,2] and Syed Tauseef Mohyud-Din[1]

[1]Department of Mathematics, Faculty of Sciences, HITEC University, Taxila Cantt, Pakistan.
[2]COMSATS Institute of Information Technology, University Road, Abbottabad, Pakistan.
[3]College of Science, China University of Mining and Technology, Xuzhou, Jiangsu, 221008, China.

Squeezing flow of a Casson fluid is considered between two parallel disks. Upper disk is taken to be impermeable but capable of moving towards or away from the lower fixed and porous disk. Governing equations are derived with the help of conservation laws combined with suitable similarity transforms. Homotopy analysis method (HAM) is then been employed to determine the solution to resulting ordinary differential equation. Numerical solution is also obtained using R-K 4 method and comparison shows an excellent agreement between both solutions. Effects of different physical parameters on the flow are also discussed with the help of graphs along with comprehensive discussions.

Key words: Casson fluid, homotopy analysis method (HAM), squeezing flow, parallel disks, magneto hydrodynamic (MHD) flow, numerical solution.

INTRODUCTION

Squeezing flow between parallel disks has been an active field of research. Its biological and industrial applications have attracted many researchers towards its study. Numbers of efforts have been made to understand such types of flows in more depth. Motion of pistons is vital for running engines and machines. Squeezing flow under the influence of moving disk is also involved in nasogastric tubes and syringes. Better understanding of these flows leads us to more efficient and effective machines which may be used for both industrial and biological purposes.

After the foundational directions provided by Stefen (1874), many researchers investigated the squeezing flow problems (Reynolds, 1886; Archibald, 1956; Grimm, 1976; Wolfe, 1965; Kuzma, 1968; Tichy and Winer, 1970; Jackson, 1962; Hughes and Elco, 1962). As in most of

the cases fluids under consideration are non-Newtonian hence due to complex nature of these fluids different mathematical models are used to study their flow. For blood type fluids Mrill et al. (1965) and McDonald (1974) depicted a most compatible model known as Casson fluid.

Later Domairry and Aziz (2009) considered the flow of an electrically conducting fluid between two parallel disks of which lower disk is permeable and fluid can enter or exit through it during suction or injection process; upper disk is taken to be impermeable and it moves towards the lower disk with a certain time dependent velocity. They applied homotopy perturbation method (HPM) to approximate the solution. Due to inherent nonlinearities in Navier Stokes equations, exact solution in most of the cases is unlikely, therefore, different approximation
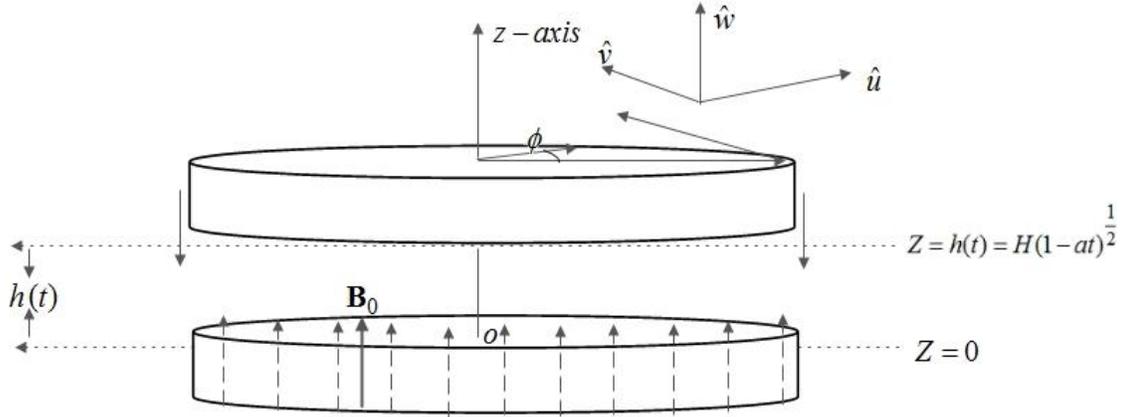
Figure 1. Schematic diagram of the problem.

techniques are used to approximate the solution analytically (Abbasbandy, 2007a, b; Abdou and Soliman, 2005a; Noor and Mohyud-Din, 2007; Abdou and Soliman, 2005b; Asadullah et al., 2013; Noor et al., 2008; Mohyud-Din et al., 2009; Nadeem et al., 2012). One of these analytical methods is homotopy analysis method (HAM) that has been effectively applied by different researchers to various nonlinear problems (Liao, 2003; Liao, 2004; Abbasbandy and Zakaria, 2008; Abbasbandy, 2007c; Tan and Abbasbandy, 2008; Hussain et al., 2012; Zeeshan et al., 2012; Hayat et al., 2003; Hayat et al., 2004; Khan et al., 2008; Hayat et al., 2009; Ellahi et al., 2010; Ellahi, 2013; Ellahi, 2012; Ellahi et al., 2012; Hayat et al., 2006).

In this paper, squeezed flow of magneto hydrodynamic (MHD) flow of a non-Newtonian Casson fluid is presented. The governing nonlinear partial differential equations are reduced to a much simpler nonlinear ordinary differential equation by employing a similarity transform. The reduced equation is solved by HAM and effects of emerging parameters are demonstrated graphically coupled with comprehensive discussions. A numerical solution is also carried out by using Runge-Kutta fourth order method to check the validity of analytical solution. An excellent agreement among the solutions is observed.

MATHEMATICAL ANALYSIS

Consider MHD incompressible flow of a Casson fluid between parallel infinite disks separated by a distance $h(t) = H(1-at)^{1/2}$. A magnetic field proportional to $B_0(1-at)^{1/2}$ is applied perpendicular to the disks. Based on the assumption of low Reynolds number, the induced magnetic field is neglected. The upper disk at $z = h(t)$ is moving with velocity $\dfrac{aH(1-at)^{-1/2}}{2}$ towards or away from the stationary lower disk at $z = 0$. The physical configuration is presented in Figure 1. Rheological equation of Casson fluid is defined as follows (Nadeem et al., 2012):

$$\tau_{ij} = \left[\mu_B + \left(\frac{p_y}{2\pi} \right)^{1/n} \right]^n 2e_{ij}, \tag{1}$$

μ_B is dynamic viscosity of the non-Newtonian fluid, p_y is yield stress of fluid and π is the product of component of deformation rate with itself, that is, $\pi = e_{ij}e_{ij}$, where e_{ij} is the $(i, j)th$ component of the deformation rate.

We have chosen the cylindrical coordinates system (r, ϕ, z). Due to the rotational symmetry of the flow $(\partial/\partial\phi = 0)$, the azimuthal component v of the velocity $V = (u, v, w)$ vanishes identically. Thus, the governing equation for unsteady two-dimensional flow and heat transfer of a Casson fluid are:

$$\frac{\partial \hat{u}}{\partial r} + \frac{\hat{u}}{r} + \frac{\partial \hat{w}}{\partial z} = 0 \tag{2}$$

$$\rho\left(\frac{\partial \hat{u}}{\partial t} + \hat{u}\frac{\partial \hat{u}}{\partial r} + \hat{w}\frac{\partial \hat{u}}{\partial z} \right) = -\frac{\partial \hat{p}}{\partial r} + \mu\left(1 + \frac{1}{\beta} \right)\left(2\frac{\partial^2 \hat{u}}{\partial r^2} + \frac{2}{r}\frac{\partial \hat{u}}{\partial r} + \frac{\partial^2 \hat{u}}{\partial z^2} + \frac{\partial^2 \hat{u}}{\partial r \partial z} - 2\frac{\hat{u}}{r^2} \right) - \frac{\sigma}{\rho}B^2(t)\hat{u} \tag{3}$$

$$\rho\left(\frac{\partial \hat{w}}{\partial t}+\hat{u}\frac{\partial \hat{w}}{\partial r}+\hat{w}\frac{\partial \hat{w}}{\partial z}\right)=-\frac{\partial \hat{p}}{\partial z}+\mu\left(1+\frac{1}{\beta}\right)\left(\frac{\partial^2 \hat{w}}{\partial r^2}+2\frac{\partial^2 \hat{w}}{\partial z^2}+\frac{1}{r}\frac{\partial \hat{w}}{\partial r}+\frac{1}{r}\frac{\partial \hat{u}}{\partial z}+\frac{\partial^2 \hat{u}}{\partial z^2}\right)$$ (4)

The boundary conditions are (Domairy and Aziz, 2009):

$$\hat{u}=0, \quad \hat{w}=\frac{dh}{dt} \quad \text{at } z=h(t)$$
$$\hat{u}=0, \quad \hat{w}=-w_0 \quad \text{at } z=0.$$ (5)

In the above equations, $\hat{u}$ and $\hat{w}$ are the velocity components in the r- and z - directions respectively, ρ is density, μ dynamic viscosity, $\hat{p}$ pressure, v kinematic viscosity and w_0 is the suction/injection velocity.
Substituting the following transformations (Domairy and Aziz, 2009):

$$\hat{u}=\frac{ar}{2(1-at)}f'(\eta), \quad \hat{w}=-\frac{aH}{\sqrt{1-at}}f'(\eta),$$
$$B(t)=\frac{B_0}{\sqrt{1-at}}, \quad \eta=\frac{z}{H\sqrt{1-at}}.$$ (6)

into Equations 2 and 3 and eliminating the pressure gradient from the resulting equations, we finally obtain

$$f_{n+1}(\eta)=A+\frac{1}{2}A_1\eta^2+\frac{1}{6}A_2\eta^3$$
$$-\left(\frac{\beta+1}{\beta}\right)\int_0^{\eta}\frac{(\eta-s)^3}{3!}\left(\begin{array}{c}-S(3f_n''(s)+sf_n'''(s)-2f_n(s)f_n'''(s))\\-M^2 f_n(s)f_n''(s)\end{array}\right)ds,$$ (7)

with the boundary conditions

$$f(0)=A, \quad f'(0)=0,$$
$$f(1)=\frac{1}{2}, \quad f'(1)=0.$$ (8)

Where S denotes the squeeze number, A the suction/blowing parameter and M is the Hartman number, defined as:

$$S=\frac{aH^2}{2v}, \quad M^2=\frac{aB_0^2 H^2}{v}.$$ (9)

SOLUTION PROCEDURE

Zero order deformation problem

Following the procedure proposed by Liao (2003), it is forthright to choose following initial guess:

$$f_0(\eta)=A+\frac{1}{2}(3-6A)\eta^2+(-1+2A)\eta^3.$$ (10)

Linear operator is selected as:

$$L_f=\frac{df^4}{d\eta^4}.$$ (11)

Above operator satisfies the following property:

$$L_f(C_1+C_2\eta+C_3\eta^2+C_4\eta^3)=0,$$ (12)

where $C_i (i=1-4)$ are the constants. Zero order deformation problem can now be constructed as follows (Noor et al., 2008):

$$(1-q)L_f[\tilde{f}(\eta,q)-f_0(\eta)]=qhN_f[\tilde{f}(\eta,q)],$$ (13)

$$\tilde{f}(0,q)=A, \quad \tilde{f}'(0,q)=0, \quad \tilde{f}(1,q)=\frac{1}{2}, \quad \tilde{f}'(1,q)=0,$$ (14)

where $q\in[0,1]$ is an embedding parameter and h is nonzero auxiliary parameter. Nonlinear operator is

$$N_f[\tilde{f}(\eta,q)]$$
$$=\frac{\partial^4 \tilde{f}(\eta,q)}{\partial\eta^4}-\left(\frac{\beta}{1+\beta}\right)\left\{S\left(\eta\frac{\partial^3 \tilde{f}(\eta,q)}{\partial\eta^3}+3\frac{\partial^2 \tilde{f}(\eta,q)}{\partial\eta^2}-2\tilde{f}(\eta,q)\frac{\partial^3 \tilde{f}(\eta,q)}{\partial\eta^3}\right)\right.$$
$$\left.-M^2\frac{\partial^2 \tilde{f}(\eta,q)}{\partial\eta^2}\right\}.$$ (15)

For $q=0$ and $q=0$ we have

$$\tilde{f}(\eta,0)=f_0(\eta), \quad \tilde{f}(\eta,1)=f(\eta).$$ (16)

$\tilde{f}(\eta, p)$ can be expressed as a Taylor's series in terms of q, that is,

$$\tilde{f}(\eta,q)=f_0(\eta)+\sum_{m=1}^{\infty}f_m(\eta)q^m, \quad f_m(\eta)=\frac{1}{m!}\frac{\partial^m f(\eta,q)}{\partial\eta^m}\bigg|_{p=0}.$$ (17)

Substituting $q=1$ in above equation we obtain

$$\tilde{f}(\eta,1)=f_0(\eta)+\sum_{m=1}^{\infty}f_m(\eta).$$ (18)

m^{th}-order deformation problem

m times differentiation of zero order problem depicted by Equation 13 and setting $q=0$ leads to

$$L_f[\tilde{f}_m(\eta)-\chi_m f_{m-1}]=h\Re_m^f(\eta),$$ (19)
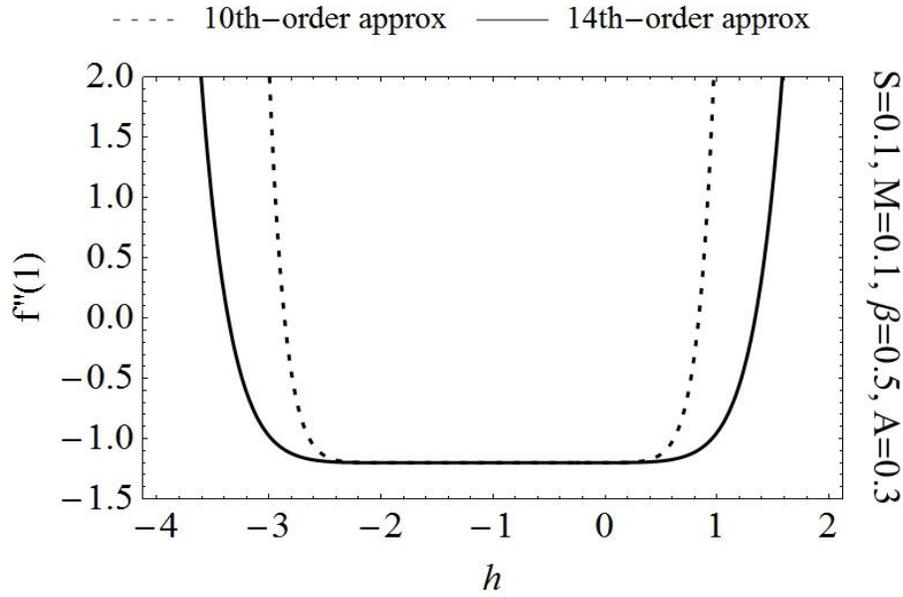
Figure 2. *h* curves for the function *f* for different orders of approximations.

Where

$$\Re_m^f(\eta) = f_{m-1}''' - \left(\frac{\beta}{1+\beta}\right)\left\{S\left(\eta f_{m-1}'' + 3 f_{m-1}''\right) - M^2 f_{m-1}'' + 2S\sum_{k=0}^{m-1} f_{m-1-k} f_k''\right\},$$

(20)

$$\chi_m = \begin{cases} 0, & m \leq 1 \\ 1, & m > 1 \end{cases}$$

(21)

The general solution of Equation 19 is

$$f_m(\eta) = f_m^\circ(\eta) + C_1^m + C_2^m \eta + C_3^m \eta^2 + C_4^m \eta^3,$$

(22)

where $f_m^\circ(\eta)$ represents the special solution; also

$$C_1^m = -f_m^\circ(0), \quad C_2^m = -\frac{\partial f_m^\circ(\eta)}{\partial \eta}\bigg|_{\eta=0}$$

$$C_3^m = -3C_1 - 2C_2 - 3f_m^\circ(1) + \frac{\partial f_m^\circ(\eta)}{\partial \eta}\bigg|_{\eta=1}$$

(23)

$$C_4^m = 2C_1 + C_2 + 2f_m^\circ(1) - \frac{\partial f_m^\circ(\eta)}{\partial \eta}\bigg|_{\eta=1}$$

Above higher order solution can be substituted to Equation 18 to obtain the final solution.

Convergence of the solution

Obtained series solution given by Equation 18 contains an auxiliary parameter h. As pointed out by Liao (2003), this parameter is the key to control convergence of series solution. Acceptable range of h can be determined by identifying the line segment of so called h-curves which is parallel to h axis. In our particular problem this can be achieved by seeing the range in which $f''(1)$ bears the same magnitude for any value of h within that range. Figure 2 is displayed to demonstrate convergence region for two orders of approximations namely 10th and 14th. It clearly shows that the acceptable region of h is to be between -2.4 and 0.4.

RESULTS AND DISCUSSION

Acceptable range for auxiliary parameter h has been discussed in previous section. In our analysis and discussions we use $h = -0.9$ as an optimal value of h. After ensuring the convergence of series solution our concern now is to see the influences of suction/blowing parameter *A*, squeeze number *S*, Hartmann number *M* and Casson fluid parameter β on velocity is examined. For convenience, we divide our discussions into two parts; one dedicated to investigate the upshots on varying physical parameter for the case suction ($A > 0$) and the other one describes the same effects for the case of blowing ($A < 0$).

Suction case

Effects of increasing suction at lower disk on both axial and radial velocities are displayed in Figures 3 and 4
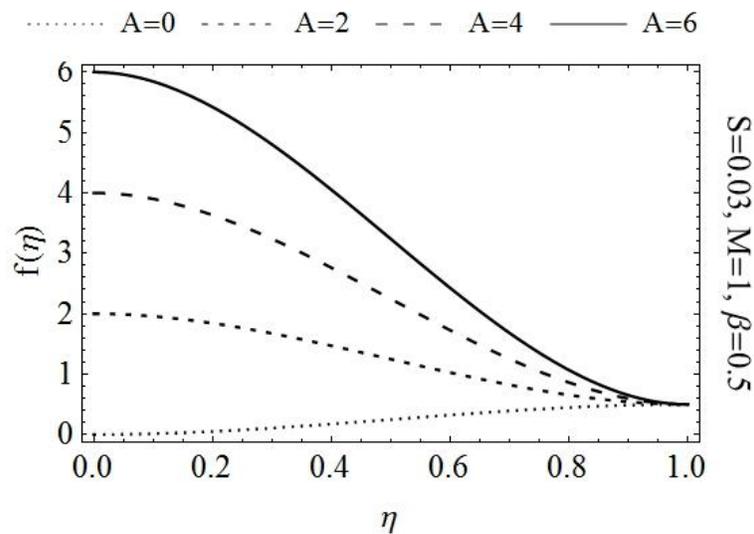
Figure 3. Effects of *A* on axial velocity.
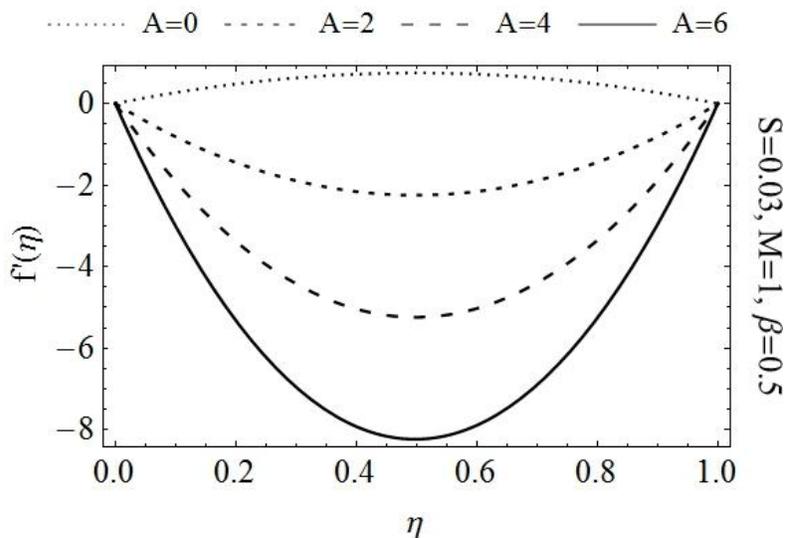
Figure 4. Effect of *A* on radial velocity.

respectively. It is evident that increasing value of A results in higher absolute values of both the velocities. As increasing suction allows more fluid to flow near the lower disk therefore a decrease in boundary layer thickness is expected.

Influences of squeeze parameter *S* on axial and radial velocities are displayed in Figures 4 and 5 respectively. Here *S*<0 corresponds to the movement of upper disk towards lower one. On the other hand, *S*>0 describes away movement of the same disk. It can be seen from Figure 5 that for squeezing motion of upper disk combined with suction axial velocity near the center is increased while for dilating motion a decrease in axial velocity is observed. From Figure 6 one can see the behavior of radial velocity for same variations in *S*. It is evident for expanding motion; an accelerated radial flow is observed near the upper disk however this trend changes gradually as we move away from it. Somewhere near the center this trend gets converted into an opposite one; that is, from that point to lower disk a delayed motion is observed. For contracting motion of upper disk combined with suction at lower disk effects of increasing
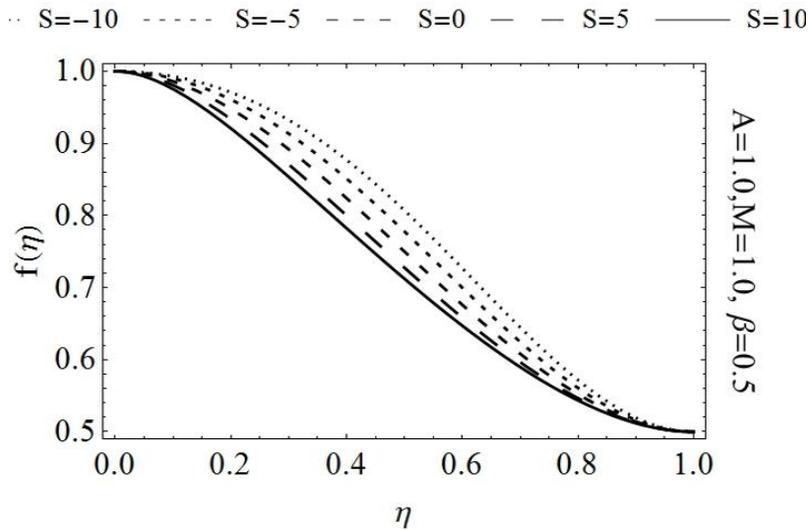
Figure 5. Effects of *S* on axial velocity.
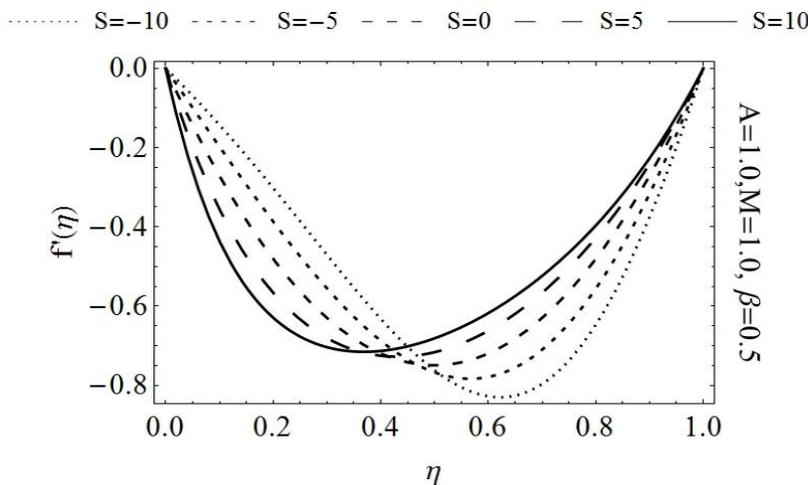
Figure 6. Effect of *S* on radial velocity.

absolute values of *S* are quite opposite to the case of expanding motion. In this case, radial velocity near upper disk decreases while near the lower disk an accelerated radial flow is observed.

Graphical results describing flow behavior under increasing Hartmann number *M* are displayed in Figures 7 and 8. From Figure 7, it can be seen that the axial velocity $f(\eta)$ is a decreasing function of M. As apparent from Figure 8, absolute value of radial velocity $f'(\eta)$ increases near the disks while in center, it behaves oppositely. It is also worth mentioning that effect near upper disk is more prominent as compared to lower one. Figures 9 and 10 respectively are dedicated to display

behavior of axial and radial velocity for increasing Casson parameter β. Axial velocity is a decreasing function of β as shown in Figure 9. Effects of β on axial velocity are more visible in central region as compared to the area near disks. Furthermore, $\beta->\infty$ gives us the flow of viscous fluid. Figure 10 shows that the radial velocity near lower disk decreases with rising β. However, after moving some distance away from the lower disk this behavior changes into an opposite one; that is, after $\eta > 0.4$ we observe an accelerated radial flow. One may also see that effects of β near the disks are very slight as compared to the region far from them.
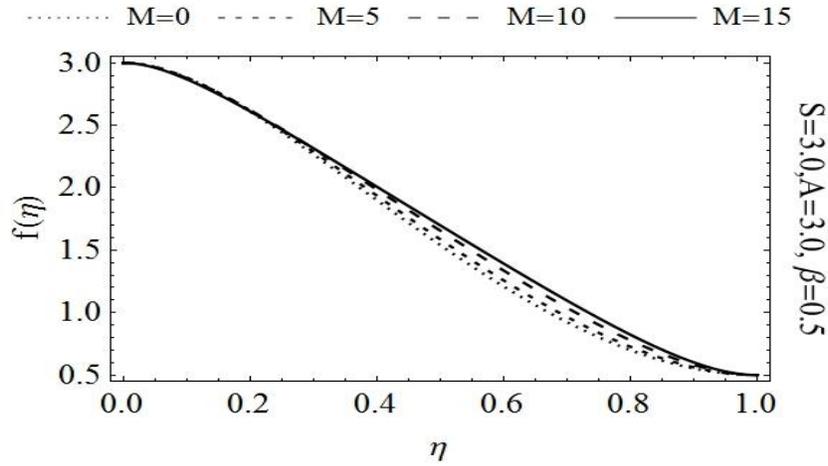
Figure 7. Effects of *M* on axial velocity.
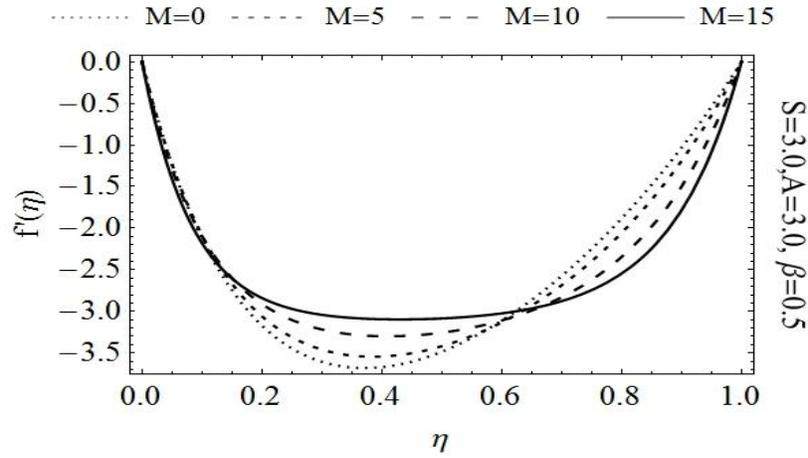
Figure 8. Effect of *M* on radial velocity.
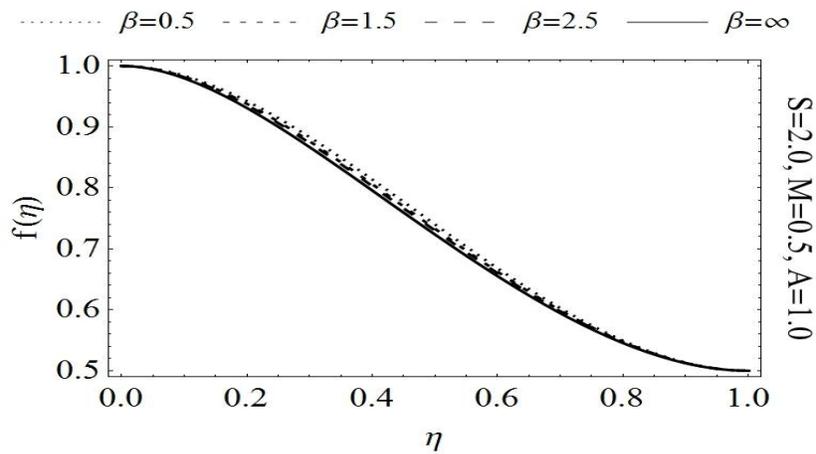
Figure 9. Effects of β on axial velocity.
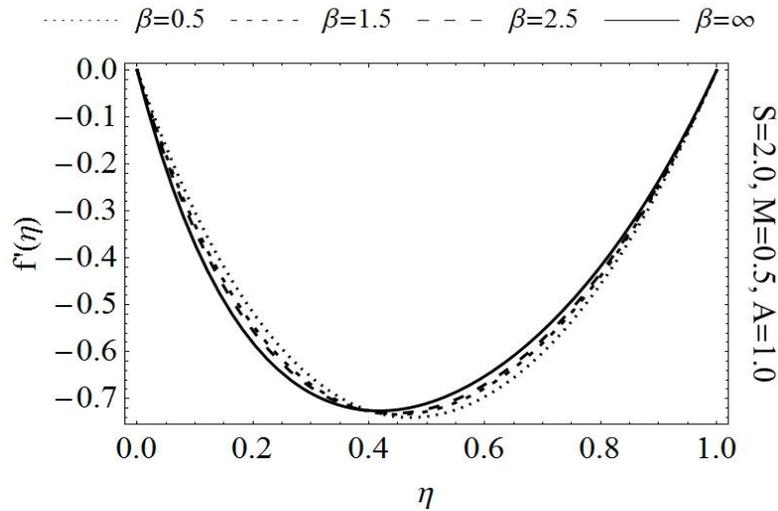
Figure 10. Effect of β on radial velocity.
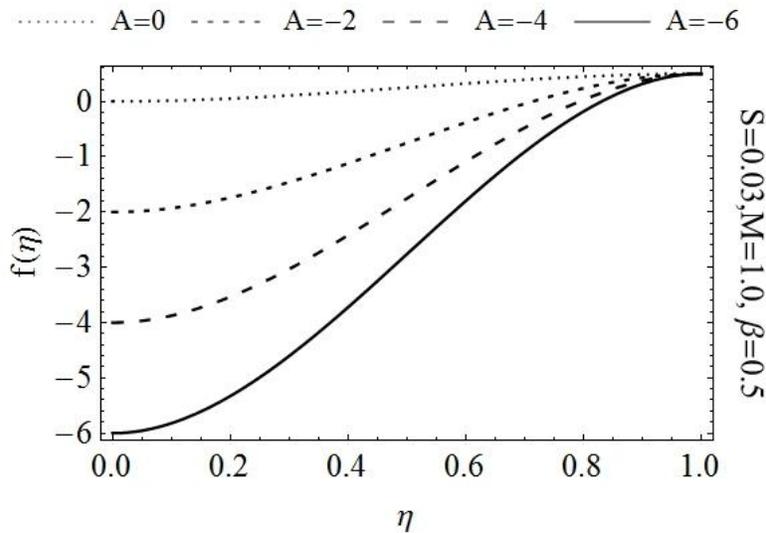
Figure 11. Effects of *A* on axial velocity.

Blowing case

Here we discus influences of involved physical parameter in the case when blowing occur at the lower disk. Figures 11 and 12 declare that the influence on increasing injection leads to increased absolute values of both axial and redial velocities. Figures 13-18 show that the effects of *S*, *M* and β on both axial and radial flow are opposite in blowing case as compared to the ones obtained for suction case. Same problem is solved numerically by using a well-known RK-4 method. Comparison for is presented in Table 1. It can be observed that both

numerical and analytical solutions are in excellent agreement.

Conclusion

Squeezing flow between parallel disks is presented. Homotopy analysis method (HAM) has been employed to obtain analytical solution to the problem. Influences of emerging flow parameters are discussed in detail with the help of graphs. It is also concluded that the effects of physical parameter on axial and redial velocities are quite

A=0 ⋯⋯   A=−2 ----   A=−4 - - -   A=−6 ——
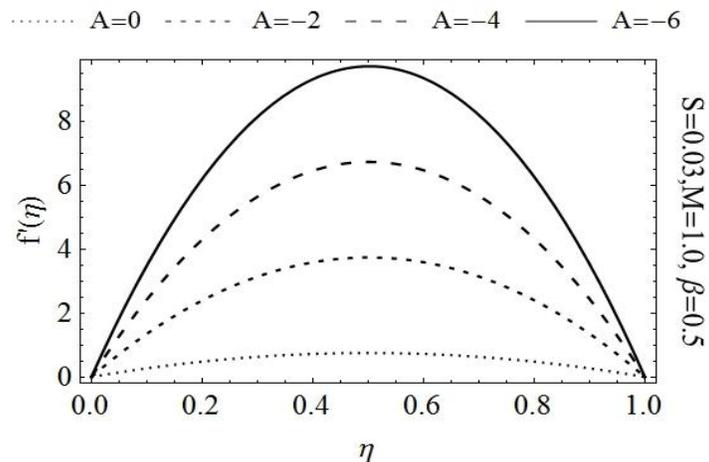
Figure 12. Effect of *A* on radial velocity.

S=−10 ⋯⋯   S=−5 -----   S=0 - - -   S=5 — —   S=10 ——
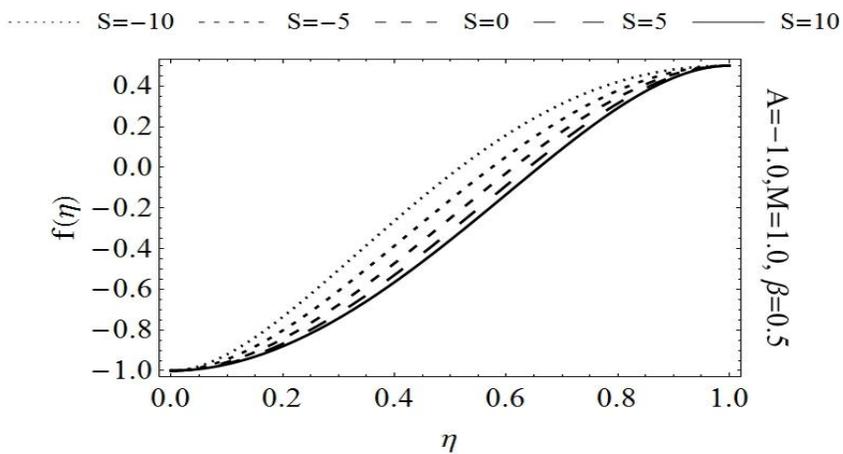
Figure 13. Effects of *S* on axial velocity.

S=−10 ⋯⋯   S=−5 -----   S=0 - - -   S=5 — —   S=10 ——
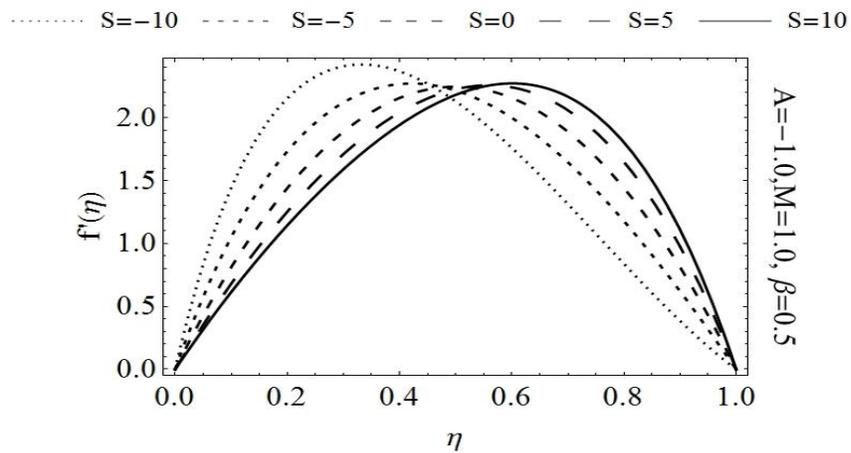
Figure 14. Effect of *S* on radial velocity.

M=0.0 ⋯⋯⋯ M=3.0 ----- M=6.0 – – – M=9.0 ──────

f(η)

S=1.0, β=0.5, A=−1.0

η
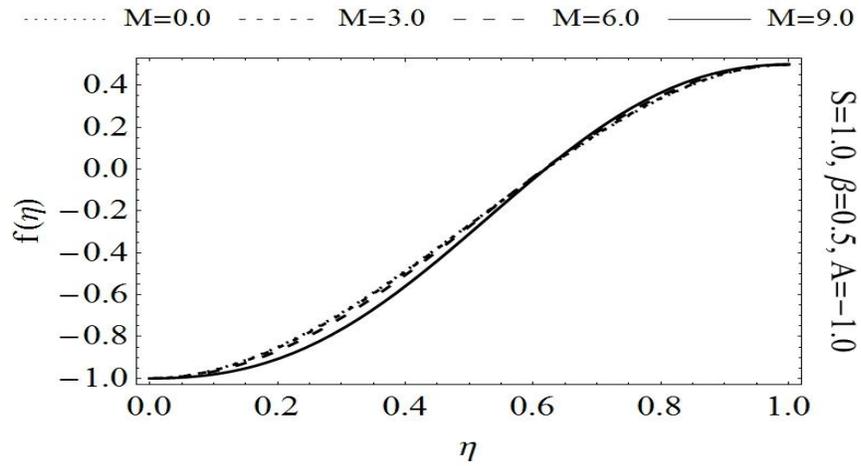
Figure 15. Effects of *M* on axial velocity.

M=0.0 ⋯⋯⋯ M=3.0 ----- M=6.0 – – – M=9.0 ──────

f'(η)

S=1.0, β=0.5, A=−1.0

η
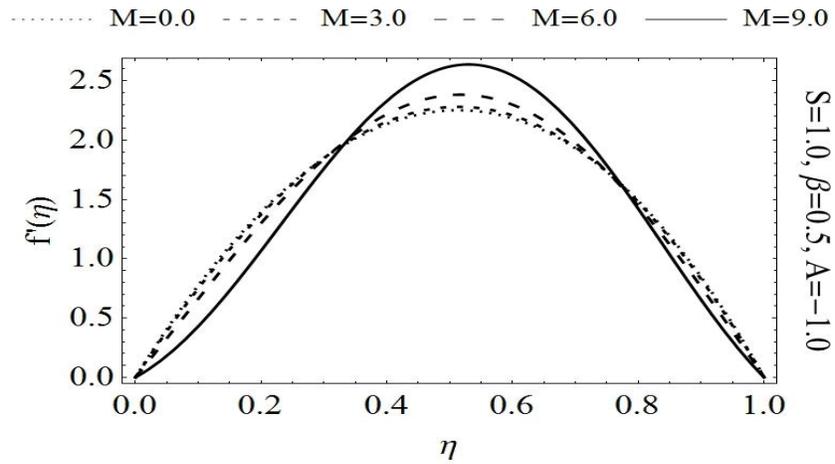
Figure 16. Effect of *M* on radial velocity.

β=0.1 ⋯⋯⋯ β=1.0 ----- β=3.0 – – – β=∞ ──────

f(η)

S=2.0, M=0.5, A=−1.0

η
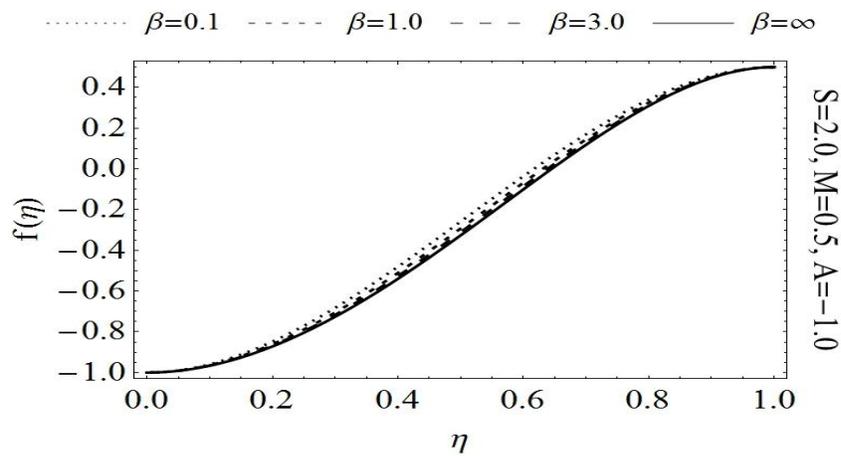
Figure 17. Effects of β on axial velocity.

$\beta=0.1$ .... $\beta=1.0$ - - - - - $\beta=3.0$ – – – $\beta=\infty$ ———

S=2.0, M=0.5, A=−1.0
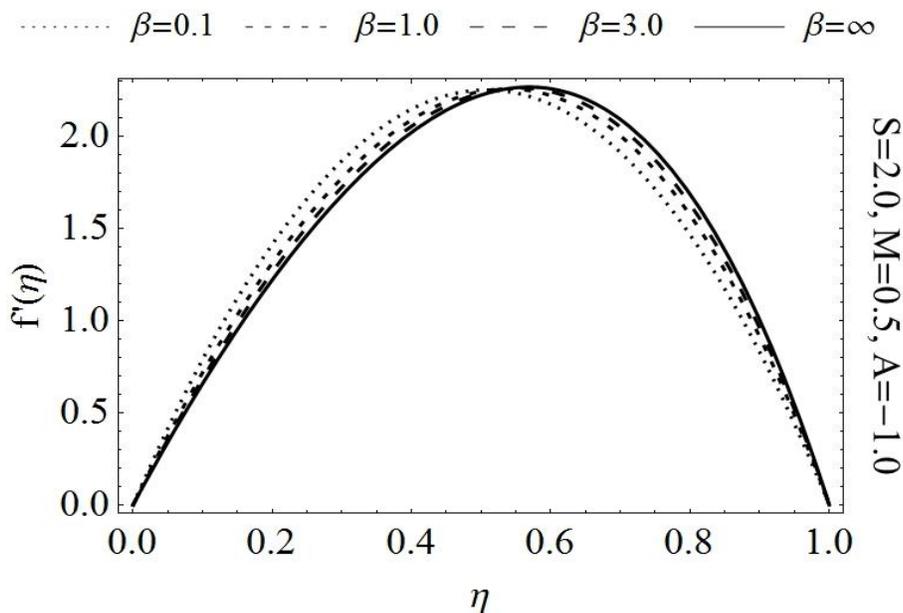
Figure 18. Effect of β on radial velocity.

Table 1. Comparison of HAM and numerical solutions for $S = 2.0, A = 1.0, M = 0.5, h = -0.9, \beta = 0.5.$

η	$f(\eta)$ HAM	Numerical	$f'(\eta)$ HAM	Numerical
0	1.000000	1.000000	0	0
0.1	0.984012	0.984012	-0.303368	-0.303368
0.2	0.942321	0.942321	-0.516753	-0.516753
0.3	0.883192	0.883192	-0.654099	-0.654099
0.4	0.813695	0.813695	-0.725515	-0.725515
0.5	0.740051	0.740051	-0.737995	-0.737995
0.6	0.667911	0.667911	-0.695962	-0.695962
0.7	0.602598	0.602598	-0.601667	-0.601667
0.8	0.549306	0.549306	-0.455454	-0.455454
0.9	0.513283	0.513283	-0.255919	-0.255919
1.0	0.500000	0.500000	0	0

opposite in the cases of suction to the blowing. A numerical solution using well known R-K 4 method has also been obtained for the sake of comparison. It is found that the results agree exceptionally well.

REFERENCES

Abbasbandy S (2007a). The application of homotopy analysis method to solve a generalized Hirota-Satsuma coupled KdV equation, Phys. Lett. A. 361:478–483.

Abbasbandy S (2007b). A new application of He's variational iteration method for quadratic Riccati differential equation by using Adomian's polynomials, J. Computational Appl. Math. 207:59-63.

Abbasbandy S (2007c). Numerical solutions of nonlinear Klein-Gordon equation by variational iteration method, Int. J. Num. Methods Eng. 70:876-881.

Abbasbandy S, Zakaria FS (2008). Soliton solutions for the fifth-order K-dVEquation with the homotopy analysis method, Nonlinear Dynamics, 51:83–87.

Abdou MA, Soliman AA (2005a). New applications of variational iteration method, Physica D. 211(1-2):1-8.

Abdou MA, Soliman AA (2005b). Variational iteration method for solving Burger's and coupled Burger's equations. J.Computational Appl. Math. 181:245-251.

Archibald FR (1956). Load capacity and time relations for squeeze films. J. Lubrication Technol. 78:A231–A245.

Asadullah M, Khan U, Ahmed N, Manzoor R, Mohyud-Din ST (2013). Int. J. Modern Math. Sci. 6:92-106.

Domairy G, Aziz A (2009), Approximate Analysis of MHD Squeeze Flow

between Two Parallel Disks with Suction or Injection by Homotopy Perturbation Method, Mathematical Problems in Engineering, article ID/2009/603916.

Ellahi R (2012). A Study on the Convergence of Series Solution of Non-Newtonian Third Grade Fluid with Variable Viscosity: By Means of Homotopy Analysis Method, Adv. Math. Phys. Article ID 634925, 11 pages.

Ellahi R (2013). The effects of MHD and temperature dependent viscosity on the flow of non-Newtonian nanofluid in a pipe: Analytical solutions, Appl. Math. Modeling, 37:1451-1467.

Ellahi R, Hayat T, Mahomed FM, Zeeshan A (2010). analytical solutions for MHD flow in an annulus, Commun. Nonlin. Sci. Numer. Simul. 15:1224-1227.

Ellahi R, Raza M, Vafai K (2012).Series solutions of non-Newtonian nanofluids with Reynolds' model and Vogel's model by means of the homotopy analysis method, Mathe. Computer Modelling, 55:1876–1891.

Grimm RJ (1976). Squeezing flows of Newtonian liquid films: an analysis includes the fluid inertia. Appl. Sci. Res. 32(2):149–166,

Hayat T, Ellahi R, Ariel PD, Asghar S (2006). Homotopy Solution for the Channel Flow of a Third Grade Fluid, Nonlinear Dynamics, 45:55–64.

Hayat T, Ellahi R, Asghar S (2004). Unsteady periodic flows lows of a magnetohydrodynamic fluid due to noncoxial rotations of a porous disk and a fluid at infinity, Math. Computer Modelling, 40:173-179.

Hayat T, Ellahi R, Mahomed FM (2009). The Analytical Solutions for Magnetohydrodynamic Flow of a Third Order Fluid in a Porous Medium, Zeitschriff Naturforsch, 64a:531-539.

Hayat T, Mumtaz S, Ellahi R (2003). MHD unsteady periodic flows due to non-coaxial rotations of a disk and a fluid at infinity, Acta Mathematica Sinica, 19:235-240.

Hughes WF, Elco RA (1962). Magnetohydrodynamic lubrication flow between parallel rotating disks. J. Fluid Mechanics, 13:21–32.

Hussain A, Mohyud-Din ST, Cheema TA (2012). Analytical and Numerical Approaches to Squeezing Flow and Heat Transfer between Two Parallel Disks with Velocity Slip and Temperature Jump, Chinese Phys. Lett. 29:114705.

Jackson JD (1962). A study of squeezing flow, Appl. Sci. Res. A. 11:148–152.

Khan I, Ellahi R, Fetecau C (2008). Some MHD Flows of a Second Grade Fluid through the Porous Medium. J. Porous Media, 11:389-400.

Kuzma DC (1968). Fluid inertia effects in squeeze films. Appl. Sci. Res. 18:15–20.

Liao SJ (2003). Beyond perturbation: introduction to the Homotopy Analysis Method, CRC Press, Boca Raton, Chapman and Hall, 2003.

Liao SJ (2004). On the homotopy analysis method for nonlinear problems, Appl. Math. Computation, 147:499–513.

McDonald DA (1974). Blood Flows in Arteries, 2nd ed. Arnold, London

Mohyud-Din ST, Noor MA, Waheed A (2009). Variation of parameter method for solving sixth-order boundary value problems, Communication Korean Math. Soc. 24:605-615.

Mrill EW, Benis AM, Gilliland ER, Sherwood TK, Salzman EW (1965). Pressure flow relations of human blood hollow fibers at low flow rates. J. Appl. Physiol. 20:954–967.

Nadeem S, Haq UIR, Lee C (2012). MHD flow of a Casson fluid over an exponentially shrinking sheet, Scientia Iranica, 19:1150-1553.

Noor MA, Mohyud-Din ST (2007). Variational iteration technique for solving higher order boundary value problems, Appl. Math. Computation, 189:1929-1942.

Noor MA, Mohyud-Din ST, Waheed A (2008). Variation of parameters method for solving fifth-order boundary value problems. Appl. Math. Infor. Sci. 2:135 -141.

Reynolds O (1886). On the theory of lubrication and its application to Mr. Beauchamp Tower's experiments, including an experimental determination of the viscosity of olive oil, Philosophical Transactions of the Royal Society of London, 177:157–234.

Stefen MJ (1874). Versuch¨ Uber die scheinbare adhesion, Sitzungsberichte der Akademie der Wissenschaften in Wien. Mathematik-Naturwissen, 69:713–721.

Tan Y, Abbasbandy S (2008). Homotopy analysis method for quadratic Riccati differential Equation, Communications Nonlinear Sci. Num. Simulation, 13:539–546.

Tichy JA, Winer WO (1970). Inertial considerations in parallel circular squeeze film bearings, J. Lubrication Technol. 92:588–592.

Wolfe WA (1965). Squeeze film pressures. Appl. Sci. Res. 14:77–90.

Zeeshan A, Ellahi R, Siddiqui AM, Rahman HU (2012). An investigation of porosity and magnetohydrodynamic flow of non-Newtonian nanofluid in coaxial cylinders, Int. J. Phys. Sci. 7(9):1353–1361.

International Journal of Physical Sciences

Full Length Research Paper

Determination of the vertical variations in temperature and longwave radiation within the gray Earth's troposphere using radiative equilibrium profile model

Mudasiru A. Olajire[1]* and Olaniran J. Matthew[2]

[1]Department of Physics, Osun State College of Education, Ila-Orangun, Osun State, Nigeria.
[2]Institute of Ecology and Environmental Studies, Obafemi Awolowo University, Ile-Ife, Nigeria.

This study estimated the vertical variation in mean temperatures within the tropospheric layer using the radiative equilibrium profile model and longwave radiation with Stefan-Boltzmann equation at a tropical meteorological station located besides Physics Building (7.55°N:4.56°E), Obafemi Awolowo University, Ile-Ife, Nigeria. In the model, the height of the troposphere was assumed to be 16.0×10^0 km and the standard effective mean temperature (255K) in the tropics was used in estimating the tropospheric mean temperatures for two layers: the ground surface (1.6×10^{-3} km) and the top of the troposphere (16.0×10^0 km). Arithmetic progression expression was then used to obtain the temperatures and longwave radiations for 16 equal sub-layers within the vertical height of the Earth's troposphere. Our results showed that the estimated ground layer temperature (33.3°C) and longwave radiation (499.1 Wm^{-2}) for the meteorological station were comparable with the observed (31.9°C; 490.0 Wm^{-2}). Both the temperature and radiation were found to decrease with altitude within the tropospheric layers. The study concluded that the model performed reasonably in estimating the vertical profile of temperatures and longwave radiation over the study area.

Key words: Radiative equilibrium profile, temperature, longwave radiation, troposphere.

INTRODUCTION

The Earth's atmosphere is defined as an envelope of gases mixed up in remarkable proportion with varying percentage compositions (Olajire, 2008). For example, the percentage composition of Nitrogen (N_2) by volume is approximately 78.08%; Oxygen (O_2), 20.95%; Argon (Ar), 0.93%; Carbon dioxide(O_2), 0.03%; Neon (Ne), 0.002%; Helium (He), 0.005%; Methane (CH_4), 0.0002%; Krypton (Kr), 0.00001% and Hydrogen (H_2), 0.00005% while N_2O, Xe, CO, O_3 in traces of water vapor are 0.0001% (Roger and Richards, 1995).

Literature illustrated that the atmosphere can be divided into four layers or regions using the characteristic temperature lapse rates (that is, troposphere, stratosphere, mesosphere and thermosphere). The first layer, troposphere, is a friction layer where many atmospheric activities take place. This layer was found to vary in height and extends to a height of approximately 8 km in the polar region and 16 -19 km over the tropical regions (Cole, 1980). Figure 1 illustrates the vertical variations in temperature within the different layers of the atmosphere as reported by Scisat-1 (2010). The figure showed that, within the troposphere, the temperature decreases from about 18°C on the earth's surface to about -47°C at the top (12 km) of the troposphere. The tropical region is principally characterized by more or less uniform decrease in temperature with height within this

*Corresponding author. E-mail: olajiremudasiru@yahoo.com
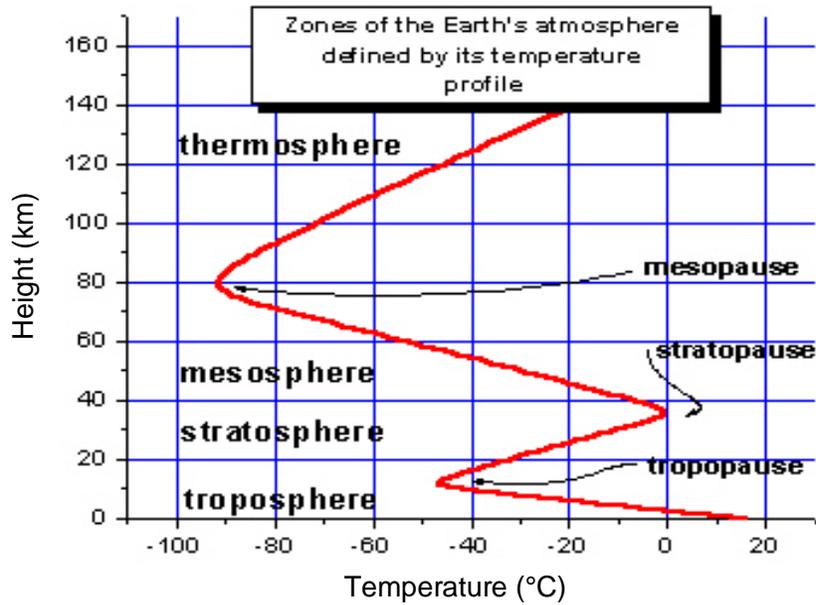
Figure 1. Variation in temperature with altitude (After Scisat-1, 2010).
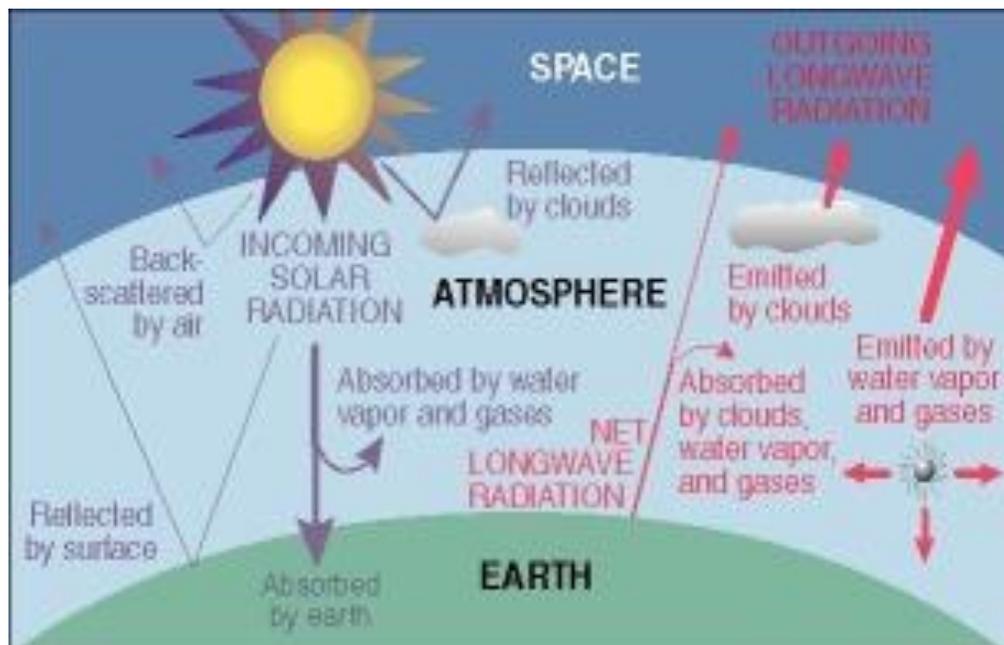
Figure 2. Radiation balance at the Earth's surface (Source: Ritter, 2009).

layer. Just above the troposphere, the temperature remains constant for further 1 or 2 km (called the tropopause) before it increase again from about -47°C (at a height 14 km; top of the tropopause) to about 0°C (at a height 35 km; top of the stratosphere). Within the stratosphere (36-80 km), the temperature decreases to about -92°C. The vertical temperatures increase within the thermosphere to reach about -20°C at the top of this layer (140 km).

About fifty-one percent (51%) of the solar or short wave radiation (0.2- 4.0 µm) at the top of the atmosphere were found to reach the earth's surface (Ritter, 2009). This is so because of the atmospheric radiation absorption, reflection and scattering (Figure 2). The atmospheric
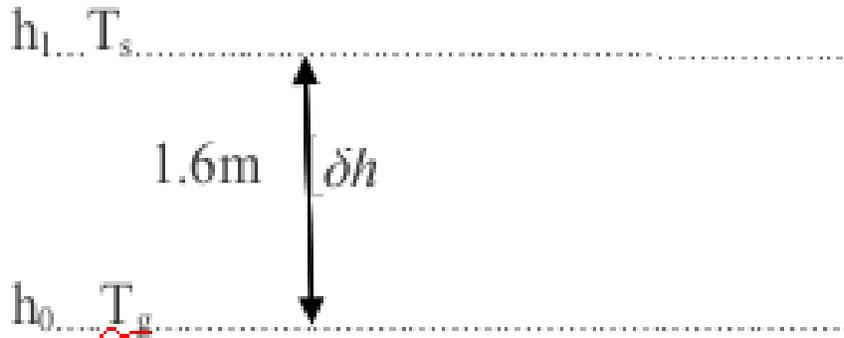
Figure 3. Stephenson screen height above the ground surface at Meteorological station located besides Physics Building, Obafemi Awolowo University Campus, Ile-Ife, Nigeria.

constituents such as oxygen (O_2), water vapour (H_2O) and carbon dioxide (CO_2) re-emit the absorbed shortwave radiation back to the earth's surface within the longwave band (12.0 - 150.0 μm). Similarly, at the Earth's surface, solar radiation is partially reflected, absorbed and then re-radiated back to the space as terrestrial or longwave radiation. The atmosphere is much more absorbent to longwave radiation than to short wave radiation. Most absorption of the longwave radiation by water vapour takes place in the lowest layer of the atmosphere thereby making the clouds very effective absorbers (Ritter, 2009). Under clear skies, radiation is emitted by the surface but little is received by the atmospheric constituents in the atmosphere and therefore the temperature falls rapidly, (Olajire, 2012). Longwave radiation varies directly as the fourth power of the surface's absolute temperatures. Its value thus depends largely on the land-cover, atmospheric constituents (such as gases in the atmosphere and aerosols) and clouds cover, types and drift (Briggs and Smithson, 1995).

Various observations had shown that temperature varies with altitude and that temperature lapse rate is one of the controlling factors governing the structure of any planetary atmosphere (Roger and Richard, 1995). However, studies on the vertical temperature structure of the tropospheric layer in many tropical locations of the world, including those areas where there are wide gaps in observational data, are grossly inadequate. More so that the use of common atmospheric measuring instruments like radio sonde, rocket, etc (Roger and Richard, 1995) in these locations is still rare. Thus, the primary objective of this study was to estimate the tropospheric layer temperature over Obafemi Awolowo University (OAU) Campus, Ile-Ife, Nigeria using the principle of radiative equilibrium profile model and longwave radiation using the Stefan-Boltzman equation. The paper evaluated the performance of the radiative equilibrium profile model in estimating the vertical variation in mean temperatures and Stefan-Boltzmann equation in estimating longwave

radiation within the troposphere. The results enhanced our scientific understanding of the vertical profile of the troposphere.

MATERIALS AND METHODS

A Stephenson screen of about 1.6×10^{-3} km (Figure 3) above the ground surface containing a dry bulb thermometer was sited at the meteorological station located besides Physics Building, Obafemi Awolowo University, Ile-Ife (7.55°N: 4.56°E), Nigeria (Figure 4) for continuous measurements of micrometeorological parameters (such as temperature, rainfall, wind speed, relative humidity, solar radiation and surface heat fluxes) at 10 min time interval.

The radiative equilibrium profile model is a multi-layer model. Within each layer, both the temperature and longwave radiation were assumed to be uniform but vary across the layers. In this study, however, a 2-layer radiative equilibrium profile model was assumed. An arithmetical progression expression was then used to further sub-divide the two layers into 16 equal sub-layers. In the model, the standard effective mean temperature ($T_e = 255K$) in the tropics was used to obtain the mean temperatures at different layers within the tropospheric height which was assumed to be 16.0×10^0 km at the study area (Cole, 1980).

Radiative Equilibrium Profile Model's descriptions

Radiative Equilibrium Profile Model, fully described by Henderson-Sellers and McGuffey (2007) is a multi-layer model (Figure 5). The model assumes that the solar radiation goes straight to the surface (not absorbed by any layer) and that the longwave radiation given out by each layer will go to next adjacent layer (that is, no one crosses next adjacent layer). This agreed with the submission of Swinbank (1963) in that most of the atmospheric longwave radiation reaching the earth's surface originates from within a few hundred meters from the ground. The model also assumed that the layers are neither too thick nor too thin and that the longwave radiation is emitted to the last surface from the ground. The surface temperature T_g (K) is presumed to be approximately equal to the air temperature T_a (K) measured by the dry bulb thermometer in the Stephenson screen. With this, the earth surface behaves like a perfect black body where the energy absorbed is approximately equal to the energy emitted and emissivity, ε, is approximately unity (ε = 1).

Long wave radiation, L_w was determined using the Stefan-
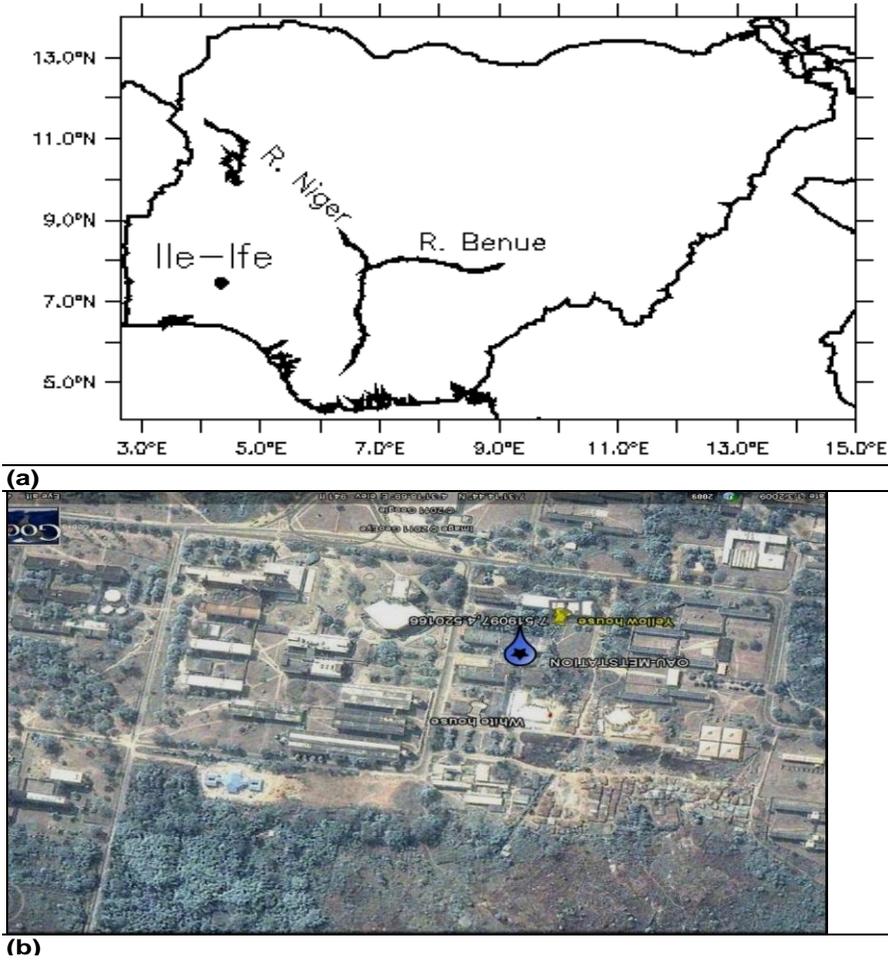
Figure 4. A Map of Nigeria showing (a) the location of Obafemi Awolowo University (OAU) Campus, Ile-Ife, Southwest Nigeria and (b) the position of the meteorological station beside Physics Building at OAU, Ile-Ife.

Boltzmann equation:

$$L_W = \varepsilon\sigma T^4 \tag{1}$$

Where ε is the emissivity of atmospheric parameters (dust samples, gases, water vapour and clouds), σ is Stefan-Boltzmann constant and T the absolute temperature. In this study, the atmospheric parameters such as water vapour and clouds were considered as grey body with emissivity, ε approximately equal to 1. Thus Equation 1 becomes:

$$L_W = \sigma T^4 \tag{2}$$

Hence, the radiation leaving the top of the atmosphere is equal to incoming radiation. That is,

$$\sigma T_e^4 \downarrow = \sigma T_1^4 \uparrow \tag{3}$$

$$T_1^4 = T_e^4 \tag{4}$$

Layer 1 has temperature T_1 and radiates out at the rate σT_1^4 to layer 4 below and to the outer space. Therefore,

$$\sigma T_1^4 \downarrow + \sigma T_1^4 \uparrow = \sigma T_2^4 \uparrow$$
$$2\sigma T_1^4 = \sigma T_2^4 \uparrow \tag{5}$$

From Equations 4 and 5 we have,

$$T_2^4 = 2T_e^4 \tag{6}$$

For layer 2,

$$\sigma T_2^4 \downarrow + \sigma T_2^4 \uparrow = \sigma T_1^4 \downarrow + \sigma T_3^4 \uparrow$$
$$2\sigma T_2^4 = \sigma T_1^4 \downarrow + \sigma T_3^4 \uparrow \tag{7}$$

For layer 3,

$$\sigma T_3^4 \downarrow + \sigma T_3^4 \uparrow = \sigma T_2^4 \downarrow + \sigma T_4^4 \uparrow$$
$$2\sigma T_3^4 = \sigma T_2^4 \downarrow + \sigma T_4^4 \uparrow \tag{8}$$
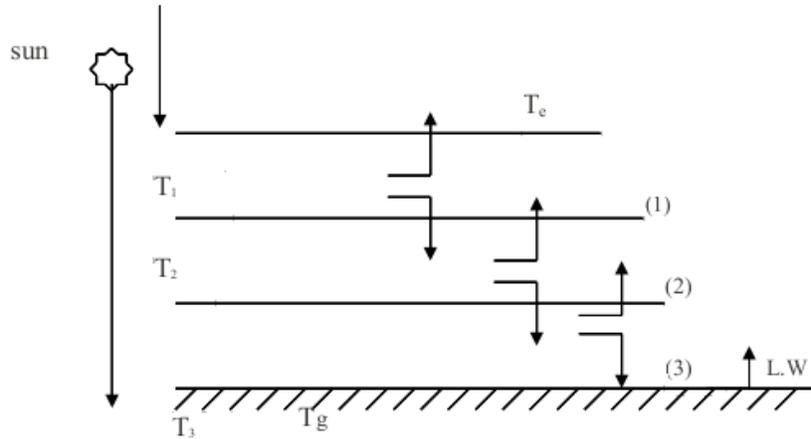
Figure 5. Radiative Equilibrium Profile Model used in this study (after Henderson-Sellers and McGuffey, 2007).

Table 1. Observed and estimated vertical mean temperatures and longwave radiations over Obafemi Awolowo University Campus, Ile-Ife, Southwestern Nigeria.

:

Altitude (km)	Temperatures (^{o}C)			Longwave radiation (Wm^{-2})		
	Observed	Estimated	Bias	Observed	Estimated	Bias
1.6 x10^{-3}	31.9	33.3	1.4	490.0	499.1	9.1
16.0 x10^{0}	-	-18.0		-	239.8	

Using Equations 3 and 5 in Equation 7, we obtain

$$T_3^4 = 3T_e^4 \qquad (9a)$$

Similarly,

$$T_4^4 = 4T_e^4 \qquad (9b)$$

$$T_5^4 = 5T_e^4 \qquad (9c)$$

Thus, at the surface, total energy absorbed is given as:

$$\sigma T_e^4 + 4\sigma T_e^4 = 5\sigma T_e^4 \qquad (10)$$

If σT_g^4 is the energy lost from the earth's surface and going by the assumption that the earth surface behaves like a perfect black body where the energy absorbed is approximately equal to the energy emitted and emissivity, $\varepsilon \approx 1$ (approximately) then,

$$\sigma T_g^4 = 5\sigma T_e^4 \qquad (11)$$

Therefore,

$$T_g^4 = (n+1)T_e^4 \qquad (12)$$

Where n is the number of layers considered or optical thickness of the atmosphere, Temperatures at layer 1 (T_1), layer 2, (T_2) and ground surface (T_g) were obtained using Equations 4, 6 and 12, respectively. The temperatures of other layers within the temperatures of the two determined layers were calculated using arithmetic progression expression,

$$L = a + (n-1)d \qquad (13)$$

Where $a = T_2$ = first term, $L = T_1 = T_e$ is the last term, $n = 16$, is the number of layers and d is the common division between the two determined layers 1 and 2.

RESULTS AND DISCUSSION

Table 1 compares the observed and estimated temperatures and longwave radiation at the surface (1.6 x 10^{-3} km) and the top of the troposphere (16.0 x 10^{0} km). The results indicated that the model adequately estimated the temperatures and longwave radiation at different layers within the troposphere. For example, the difference between the observed (31.9°C) and estimated (33.3°C) temperature (that is, bias) was about 1°C at 1.6 x 10^{-3} km (Table 1). There was no observation for the temperature to the top of the troposphere (16.0 x 10^{0} km). However, the model estimated the temperature at this
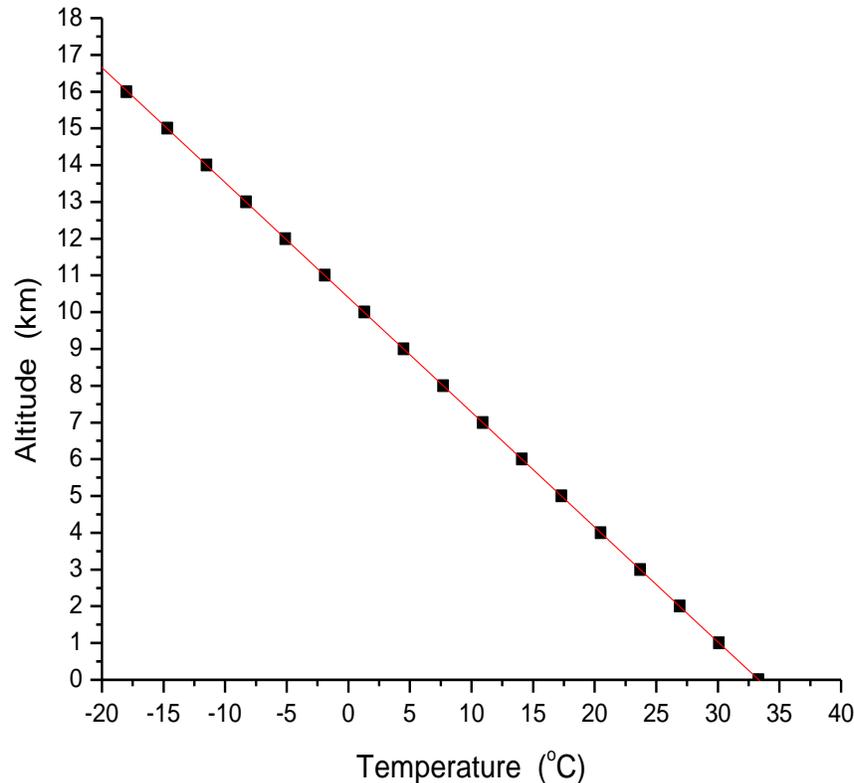
Figure 6. Vertical variation in temperature with altitude over Obafemi Awolowo University Campus, Ile-Ife, Southwestern Nigeria.

height to be -18.0°C. Similarly, the difference between the observed (490 Wm^{-2}) and estimated (499.1 Wm^{-2}) longwave radiation was less than 10.0 Wm^{-2} at 1.6 x 10^{-3} km and the estimated radiation was 239.8 Wm^{-2} at the top of the troposphere.

Generally, our results suggested good agreement between the observation and the model. However, there were slight over-estimations in both the mean temperatures and longwave radiation. Furthermore, the vertical variations in the estimated tropospheric mean temperature over the study area were presented in Figure 6. Results suggested that temperature decreases with height within the troposphere. For example, temperatures at heights 1.6 x 10^{-3} km, 1.0 x 10^{0} km, 2.0 x 10^{0} km, 10.0 x 10^{0} km and 16.0 x 10^{0} km were 33.3, 30.1, 26.9, 1.3 and -18.0°C respectively (Figure 6). This implies that the temperature decreases steadily by -3.2°C/km (dry adiabatic lapse rate) within the troposphere. These results agreed with previous studies (Roger and Richard, 1995; Briggs and Smithson, 1995; Russell, 2009; Scisat-1, 2010) in that temperatures decrease (get cooler) with increasing altitude in the troposphere.

Results of this study also showed that the longwave radiation decreases with height within the troposphere. For example, temperatures at heights 1.6 x 10^{-3} km, 1.0 x 10° km, 2.0 x 10° km, 10.0 x 10° km and 16.0 x 10°

km were 499.1, 478.6, 458.7, 321.0 and 239.8 Wm^{-2}, respectively (Figure 7). These were indications that the longwave radiation decreased steadily by -16.2 Wm^{-2}/km within the troposphere. Then, going by the submission of Briggs and Smithson (1995) that longwave radiation is a function of surface's temperature and Roger and Richard (1995) that temperature decreases with height within the troposphere, it could be deduced that steady decrease in longwave radiation within the troposphere as found in this study was reasonable.

Conclusion

This study used the radiative equilibrium profile model in estimating the vertical variation in the Earth's tropospheric temperatures and Stefan-Boltzmann equation for longwave radiation over a tropical meteorological station located besides Physics Building (7.55°N:4.56°E), Obafemi Awolowo University (OAU) Ile-Ife, Nigeria. The study showed that the model adequately replicated the vertical profile of the tropospheric layer temperature and longwave radiation over the study area. The results of this study were fairly good data resources particularly over the remote areas of the tropics where there are dearth of meteorological measurements.
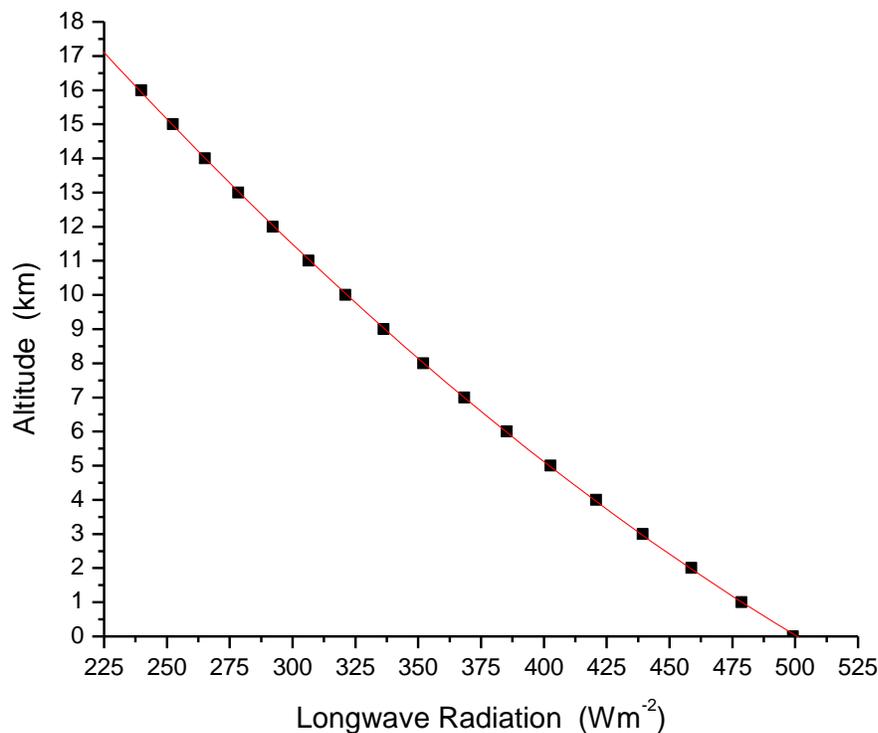
Figure 7. Vertical variation in longwave radiation with altitude over Obafemi Awolowo University Campus, Ile-Ife, Southwestern Nigeria.

REFERENCES

Briggs D, Smithson P (1995). Fundamentals of Physical Geography. Butter and Tanner Ltd. London. P. 558.

Cole FW (1980). Introduction to Meteorology. Canada. John Wiley and Sons. 3rd Edition. P. 505.

Henderson-Sellers A, McGuffey K (2007). A Climate Modelling Primer. University of Michigan. John Wiley and Sons, P. 217.

Olajire MA (2008). Variation in Sky (infrared) Radiation Fluxes over Ile-Ife, Nigeria. M.Sc. Dissertation Submitted to the Department of Physics, Obafemi Awolowo University, Ile-Ife, Nigeria. P. 85.

Olajire MA (2012). Atmospheric Longwave Radiation Balance at a Tropical Location in Ile-Ife, Southwestern, Nigeria. M. Phil. Thesis Submitted to the Department of Physics, Obafemi Awolowo University, Ile-Ife, Nigeria. P. 105.

Ritter ME (2009). 'Radiation and Energy Balance of the Earth System' The Physical Environment: An Introduction to Physical Geography. http://www.uwsp.edu/ geo/faculty/ritter/geog101/textbook/title_page.html.

Roger GB, Richard JC (1995). Atmosphere, Weather and Climate. Rontedge. New York. 392 pp.

Russell R (2009). Temperature in the Troposphere. National Earth Science Teachers Association.

Swinbank WC (1963). Longwave Radiation from Clear Skies. Quarterly Journal of Royal Meteorological Society 89.21.

Scisat-1 (2010). Atmospheric Temperature Profile. John, H. Chapman Space Center David Florida Laboratory Canadian Space Agency Liaison Office.

Full Length Research Paper

Numerical and experimental evaluation of bearing capacity factor Nγ of strip footing on sand slopes

Mohd Raihan Taha* and Enas B. Altalhe

Department of Civil and Structural Engineering, Universiti Kebangsaan Malaysia, 43600 UKM Bangi Selangor, Malaysia.

Results of laboratory model tests and numerical studies on the behavior of a strip footing adjacent to a sand slope are investigated and presented in this paper. The investigated parameters include the effects of depth of the first reinforcement layer, vertical spacing, number of reinforcement layers, and distance between the edges of footings on bearing capacity. Results were analyzed to determine the effects of each parameter. Using a strip footing located near a sand slope crest had a significant effect on improving bearing capacity. The improvement increased when relative density decreased. The depth of the first layer decreased with further improvement when the distance of the footing edge from the slope crest increased. Using a strip footing can be considered effective in controlling the horizontal movement of the subgrade and in decreasing slope deformation. Finite element analysis explained and identified the failure pattern of strip footings adjacent to a slope crest. The findings also confirmed the load transfer mechanism and showed how a slope can be protected when geotextile is used.

Key words: Strip footing, slope stability, plaxis, bearing capacity, scale effects.

INTRODUCTION

Rapid population growth and urbanization have resulted in increased construction areas and the decrease of suitable settlement areas. As a result, the bearing capacity and settlement criteria for building construction are changing. The use of unwanted soil has also become obligatory. Engineering structures, foundation systems, ground transportation, and living conditions are usually designed by using shallow foundations, which becomes problematic with regard to certain types of soil. The most commonly used solution is deep/pile foundation, which is applied by selecting the foundations of a building. Deep/pile solution is expensive. However, rapid advancements in construction technology that provide new solutions to problematic surfaces have made deep/pile solution necessary. Several methods in soil solution have been developed since the 1970s

and improved problematic soil strength properties. Economical methods based on deep foundation system solutions can be applied in certain cases. Geotechnics, which is a type of reinforced soil application, is one of the commonly used solutions. Reinforced soil application takes various resistant elements in the soil reinforcement placement depending on the obtained composite reinforcement material.

The concept of soil reinforcement was introduced in 1968 by French engineer Henri Vidal. Several theoretical and experimental geotechnical engineering studies have followed Vidal's proposal. Vidal (1968) implemented soil reinforcement by using a metal strip and reinforcing material. After the 1980s, along with technological advancement, the location of the metal strip used in synthetic geotextile and geogrid materials such as

*Corresponding author. E-mail: profraihan@gmail.com or enasraft@yahoo.com. Tel: +603-89216218, Fax: +603-89216147.

polymer raw materials, was developed. Geotechnical engineering is practical and promotes the use of economical geosynthetic structures and materials. Thus, geotechnical engineering is increasingly applied to constructing dams, roads, landfills, and retaining structures.

Geotextiles and geogrids are the most commonly used geosynthetic materials in geotechnical application. Geotextiles enable more separation and filtration, and are used for drainage. Geogrids, which have lower metal rigidity, reduce ground transportation through strength and expected settlement. Although geogrids have a coupling effect with the ground through grid-shaped openings, these mechanisms tend to perform effectively.

Studies were conducted on flat-surfaced floors, foundation bearing capacity, and settlement behaviors based on improvement from using geogrid reinforcement (Binquet and Lee, 1975a; Akinmusuru and Akinbolade, 1981; Fragaszy and Lawton, 1984; Guido et al., 1985; Huang and Tatsuoka, 1990; Mandal and Sah, 1992; Dixit and Mandal, 1993; Khing et al., 1993; Yetimoğlu et al., 1994; Adams and Collin, 1997; Laman and Yildiz, 2003; Kumar and Saran, 2003; Michalowski, 2004; Kumar and Walia, 2006). However, in certain cases, foundations are constructed on or near slopes (bridge piers, utility poles, and buildings). In such cases, non-transportation capacity of the inclined surface decreases significantly.

In cases where the foundation is built on a slope, one of the solutions to increase bearing capacity is to place the foundation at a sufficient distance away from the top of the slope, which reduces the impact of transportation capacity. An alternative method is using transportation to increase geogrid reinforcement capacity. However, using transportation is not economical. A limited number of studies on strip foundation have been conducted. Selvedurai and Gnanendran (1989) and Lee and Manjunath (2000) used a single reinforcement layer and examined the effects of a strip foundation on the bearing capacity. Huang et al. (1994) started a research using geotextile reinforcement and it explained about failure mechanism on sand slope. Yoo (2001) and Laman et al. (2007) used a multi-layer case in their experimental studies. Bathurst et al. (2003) conducted a large-scale experiment to examine the failure mechanism. El Sawwaf (2007) investigated clay on the parameters of tapered equipment for sand filling. Previous analyses and experiments that mostly focused on single angle of slope, stability, and uniform basic width used geogrid reinforcement.

Moghaddas and Khalaj (2008) conducted an experimental study on the benefits of geogrids to the deformation of small-diameter pipes and settlement of the soil surface when subjected to repeated loads that simulate vehicle loading. According to the report, using geogrid reinforcement can significantly reduce the vertical diameter change of pipes and the soil surface settlement. El Sawwaf and Nazir (2010) conducted a laboratory study on the effects of geosynthetic reinforcement on the cumulative settlement of repeatedly loaded rectangular model footings placed on reinforced sand. Repeated load tests were performed with different initial monotonic load levels to simulate structures. Live loads, such as petroleum tanks and ship-repair tracks, changed slowly and repeatedly.

Moghaddas and Dawson (2010) and El Sawwaf and Nazir (2012) studied repeated loads and cyclic loads, respectively, on model strip footings. A series of experiments were conducted to investigate the behavior of strip footings supported on three-dimensional and planar geotextile-reinforced sand beds subjected to repeated loads. The aforementioned researchers determined the effects of partial replacement of compacted sand layer and the inclusion of geosynthetic reinforcement. They found that the efficiency of sand-geogrid systems was dependent on cyclic load properties and on the location of the footing relative to the slope crest.

Scale effects between laboratory and field testing of footings were explored by a number of researchers (Berry, 1935; De Beer, 1963; Bolton and Lau, 1989; Das and Omar, 1994; Tatsuoka et al., 1994; Kusakabe, 1995; Kerry et al., 1999; Banimahd and Woodward, 2006; Cerato and Lutenegger, 2007; Kumar et al., 2008; Chang et al., 2010). Scale effects were presented by Berry (1935), who showed that the bearing capacity of model circular footings increases disproportionately with increasing footing size (50.8, 71.8, 101.6, and 143.7 mm) on dense sand held at the same relative density. The bearing capacity factor Nγ decreases with increasing footing size Nγ. The bearing capacity can be calculated as follows:

$$q_{ult} = \frac{1}{2}\gamma' B N_\gamma \tag{1}$$

Generally, the bearing capacity factor ($N_{\gamma q}$) from model footings depends on footing width B. The magnitude of $N_{\gamma q}$ increases as the footing size decreases (De Beer, 1965; Das and Omar, 1994; Clark, 1998; Zhu et al., 2001; Lancelot et al., 2006; Cerato and Lutenegger, 2007). The increase of $N_{\gamma q}$ with the decrease of footing size becomes particularly extensive when the footing size becomes smaller than 1 m (Banimahd and Woodward, 2006). Kumar et al. (2008) conducted small-scale model tests with 7 cm strip footing and found that the value of $N_{\gamma q}$ was extremely high. In the present paper, the footing size is only 5 cm. Thus, the value of $N_{\gamma q}$ may be extremely high. Tatsuoka et al. (1991, 1994) reported that the scale effects were due to two factors: mean stress level beneath the footing and particle size. Bolton and Lau (1989) and Kusakabe (1995) stated that the particle size effect ($B/d_{50\%}$) was insignificant to the results when ($B/d_{50\%}$) was greater than 50 or 100. The value of ($B/d_{50\%}$) is approximately 100 in the present study. Consequently,
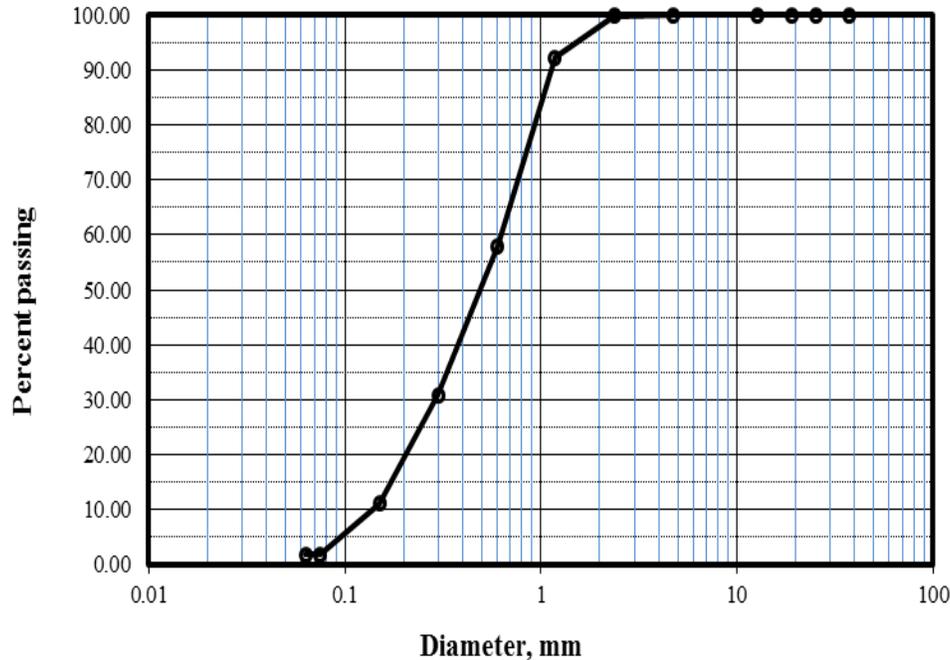
Figure 1. Grain size distribution of sand.

the particle size effect can be avoided. Unless the bearing capacity factor is modified, the effect of the first factor is difficult to account (Shiraishi, 1990). Kusakabe et al. (1991) showed that shape factor decreases by 33% as a footing size increases up to 3m.

In the present study, unreinforced, geotextile-reinforced, and increasing footing width B (unreinforced and reinforced) strip foundation bearing capacity, and settlement behavior of place on sandy slopes were investigated through laboratory model tests. In the unreinforced case, we studied the distance from the top of the foundation slope and the degree of stabilizing behavior of bearing capacity based on the effects of the parameters. In the reinforced case, the number of reinforcement layers and behavior of the parameters were investigated along with effects on bearing capacity factor. Based on the ratio of the distance from the slope crest to the footing width, basic size, and bearing capacity factor, we obtained the optimum reinforcement parameters. The effects of increasing footing width B in shear strength parameters were also experimentally determined in the unreinforced and non-woven geotextile-reinforced models for the availability of the fillings which was investigated. The availability of the fillings was determined by the value of the largest bearing capacity. In our study, unreinforced and reinforced foundations on the sand slopes were simulated by using computer software PLAXIS with two-dimensional and plane strain conditions. The numerical solution of the finite element method (FEM) was obtained. The results were compared with the experimental results.

MATERIALS AND METHODS

Tests on model footings

Test equipment

The apparatus used for the model tests consisted of a cuboid soil bin that measures 2,000 mm × 600 mm × 620 mm, a loading frame, a hydraulic jack, a pumping unit, and measuring devices for load settlement monitoring. The test tank was made rigid to prevent volume change during test bed preparation and during the load test. To accommodate the bearing ball, a 50 mm × 15 mm thick rigid steel footing with a notch hole at the top center was used as the model footing. The length of the steel footing was kept equal to the length of the tank (600 mm) to ensure the strip footing behavior and the plane strain condition. A controlled pouring and tamping technique was adopted to obtain the required unit weight of sand in the tank. The load was transferred to the footing by using a bearing ball, which produced a hinge. The hinge enabled the footing to rotate freely as it approached failure and eliminated any potential moment transfer from the loading fixture. Settlement of the footing was measured by using two mechanical dial gauges with least count of 0.01 mm. Medium coarse sand with grain size that ranges from 0.06 to 2.00 mm was used. Grain size distribution of the sand is shown in Figure 1. Optimum moisture content was determined by using a standard Proctor test and was found to be approximately 10%. Different relative densities of the sand were used by forming the designed weight of the sand into a certain volume of the soil bin by compaction.

Numerical modeling

Experimental results were verified through numerical modeling by using FEM. Plane strain elastoplastic finite element analysis (FEA) was conducted by using the commercial program PLAXIS 2D
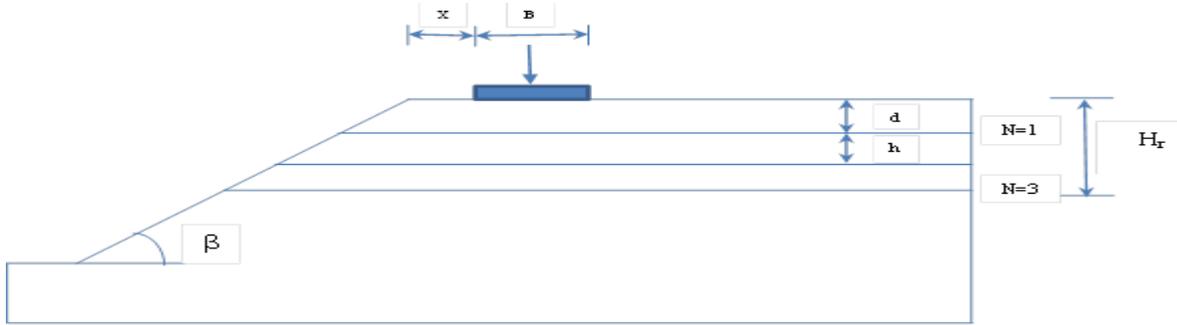
Figure 2. Slope geometry and parameters.

(Bringkgreve and Vermeer, 1998; Plaxis, 2002). PLAXIS can address a wide range of geotechnical problems, such as deep excavations, tunnels, and earth structures (for example, retaining walls and slopes). Prototype slopes were supposed to rest on a yielding foundation and extend laterally to a distance of 1.5 times the slope height (H) from the toe of the slope. The initial conditions generally comprise the initial groundwater conditions, the initial geometry configuration, and the initial effective stress state. The sand layer was dry, which made implementing ground water condition unnecessary. However, the analysis required the generation of initial effective stresses via K0 procedure. The geometry of the prototype footing slope system was supposed to be similar to that of the laboratory model (footing width B = 50 mm; thickness and slope height = 600 mm). The same inclination of model test slopes, 2(H):1(V), and geotextile sand were used in the prototype study. The software enabled the automatic generation of 6- or 15-node triangle plane strain elements for the soil.

RESULTS AND DISCUSSION

The load–settlement curves obtained from the experimental ultimate bearing capacity (q_u) and the amount of settlement at the time of failure (S) were determined. Given the subsequent reduction of the bearing capacity of the slope, the bearing capacity reduction coefficient (j_β) was determined as

$$j_\beta = \frac{q_u}{q_{u(\beta=0)}}$$

where $q_{u(\beta=0)}$ was the ultimate bearing capacity of the strip footing on a flat surface (Figure 2). Table 1 shows the unreinforced test program. We investigated the following effects of geometrical parameters on the bearing capacity of strip footing on reinforced sand slope experiments (Figure 2):

(a) Ratio of depth of the first layer to the footing width (d/B).
(b) Ratio of distance from the slope crest to the footing width (X/B).
(c) Vertical spacing between layers to the footing width (h/B).

Table 1. The unreinforced test program.

Test No	β˚	Dr%	B (mm)	X/B
Ur1*	0	85	50	-
Ur2	30	85	50	0
Ur3	30	85	50	1
Ur4	30	85	50	2
Ur5	30	85	50	3
Ur6	30	85	50	4
Ur7	30	85	50	5
Ur8	30	85	70	0
Ur9	30	85	70	1
Ur10	30	85	70	2
Ur11	30	85	100	0
Ur12	30	85	100	1
Ur13	30	85	100	2
Ur14	30	85	150	0
Ur15	30	85	150	1
Ur16	30	85	150	2
Ur17	30	60	50	0
Ur18	30	60	50	1
Ur19	30	60	50	2
Ur20	30	60	70	0
Ur21	30	60	70	1
Ur22	30	60	70	2
Ur23	30	60	100	0
Ur24	30	60	100	1
Ur25	30	60	100	2
Ur26	30	60	150	0
Ur27	30	60	150	1
Ur28	30	60	150	2

(d) Increase of width footing (B).
(e) Number of reinforcement layers (N).

The behavior of bearing capacity and settlement of strip footing on reinforced slope was examined, as well as the bearing capacity values based on the sizes and types of equipment used for the tests. The multi-layer reinforced d
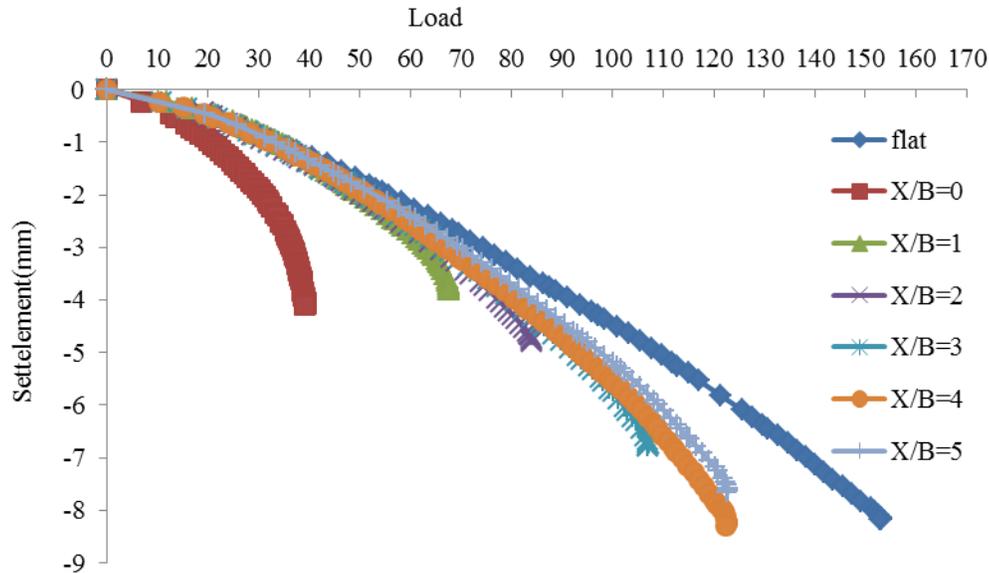
Figure 3. Load variations with settlement for different edge distances of strip footing on the slope (D_r=85%, and β=30).

was also obtained from the experiment. The optimum values of parameters h and N were used, which reinforced the basic parameters related to width B. The value calculated by the ratio (d/B, h/B, H_r/B, and X/B) was expressed. To make the optimum values of the strip footing width B dimensionless, the experimental results evaluated the reinforcement. The load settlement curves obtained from the experiment, the ultimate bearing capacity, and the settlement values were determined at the time of failure. Given the reinforcement to express a given increase in bearing capacity, the bearing capacity ratio (BCR) can be expressed as follows:

$$BCR = \frac{q_{ur}}{q_u}$$

q_{ur} : Reinforcement ultimate bearing capacity

q_u : Non-reinforcement ultimate bearing capacity

The reinforcement that results from the decrease in settlement values is referred to as the settlement reduction factor (SRF), which can be expressed as follows:

$$SRF = \frac{S_r}{S}$$

S_r : Settlement value of reinforced sand slope

S : Settlement value of unreinforced sand slope

**Effect of edge distance of strip footing on bearing capacity**

To investigate the footing on the slope, the laboratory experiments were placed at a total of seven different distances. In the experiments, footing width B = 50 mm, β = 30°, and Dr = 85% were selected as the degree of firmness. Load (q) and settlement (S) curves are illustrated in Figure 3. The maximum values clearly showed the curve collapse load, which was determined as q_u. In the tapered case, with the value obtained from the payload, the payload will slope the value obtained from the ratio of the case by a factor of $i_β$. The q_u values in different X/B and the rates are summarized in Table 2. The relationship between X/B and $i_β$ is illustrated in Figure 4. With a different edge distance of the strip footing on the slope, the following results were obtained from the experiments on the effects of bearing capacity.

   With consideration for the distance of strip footing in selecting between the 0B and 5B experiments, the X/B ratio increased, and the value of the underlying bearing capacity increased the lateral support that was lost as a result of reactivating the entry. As a point was placed sufficiently far from the top, we beveled the remaining portion of the main ground floor. The failure occurred in the right wedge, which was partly because of passive resistance that increased the payload. The largest increase in bearing capacity X/B = 0 and X/B = 1 was between (19%) and X/B = 2 with the constant distance increased significantly (10%). In X/B = 3, the value of state approximately corresponds to 70%. The increase in bearing capacity X/B = 4 and X/B = 5 showed a 1% decrease, and X/B = 5 to 80% of the value of reaching

Table 2. Ultimate bearing capacity test results (D_r = 85% and β = 30).

X/B	qu(kN/m^2)	S(mm)	i_β
0	39.27	-4.06	0.256315
1	67.64	-3.72	0.441486
2	83.98	-4.75	0.548137
3	107.16	-6.74	0.699432
4	122.58	-8.22	0.800078
5	122.87	-7.59	0.801971
Flat	153.21	-8.16	1
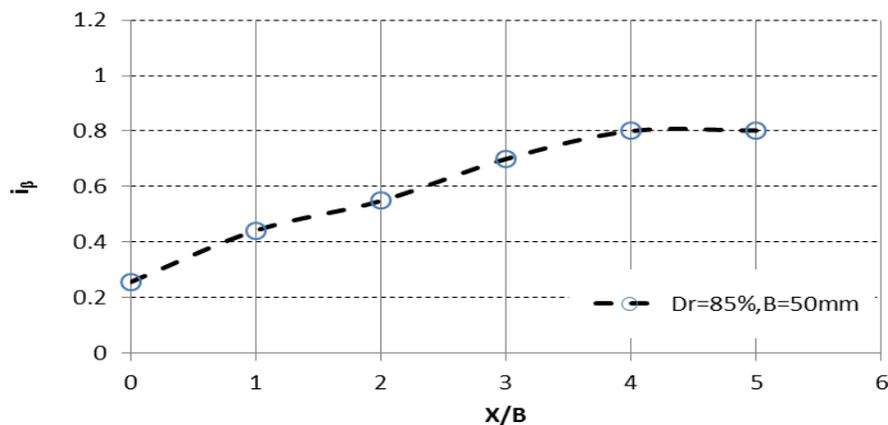
Figure 4. Bearing capacity of strip footing on different slope distances.

out. The effect of the payload was largely irrelevant. As the X/B value increased, the load settlement became steeper. With increasing curves and dips, the value of X/B is less than 4.

Effects of number of geotextile layers on settlement

The efficiency of reinforcement on the settlement of strip footing was investigated. Figure 5 illustrates the differences between the load–settlement curves of unreinforced and reinforced soil mass. The difference in ultimate bearing capacity was caused by the difference in the slope at the near end of the curves, which results in increased settlement by the increase of reinforced layers. The method of settlement calculated by the load settlement curve is presented in Figure 5. Table 3 provides the results obtained for (Dr = 85%, X/B = 1, and β = 30°).

As shown in Table 3, the foundation settlement increased with reinforcement. However, using one-layer reinforcement seems logical when increasing bearing capacity and allowable quantities of settlement are considered. Relative to other situations, reinforcement is unnecessary because both settlement of footing and the

bearing capacity increase. For example, the bearing capacity of soil mass with three-layer reinforcements and unreinforced soil was obtained (358.9/67.4). However, the settlement increased in the three-layer reinforcement, which was caused by the tension rupture of the soil confined between geotextile layers.

Comparisons of Table 3 and Figure 5 indicated similar results for the two cases of edge distance. Therefore, using reinforcement in sand slope with a large edge distance is beneficial because it increases bearing capacity, although the settlement increased compared with unreinforced soil. The settlement process is still increased by adding reinforcement layers. In investigating the effect of reinforcing the bearing of the number of layers, experimental studies showed that as the number of reinforcement layers (N) increased, so did the reinforced soil bearing capacity. The optimum reinforcement layer was found to be N = 3. In this case, the effective reinforcement depth (Hr) is 2.5 B. Figures 6 and 7 show that according to the optimum reinforcement layer, an increase of 3.2 times was observed in the number of loads.

An increasing number of reinforcement layers contribute significantly to the bearing capacity of the slope. The bearing capacity increased with the passive
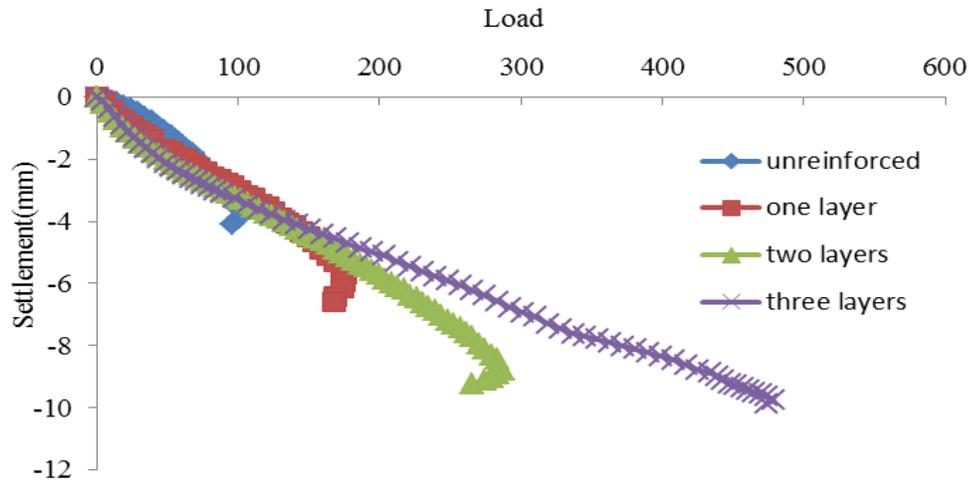
Figure 5. Load–settlement curves for different numbers of reinforcement layers at $D_r = 85\%$, X/B = 2, and β=30°.

Table 3. Variation of footing settlement and bearing capacity for reinforcement soil.

Soil type	Bearing capacity	Footing settlement (mm)
Unreinforced	67.4	4.375
One reinforced layer	158.9	4.66
Two reinforced layers	283.5	6.7
Three reinforced layers	358.9	9.22
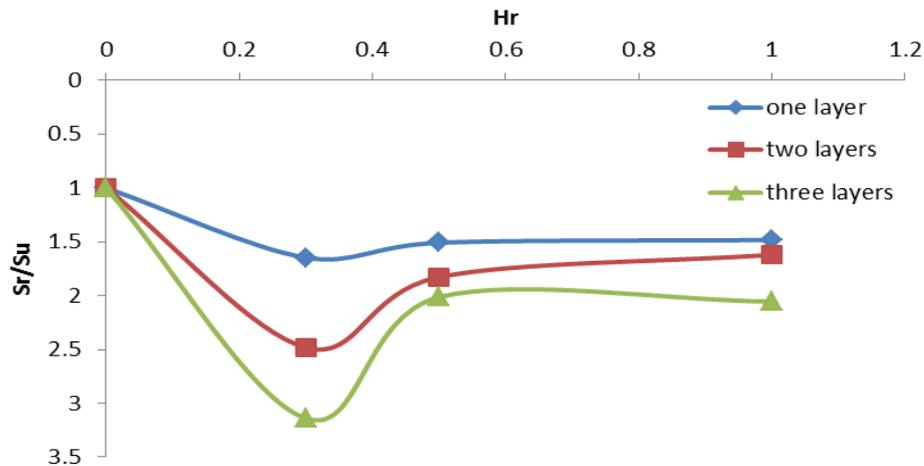
Figure 6. Variation of Hr with Sr/Su.

resistance of the ground, which consists of sand, and the soil–geotextile reinforcement mechanism can be said to be due to adhesion. Reinforcement is composed of tensile, shear stresses below the footing against the horizontal layer, which exhibits resistance, and the stress shows a more stable soil layer that transfers a failure in a wider and deeper zone.

Table 3 shows the value of qu experiments, which corresponds to approximately the same value of q in sitting rates in unreinforced and reinforced cases. Figure 8 shows the Hr–SRF given relationship. Based on Table 3 and Figure 8, if strip footing is placed in the soil
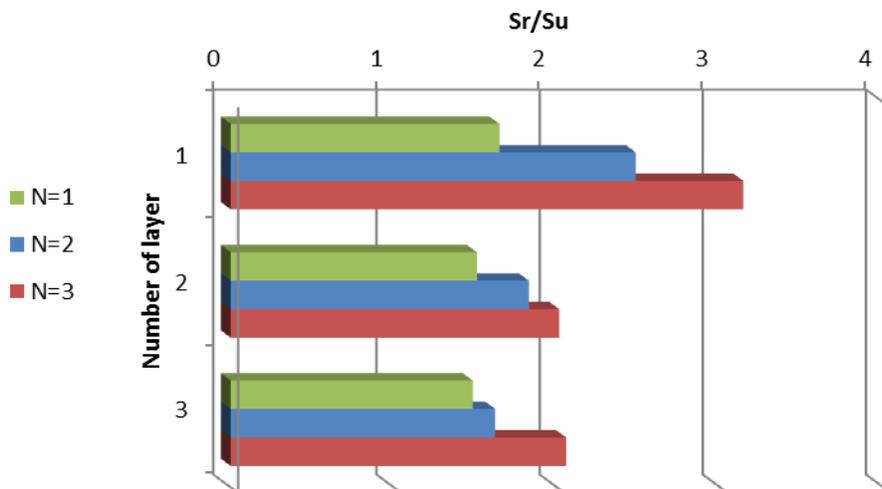
**Figure 7.** Variation of Sr/Su with number of layers.
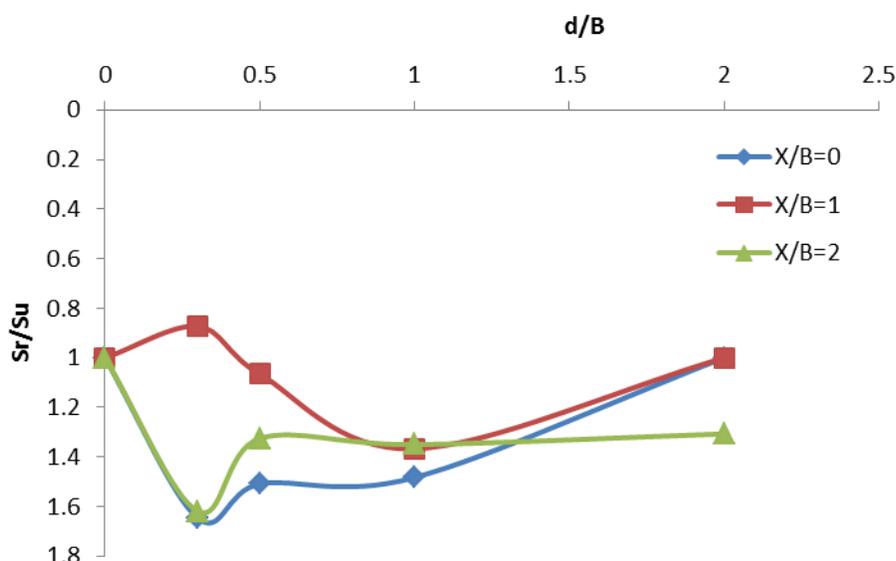
Figure 8. Variation of Sr/Su with depth of first layer.

reinforcement layer of N = 3, then the strip footing decreases under the same load values. The improvement in the strip behavior of the N = 3 reinforcement reached approximately 45% of the value of the number of layers N = 4.

FEA results

FEA results are shown in Figures 9a to h. Figure 9a presents a typical deformed FE mesh for strip footing on reinforced sand slope in the case of (X/B = 1, β = 30°, and d/B = 0.5). A small deformation is shown, which is a significant feature of the reinforced sand slope, unlike the unreinforced case. The presence of geotextile significantly decreased the deformation of both underlying soil and slope compared with the footing without geotextile. This observation can be confirmed by the displacement vector obtained from the analysis and shown in the following figures 9b. The geotextile layers decreased subgrade deformation and prevented particles from moving to the region surrounded by the geotextile layer. The geotextile layers provide lateral restraint, which controls the horizontal movement of soil particles under the footing and mitigates slope deformation (Figure 9c). The geotextile layers also decrease the horizontal movement of subgrade particles. The extreme horizontal displacement also developed beyond the confined region
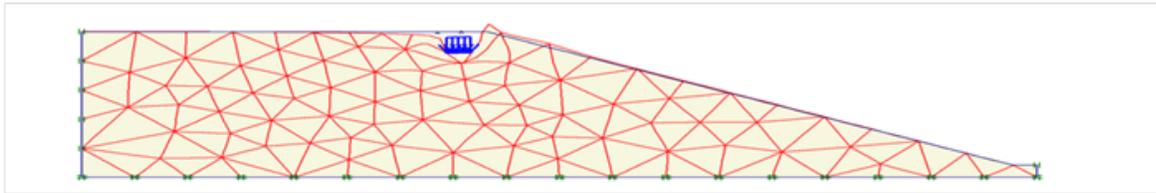
1) Without reinforcement
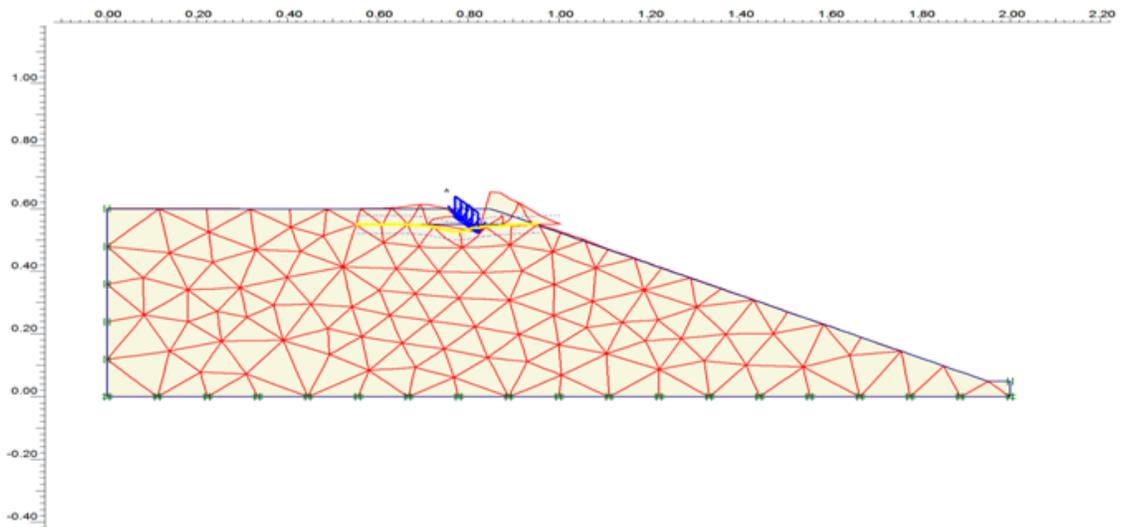

2) One-layer reinforcement

(a) Distorted FE
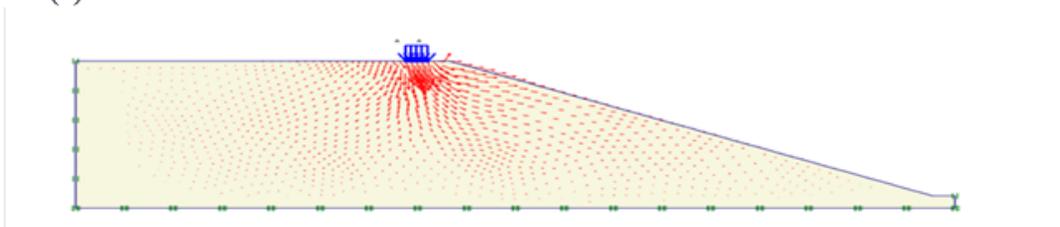
1) Without reinforcement
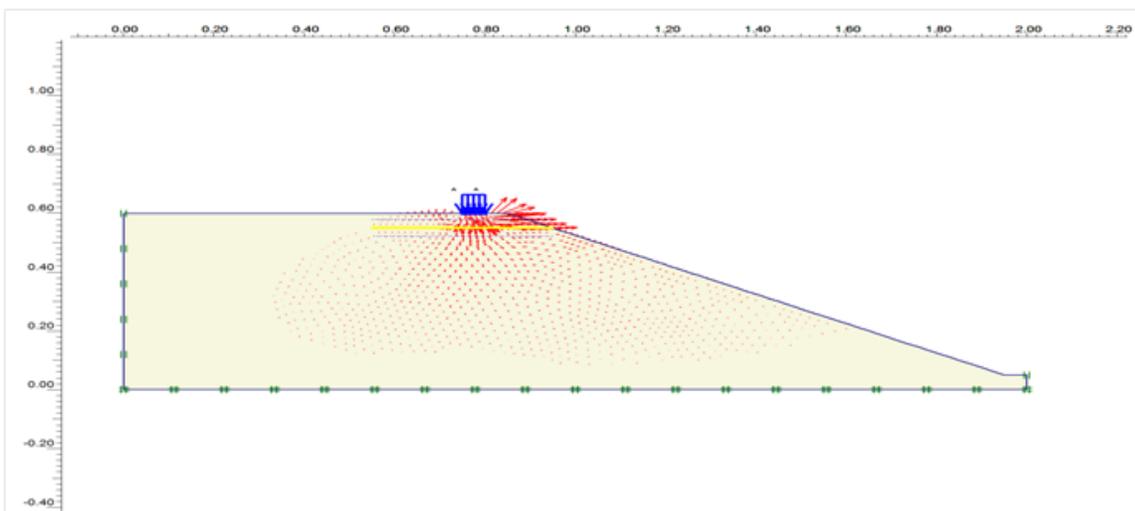
1) One-layer reinforcement

**b) Total displacement vector**
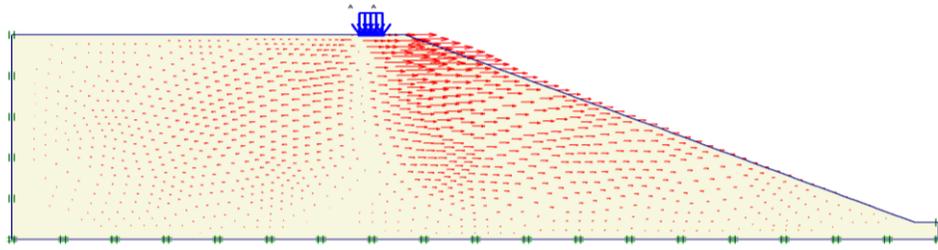
1)   Without reinforcement
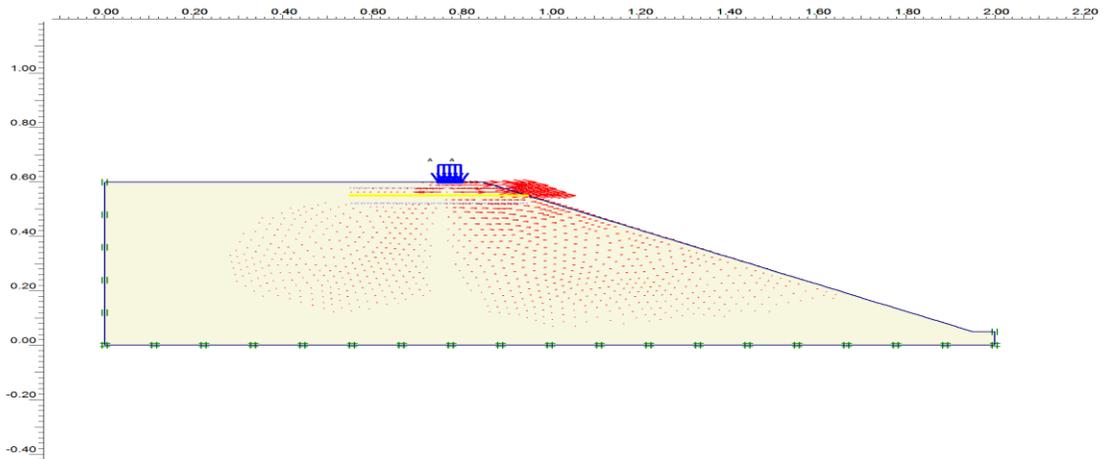
2)   One reinforced layer
**(c) The horizontal displacement vector**
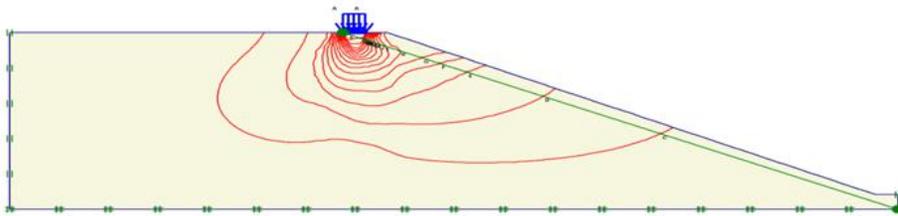
1) Without reinforcement
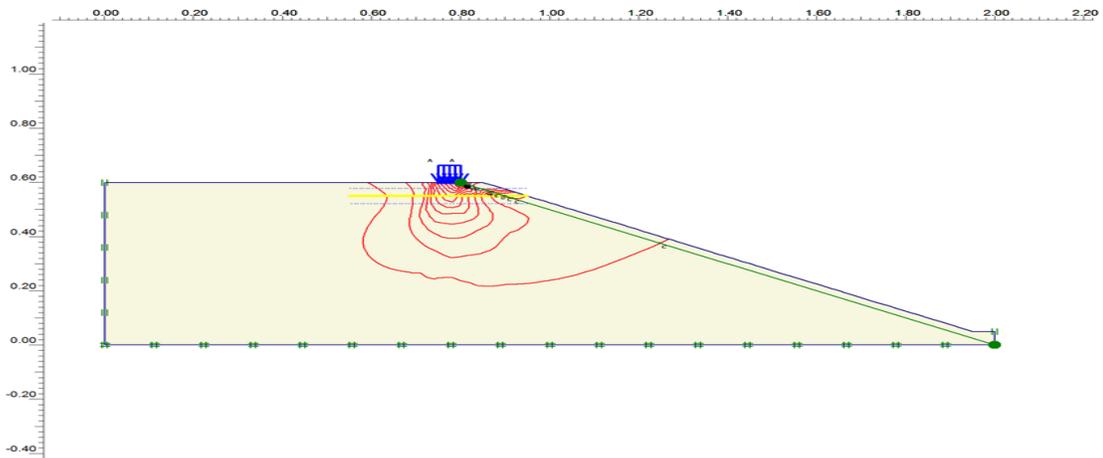
2) One reinforced layer
**d) Horizontal displacement contours**
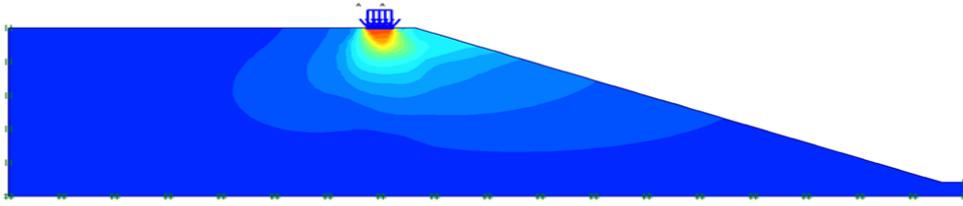
1) Without reinforcement
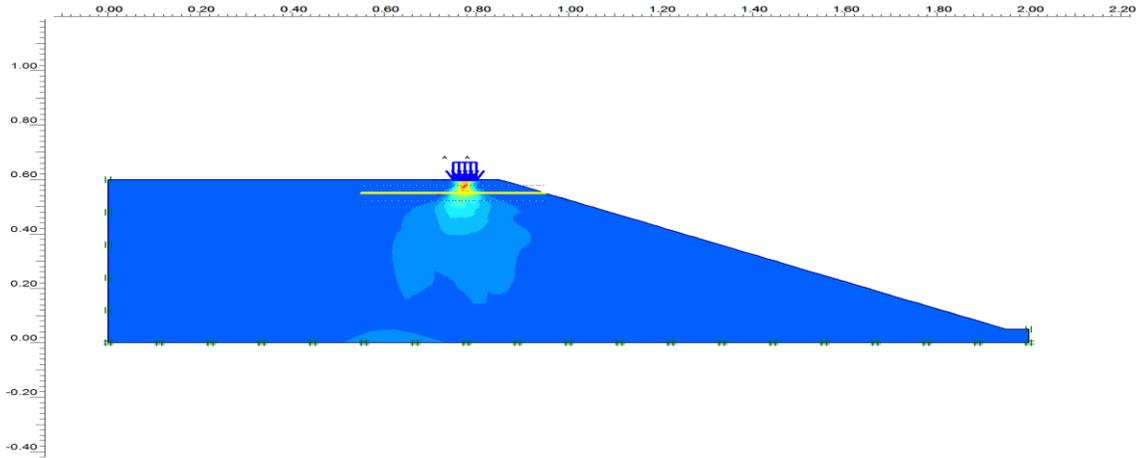
2) One-layer reinforcement
e) Shading of mean stresses
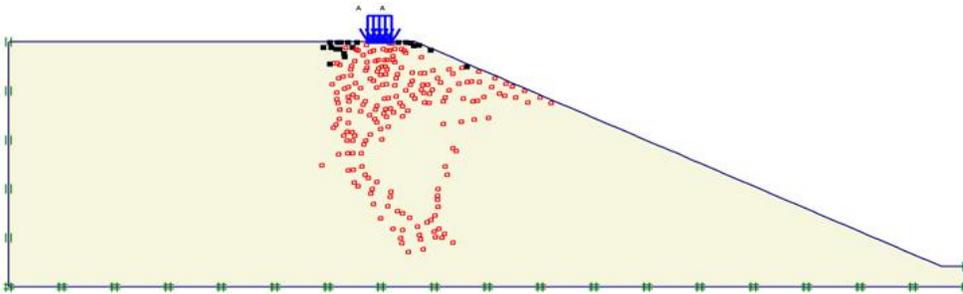
1) Without reinforcement
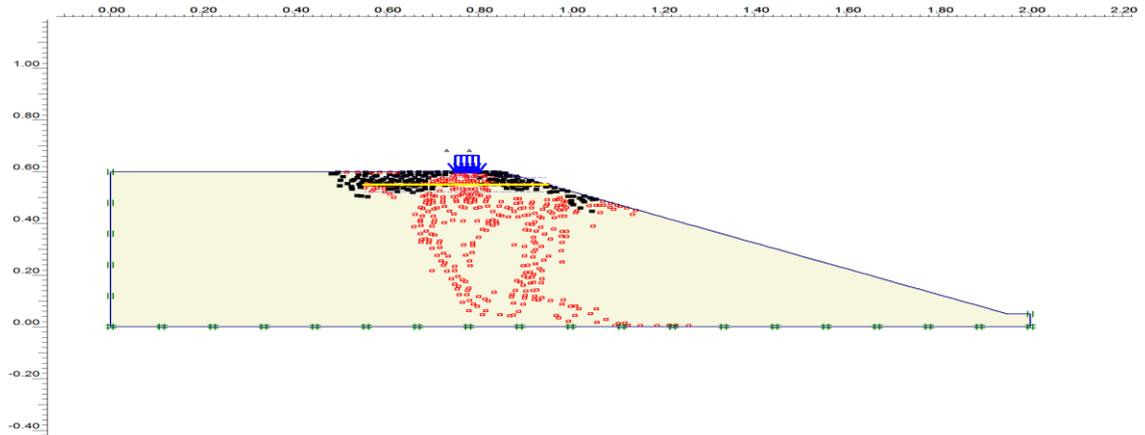
2) One-layer reinforcement
**f)   Plastic points for geotextile**
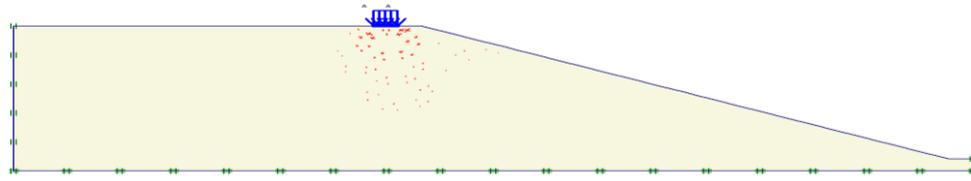
1) Without reinforcement
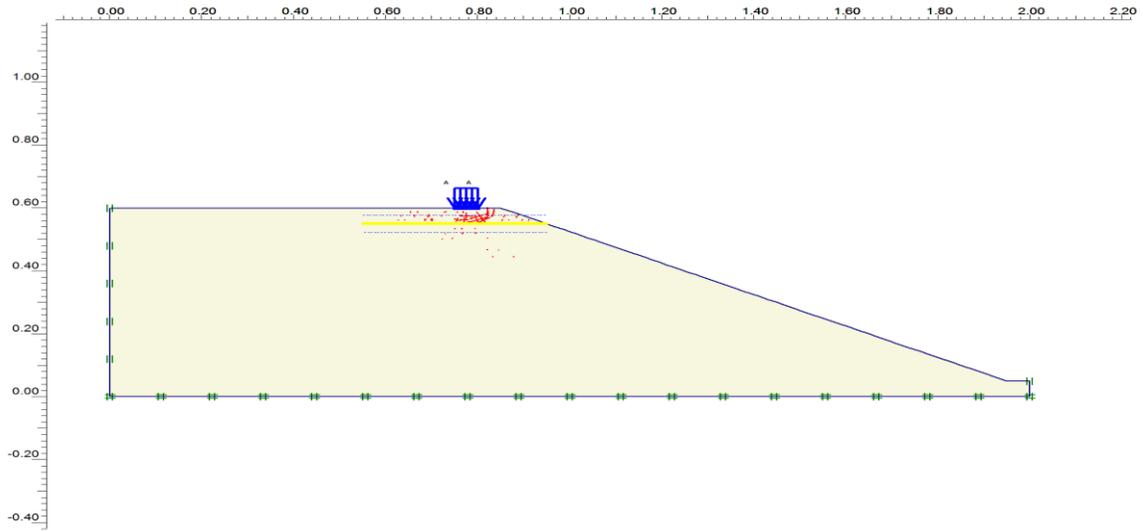
2) One-layer reinforcement
(g) The principal strain location
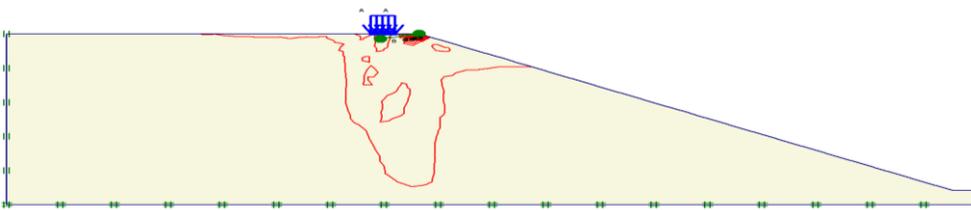
1)   Without reinforcement
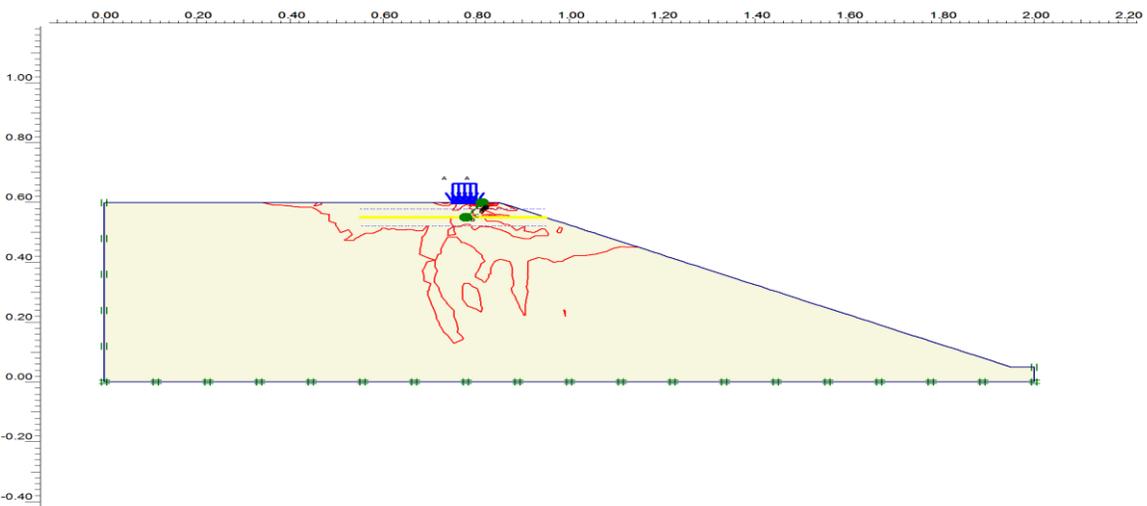
2)   One-layer reinforcement
(h) The contours of principal strain

Figure 9. Horizontal displacement contours in soil mass under footing placed on: (a) unreinforced slope, (b) reinforced footing (d=B).

(Figure 2d), which exhibits contours of extreme horizontal displacement. Figure 2d identifies slope zones in which subgrade particles have a large horizontal displacement. The displacement was mainly observed at the zones located below the confined subgrade and was extended vertically within a distance of nearly 0.5 B (Figure 9d). The convergence between the contours was densely located below the confined zone.

Generally, horizontal displacement of the confined particles is almost null when geotextile layers are located beyond depth 2 B. As the depth of the reinforcement layer decreases, the horizontal movement of the subgrade increases to the outside region. Thus, slope deformation also increases. The geotextile layers provide lateral restraint, which modifies the stress distribution zone under the base (Figure 9e). The extreme values were located between the following.

The stress shading denotes the absence of resistance in the soil adjacent to the slope as a result of the slope effect (left side). However, resistance on the right part was observed because the shading in the adjacent soil increased densely as the geotextile layer transmitted the stress to the soil. This observation can be confirmed by plastic or stress point distribution along both sides of the geotextile layer, which was observed along the length of the geotextile layer.

Figure 9f shows the distribution of the plastic points beneath the footing with the geotextile layer. Plastic points are referred to as stress points in the plastic states, which can be observed mainly at the zone above the geotextile layer. Small plastic points are illustrated below the region, which indicates that shear failure can be expected at the outside region below the reinforcement layer. This observation also indicated that soil shear failure occurred mostly beyond the reinforcement layer as expected. Moreover, the shear strains decreased through the reinforced zone (Figure 9g), which represents the distribution of the principle shear strains. As also shown in Figure 9g, the geotextile layer transferred the stress to the adjacent soil, which produced strains at each edge. This finding indicates that geotextile layers have a considerable effect on decreasing shear stress in the reinforced zone. In addition, the contours of shear strains (Figure 9h) indicate that shear failure will develop at the end of the reinforced region.

Given that the main contours were extended below the reinforced soil, shear failure developed in a deeper location. The location where the maximum shear strain converged was regarded as a slip surface where shear failure initiates. Propagation of the high-strain zone at the end of the reinforced region caused progressive failures.

Figure 9 shows that the load transfer mechanism occurs in a deeper zone below the geotextile layer, which explains the occurrence of shear failure. The main function of the reinforcement layer is to reduce the distortion rate in the sheared zone and the ultimate shear stress mobilized in the shear zone. Thus, the bearing capacity failure can be modified to punch the shear failure under the footing, and the general bearing capacity failure occurred at the top geotextile layer.

## Comparison between experimental and numerical results

Initially, the numerical model used the results obtained from the experimental test program of this study. Figure 10 shows a comparison between the BCR values obtained from FEA and the results obtained from the experimental model tests. FEA results have a reasonable fit with the experimental data and are in accordance with the same trend. Figure 10 also shows the experimental and numerical results of three tests: X/B = 0, X/B = 1, and X/B = 2. Although the numerical results do not fit completely with the experimental results, the results are in good agreement. Any discrepancy may be related to the chosen model, soil, and foundation parameters, and differences between the boundary conditions in the numerical and experimental models.

Figure 11 shows the typical results of load curves for the strip footing tests on sand slope. The results were obtained from the bearing capacity tests on sand slope at a density of $D_r = 85\%$. The failure modes for each of the footings varied depending on the sand type and density. The curves showed that large strip footings have a higher bearing capacity than small strip footings, which was also the case for tests on each density. The results also indicated that values of N_γ for sand decreased with the footing size and increased higher relative density. The relative density also had a significant influence on N_γ (Figure 12). The results shown in Figure 12 suggest that as the footing width decreased, N_γ increased significantly faster than that which was previously noted.

The failure mode of the footings varied depending on density and footing size. To explain the observed different behaviors, the footings were related to the critical state concept. The concept suggests that dense sand under large mean stresses tend to contract. The same concept can be related to footings of different widths. For example, if four footings of various sizes were placed on the same sand in the same state and in the influence area, the mean stress of the four footings would be different. The largest footing would have the largest influence area, and the smallest footing would have the smallest influence area.

The bearing capacity factor $N\gamma$ depends on the absolute width of the footing for strip footing (Figure 12). The $N\gamma$ for strip footing decreased with the footing size but increased with the increasing relative density. One explanation for the scale effect is stress dependency, in which different footing sizes have different mean stresses, which means that a smaller footing indicates a smaller mean stress. The observation is related to the
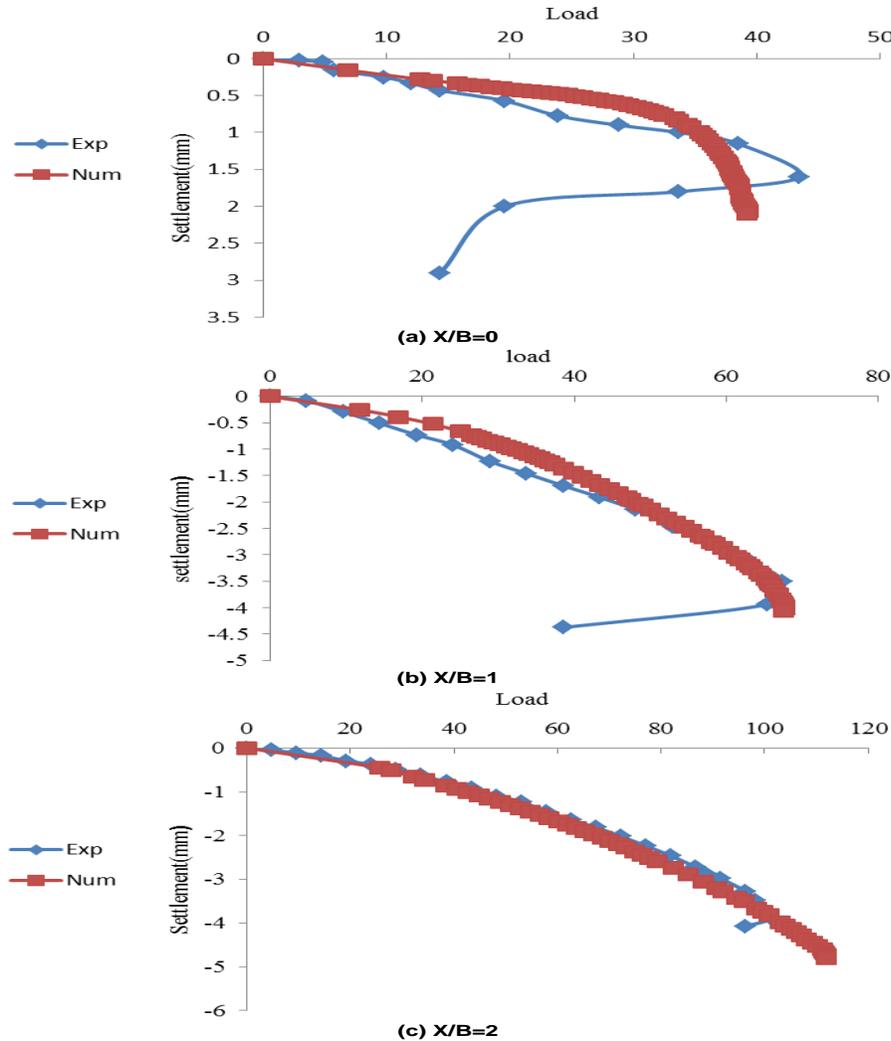
Figure 10. Experimental and numerical results of test with D_r=85% (a) X/B = 0; (b) X/B = 1; and (c) X/B = 2.

critical state strength. A small footing (small mean stress) would function as if it was on denser soil than a larger footing, despite being tested on sand with the same void ratio. The stress dependency may also be related to the curvature of the Mohr–Coulomb failure envelope where high friction angles at low stresses and low friction angles at high mean stresses were observed. The curvature of the Mohr–Coulomb failure envelope has been widely documented and can explain why small footings have large Nγ values. Thus, large friction angles correspond to the dense state of soil in relation (Ψ) to the critical state line.

Effect of Ψ on bearing capacity factor Nγ

The bearing capacity factor Nγ depends on the soil unit weight γ and can be calculated by assuming

cohesionless soil (C = 0) with no surcharge (q = 0). The generalized Terzaghi's bearing capacity equation is given as:

$$q_u = \frac{1}{2} B \gamma N_\gamma$$

where N_γ is the bearing capacity factor for strip footing.

Table 4 lists the values of the bearing capacity factor N_γ for X/B = 0.0, 1.0, and 2.0, which shows the variation of N_γ with Ψ, X/B, and B for strip footing. Figure 13 shows the variation of N_γ with B and Ψ for strip footing widths of 50, 70, 100, and 150. N_γ increased considerably with increasing X. The dilatancy had a significant effect on the value of the bearing capacity factor, particularly for high X
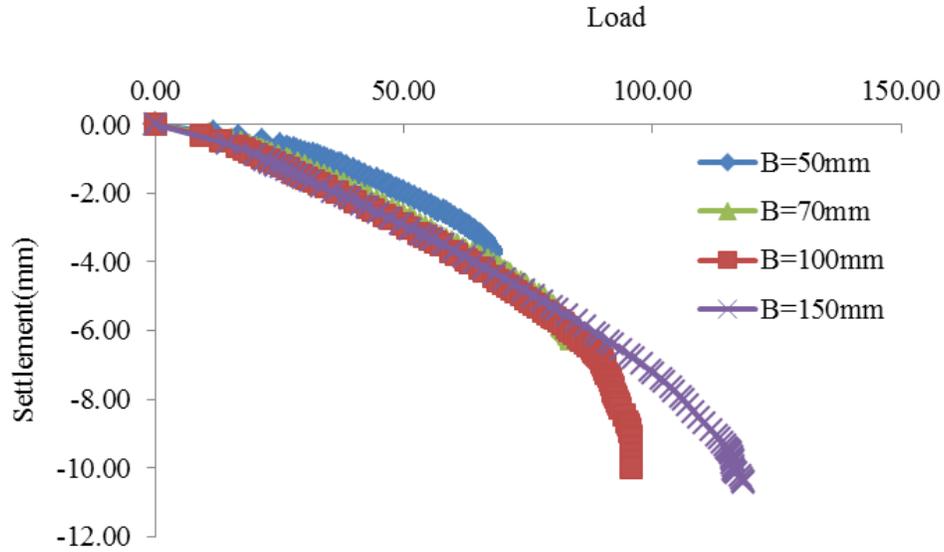
**Figure 11.** Load variations with S for model slope with different footing widths (X/B=1).
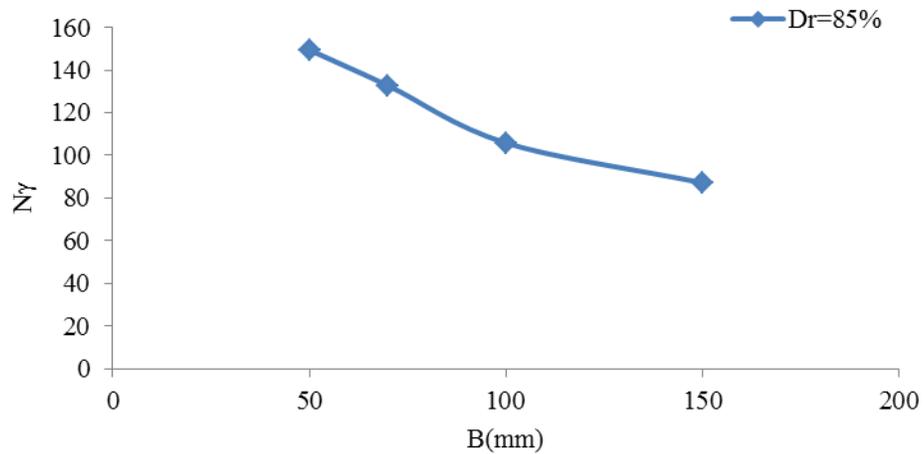
Figure 12. Nγ versus B for 85% relative density.

Table 4. Bearing capacity factor Nγ for strip footing on sand slope with relative density of 60%.

| X/B	B(mm)	Nγ				
		Ψ				
		0	φ/4	φ/2	3φ/4	φ
(0)	50	58.93491	69.5858	76.21302	77.15976	82.36686
	70	37.19358	51.05664	62.21471	62.72189	63.90533
	100	24.26036	37.75148	41.30178	45.08876	46.0355
	150	5.443787	28.00789	31.3215	34.00394	34.47732
(1)	50	69.5858	91.59763	104.142	108.6391	109.3491
	70	25.86644	79.79713	88.25021	90.78614	92.98394
	100	21.06509	59.40828	63.07692	70.88757	72.42604
	150	33.13609	44.26036	49.78304	52.70217	53.57002
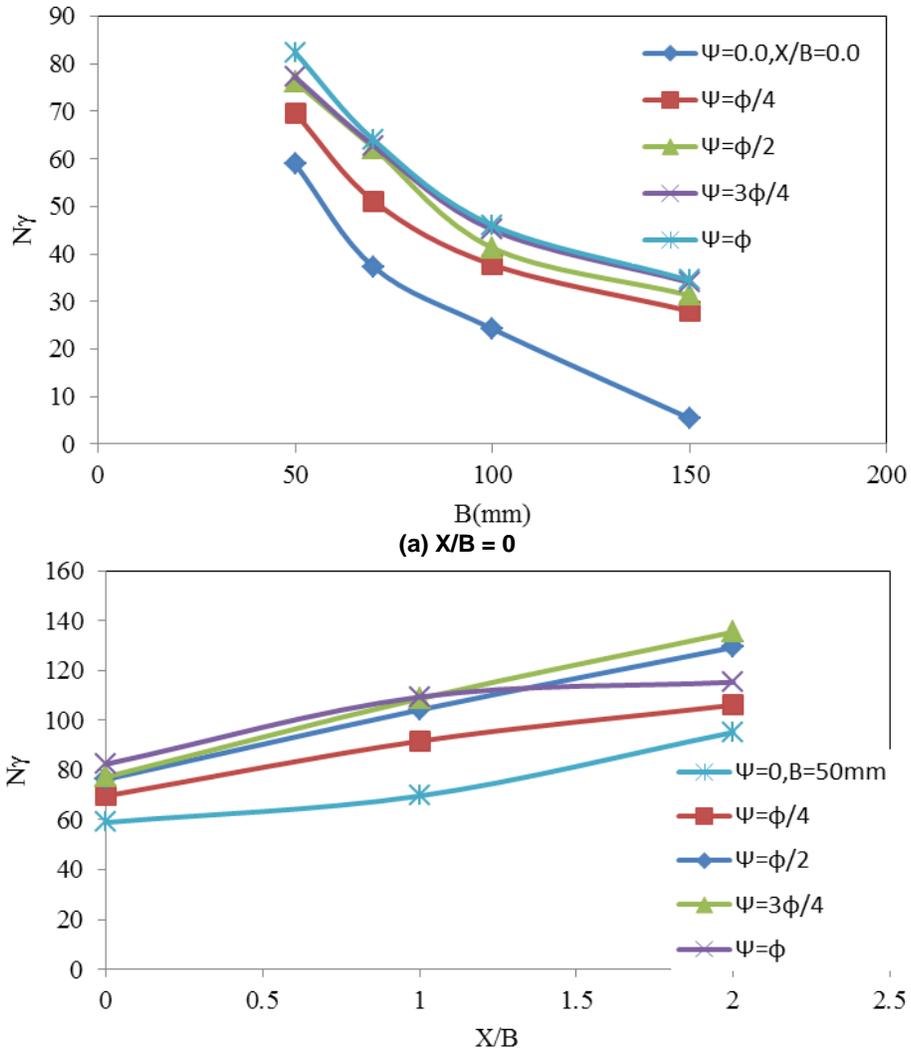
Figure 13. Nγ versus X/B for different φ for relative density of 60%.

values. N_γ decreased significantly when Ψ decreased.

The gap between the two values of N_γ increased with the increase of X. The decrease of N_γ was evident when the value of Ψ/φ decreased from 3/4 to 0. Beyond this limit, the decrease seemed to be insignificant.

Conclusions

A series of experimental and numerical model tests was conducted to evaluate the bearing capacity of a strip footing with and without reinforcement that rests adjacent to the crest of sand slopes. This study mainly aimed to investigate the effects of geotextile depth, footing location, and slope angle on both ultimate bearing

capacity and failure mechanism. Based on our findings, the following conclusions can be drawn:

1. Stabilizing the earth slope by using geotextile at an adequate depth in conjunction of the strip footing adjacent to the slope crest had a significant effect on improving soil bearing capacity.
2. The optimum geotextile depth that produced the maximum ultimate bearing capacity was approximately 0.5 of the footing width.
3. The ultimate bearing capacity of a strip footing with geotextile increased with increasing distance from the footing to the edge and decreased when the angle of slope increased. However, at an edge distance greater than the footing width, the ultimate bearing capacity effectively increased.
4. FEA helped to better explain the failure patterns of the footing-reinforced soil system adjacent to a slope. FEA

also confirmed the load transfer mechanism and illustrated how geotextile can protect the slope from collapsing by decreasing the slope deformation.

REFERENCES

Adams MT, Collin JG (1997). Large Model Spread Footing Load Tests on Geosyntetic Reinforced Soil Foundation. J. Geotech. Geoenviron. Eng. 123(1):66-72.

Akinmusuru JO, Akinbolade JA (1981). Stability of Loaded Footings on Reinforced Soil. J. Geotech. Eng. 107:819-827.

Banimahd M, Woodward PK (2006). Load–displacement and bearing capacity of foundations on granular soils using a multi-surface kinematic constitutive soil model. Int. J. Numer. Anal. Methods Geomech. Wiley 30:865–886.

Bathurst RJ, Blatz JA, Burger MH (2003). Performance of Instrumented Large-Scale Unreinforced and Reinforced Embankments Loaded by a Strip Footing to Failure. Canadian Geotech. J. 40:1067-1083.

Berry DS (1935). Stability of Granular Mixtures. American Society for Testing Materials: Proceedings of the 38th Annual Meeting. 35(2):491-507.

Binquet J, Lee KL (1975a). Bearing Capacity Tests on Reinforced Earth Slabs. J. Geotech. Eng. Div. ASCE. 101(12):1241-1255.

Bolton MD, Lau CK (1989). Scale Effects in the Bearing Capacity of Granular Soils. Proceedings of the 12th International Conference on Soil Mechanics and Foundation Engineering. 2:895-898.

Cerato AB, Lutenegger AJ (2007). Scale effects of shallow foundation bearing capacity on granular material. J. Geotech. Geoenviron. Eng. 133(10):1192-1202.

Chang CS, Cerato AB, Lutenegger AJ (2010). Modelling the scale effect of granular media for strength and bearing Capacity. Int. J. Pavement Eng. 11(5):343–353.

Clark JI (1998). The settlement and bearing capacity of very large foundations on strong soils: the 1996 R. M. Hardy lectures. Canadian Geotech. J. Ottawa 35:131–145.

Das BM, Omar MT (1994). The effects of foundation width on model tests for the bearing capacity of sand with geogrid reinforcement. Geotech. Geol. Eng. 12:133–141

De Beer EE (1963). The scale effect in the transposition of the results of deep-sounding tests on the ultimate bearing capacity of piles and caisson foundations. Geotechnique, 13(1):39-75.

Dixit RK, Mandal JN (1993). Bearing Capacity of Geosynthetic-Reinforced Soil Using Variational Method. Geotextiles and Geomembranes, 12(6):543-566.

El Sawwaf M, Nazir AK (2010). Behavior of repeatedly loaded rectangular footings resting on reinforced sand. Alexandria Eng. J. 49(4):349–356.

El Sawwaf M, Nazir AK (2012). Cyclic settlement behavior of strip footings resting on reinforced layered sand slope. J. Adv. Res. 3(4):315-324.

El Sawwaf ME (2007). Behavior of Strip Footing on Geogrid-Reinforced Sand over a Soft Clay Slope. Geotextiles and Geomembranes, 25(1):50–60.

Fragaszy RJ, Lawton EC (1984). Bearing Capacity of Reinforced Sand Subgrades. J. Geotech. Eng. 110:1500-1507.

Guido VA, Chang DK, Sweeny MA (1985). Comprasion of Geogrid and Geotextile Reinforced Slabs. Canadian Geotech. J. 23:435-440.

Huang C, Tatsuoka F, Sato Y (1994). Failure mechanisms of reinforced sand slopes loaded with a footing. Soils and Foundations 24(2):27-40.

Huang CC, Tatsuoka F (1990). Bearing Capacity of Reinforced Horizontal Sandy Ground. Geotextile Geomembranes, 9:51-82.

Khing KH, Das BM, Puri VK, Cook EE, Yen SC (1993). Bearing Capacity of a Strip Foundation on Geogrid-Reinforced Sand. Geotextile and Geomembranes, 12(4):351-361.

Kumar A, Saran S (2003). Closely Spaced Footings on Geogrid-Reinforced Sand. J. Geotech. Geoenviron. Eng. ASCE 129(7):660-664.

Kumar A, Walia BS (2006). Bearing Capacity of Square Footings on Reinforced Layered Soil. J. Geotech. Geological Eng. 24:1001–1008.

Kumar J, Bhoi MK (2008). Interference of Multiple Strip Footings on Sand Using Small Scale Model Tests. Geotech. Geol. Eng. 26:469–477.

Kusakabe O (1995). Chapter 6: Foundations. *Geotechnical Centrifuge Technology,* R. N. Taylor, ed., Blackie Academic& Professional, London, 118-167.

Kusakabe O, Yamaguchi H, Morikage A (1991). Experiment and Analysis on the Scale Effect of Nγ for Circular and Rectangular Footings. Centrifuge 1991. pp. 179-186.

Laman M, Yildiz A (2003). Model Studies of Ring Foundations on Geogrid-Reinforced Sand. Geosynthetics International, Thomas Telford, 10(5):142-152.

Laman M, Yildiz L, Keskđn MS, Uncuoğlu E (2007). Donatılı Kum Seve Oturan Serit Temelin Deneysel Olarak Đncelenmesi. ĐMO Teknik Dergi, 277:4197-4217.

Lancelot L, Shahrour I, Mahmoud MA (2006) Failure and dilatancy properties of sand at relatively low stresses. J. Eng. Mech. ASCE 132(12):1396–1399

Lee KM, Manjunath VR (2000). Experimental and Numerical Studies of Geosynthetic-Reinforced Sand Slopes Loaded with a Footing. Canadian Geotech. J. 37:828–842.

Mandal JN, Sah HS (1992). Bearing Capacity Tests on Geogrid-Reinforced Clay. Geotextile and Geomembranes, 11(3):327-333.

Michalowski RL (2004). Limit Loads on Reinforced Foundation Soils. J. Geotech. Geoenviron. Eng.130(4):381-390.

Moghaddas SN, Dawson AR (2010). Behavior of footings on reinforced sand subjected to repeated loading – comparing use of 3D and planar geotextile. Geotextiles and Geomembranes 28:434–447.

Moghaddas TSN, Khalaj O (2008). Laboratory tests of small-diameter HDPE Pipes buried in reinforced sand under repeated load. Geotextiles and Geomembranes. 26(2):145–163.

Plaxis (2002). User Manual. 2D version8, (Edited by BRINKGREEVE, R.J.B.), Delft University of Technology&PLAXIS b.v., The Netherlands.

Selvedurai APS, Gnanendran CT (1989). An Experimental Study of a Footing Located on a Sloped Fill: Influence of a Soil Reinforcement Layer. Canadian Geotech. J. 26(3):467–473.

Shiraishi S (1990). Variation in bearing capacity factors of dense sand assessed by model loading tests. Soil and Foundations, 30(1):17-26.

Tatsuoka F, Okahara M, Tanaka T, Tani K, Morimoto T, Siddiquee MSA (1991). Progressive failure and particle size effect in bearing capacity of footing on sand. Geotechnical Engineering Congress 1991. McLean, F., Campbell, D.A., and Harris,D.W., Editors, ASCE Geotechnical Special publication No.27,Vol.2,Proc. Congress held Boulder, Colorado, USA, June1991, pp. 788-802.

Tatsuoka F, Siddiquee MSA, Tanaka T (1994). Link among design, model tests. Theories and sand properties in the bearing capacity of footing on sand. 13th Int. Conf. Soil Mechanics Foundations Eng. New Delhi, India, 1:87-88.

Vidal H (1968). La Terre Arme. Annales de L'Intitut Technique du Batiment et des Travoux Publics: 888-938 (as referred by Das, 1999).

Yetimoğlu T, Wu JTH, Saglamer A (1994). Bearing Capacity of Rectangular Footings on Geogrid-Reinforced Sand. J. Geotech. Eng. 120(12):2083-2099.

Yoo C (2001). Laboratory Investigation of Bearing Capacity Behavior of Strip Footing on Geogrid-Reinforced Sand Slope. Geotextiles and Geomembranes, 19:279–298.

Zhu F, Clark JI, Phillips R (2001). Scale effect of strip and circular footings resting on dense sand. J. Geotechnol. Geoenviron. Eng. ASCE 127(7):613–621.

**14th International Conference on Accelerator and
Large Experimental Physics Control Systems. The Hyatt Regency
Embarcadero Center San Francisco, California October 6-11,
2013**
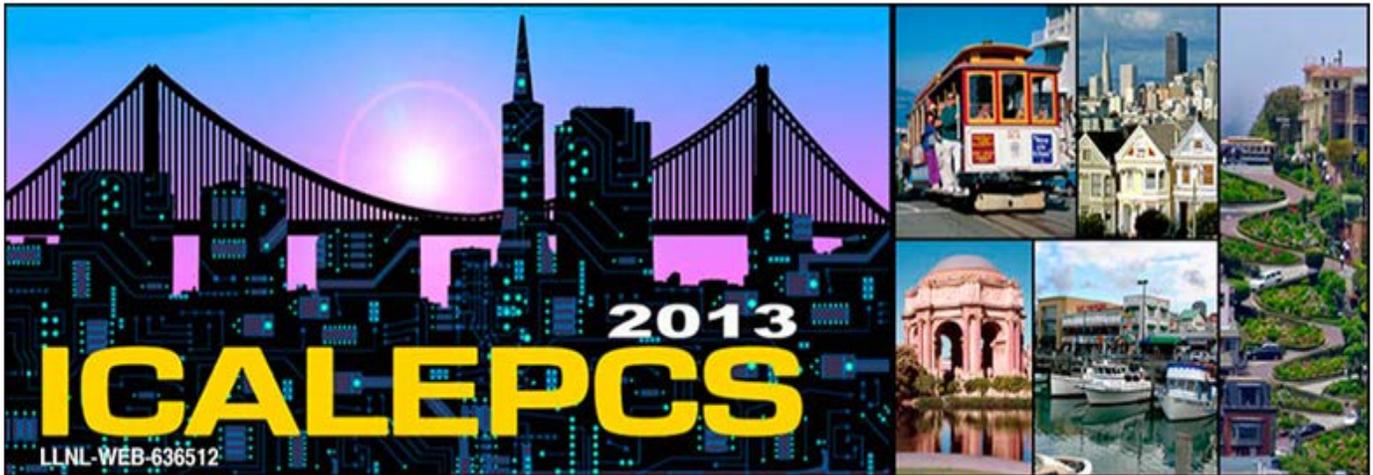
**December 6-7, 2013 Sydney, Australlia 2013 5th
International Conference on Signal Processing Systems**

Conferences and Advert

October 2013

14th International Conference on Accelerator and Large Experimental Physics Control Systems. The Hyatt Regency Embarcadero Center San Francisco, California October 6-11, 2013

December 2013

5th International Conference on Signal Processing Systems Sydney, Australlia, December 6-7, 2013

International Journal of Physical Sciences

academic**Journals**